Studies on cell-autonomous mechanisms for neurodegeneration in prion disease

（プリオン病における神経細胞自律的変性機構に関する研究）

TANAKA Misaki

CONTENTS

ABBREVIATIONS

3D	three-dimensional
AD	Alzheimer's disease
AraC	cytosine β-D-arabinofuranoside
ATF3	activating transcription factor 3
ATF4	activating transcription factor 4
Bax	Bcl2 associated X, apoptosis regulator
Bcl2	apoptosis regulator, B-cell lymphoma 2
BSE	bovine spongiform encephalopathy
cDNA	complementary DNA
CGNs	cerebellar granule neurons
CHOP	C/EBP -homologous protein
CJD	Creutzfeldt-Jakob disease
CxN	primary cortical neuronal culture
DAPI	4',6-diamidino-2-phenylindole
D&F	Diseases & Functions
div	days *in vitro*
dpi	days post infection
dpe	days post exposure
EGFP	enhanced green fluorescence protein
eIF2α	eukaryotic translation initiation factor 2 subunit alpha
ER	endoplasmic reticulum
FC	fold change
GADD34	growth arrest and DNA damage-inducible protein 34
GFAP	glial fibrillary acidic protein
GO	Gene Ontology
GPCR	G protein-coupling receptor
GPI	glycosylphosphatidylinositol
IFA	immunofluorescence assay
IPA	Ingenuity Pathway Analysis
KEGG	Kyoto encyclopedia of genes and genomes
mAb	monoclonal antibody
MAP2	microtubule-associated protein 2
mRNA	messenger RNA
NFW	nuclease-free water
nRPKM	normalized read count per kilobase exon per million reads
NSV	normalized signal value
PBS	Phosphate-buffered saline

p-eIF2α	phosphorylated eIF2α
PERK	Protein kinase R-like endoplasmic reticulum kinase
p-PERK	phosphorylated PERK
PrP	prion protein
PrP^{C}	cellular isoform of prion protein
PrP-res	Proteinase K-resistant prion protein
PrP^{Sc}	pathogenic isoform of prion protein
PSD	post synaptic density
qRT-PCR	quantitative reverse transcription polymerase chain reaction
rAAV	recombinant adeno-associated virus
RNA-Seq	RNA sequencing
RT	Room temperature
RPKM	Read count per kilobase of exon per million reads
rRNA	ribosomal RNA
SDD-PAGE	sodium dodecyl sulfate-polyacrylamide gel electrophoresis
ThN	primary thalamic neuronal culture
UPR	unfolded protein response

PREFACE

Prion disease, also known as transmissible spongiform encephalopathy, is a group of fatal neurodegenerative disorders in both animals and humans which includes scrapie in sheep and goats, bovine spongiform encephalopathy (BSE), chronic wasting disease (CWD) in cervids, and Creutzfeldt-Jakob disease (CJD) in humans [1]. Whereas the majority of human cases are sporadic and familial forms, there are a small number of iatrogenic transmissions of CJD in humans, which were related to neurosurgery and therapeutic use of human cadaveric pituitary growth hormone [2]. Furthermore, animal prion diseases are usually transmitted *via* oral ingestion of tissues of diseased animals [3] or even *via* secretions in the case of CWD, showing a fast but limited geographic spread so far [4, 5]. Apart from the horizontal transmission in a host species, the spatiotemporal relationship between variant CJD and BSE indicated a zoonotic potential of prion diseases [2]; therefore, prions may still pose a significant threat to the health of humans, animals, and the environment as well.

The pathological hallmarks of prion diseases include vacuolation in the neuropil, microglial activation, astrogliosis, synaptic loss, and specifically, accumulation of the pathogenic isoform of prion protein (PrP^{Sc}) in the central nervous system. PrP^{Sc}, a key component of the infectious agent, prions, is a product of self-seeding conformational conversion, or misfolding, of cellular isoform of PrP (PrP^{C}) encoded by the host gene *Prnp* [6-8]. The production of PrP^{Sc} is strongly associated with prion propagation and neurodegeneration in prion diseases. PrP-deficient mice are totally resistant to prion infection, therefore, PrP is a key molecule for prion pathogenesis [9-11]. In addition, brain tissue devoid of PrP was not impaired by exogenous PrP^{Sc} produced in PrP-expressing tissue grafts nearby [12], and the conditional knockout of the neuronal *Prnp* protected or even rescued mice from prion infection as well as neurodegeneration in spite of the presence of PrP^{Sc} in glial cells and extracellular parenchymal space [13, 14]. These facts suggest that not just the presence of PrP^{Sc} but

intraneuronal prion propagation, i.e., misfolding of intrinsically neuronal PrP, is required for the development of prion diseases. Thus, there has been a strong motivation to study the cellular aspects of prion propagation in neural cell lines. Previous studies with the use of persistently prion-infected immortalized neural cell lines, including Neuro2a murine neuroblastoma cells, revealed a subcellular localization of PrP^{Sc}. The subcellular sites where PrP^{Sc} was found, and are likely the conversion site of PrP in those cells, are plasma membranes and lipid rafts [15-17], endocytic pathway [18, 19] or endocytic recycling pathway [20-24], and early and late endosomes at an early step of prion propagation [25].

Contrary to prion propagation mechanisms, we have less knowledge of the cellular and molecular mechanisms that account for the neurodegeneration in prion diseases. There have been two hypotheses that may explain the pathogenesis of prion diseases. One is the loss of physiological function of PrP^{C} because of misfolding; however, this speculation can hardly explain normal development of PrP-deficient mice and other mammals during fetal growth and after birth [26-30]. Another hypothesis is that the gain of toxic function by misfolding into PrP^{Sc} is the cause of neurodegeneration, which is also subject to doubt because exogenous PrP^{Sc} itself did not injure neurons of PrP-deficient mice as reported previously [9-14]. It means that there ought to be alteration or abnormal induction of cellular responses and abnormalities in PrP molecules in the prion pathogenesis. Though limited so far, possible involvements of various physiological and cellular functions in the prion pathogenesis have been proposed.

Synaptic loss and dysfunction are well-described histopathological and electrophysiological alterations in the brain of prion-affected animals and humans at a relatively early stage of the disease, corresponding to behavioral abnormalities in mice [8, 31, 32]. PrP^{Sc} can induce some morphological and functional alterations to neurites as well as synapses, such as spine retraction, decreased miniature excitatory postsynaptic current (mEPSC), and impaired long-term potentiation in cultured hippocampal neurons and slices [33, 34]. The morphological

abnormality of PrP^{Sc}-exposed hippocampal neurons seemed to be similar to what was induced by excitotoxicity in other neurodegenerative disorders [35, 36]. However, the implications of acute synaptotoxicity of PrP^{Sc} for the irreversible neurodegeneration under a condition of continuous prion propagation should still be evaluated.

Apoptotic cell death is found in the brain of naturally occurring human and animal prion diseases and experimental prion disease models as DNA fragmentation and the activated caspases [37-41]. Genetic modifications of apoptotic signaling, such as deletion of pro-apoptotic *Bax* and *Casp12* (caspase-12) and overexpression of anti-apoptotic *Bcl2*, could not prevent neuronal death and degeneration [42-44]; so, the host mice still had a clinical manifestation and died [45]. These facts indicate that not all prion-induced neuronal deaths can be attributed to apoptosis.

Autophagy plays an important role in bulk degradation and recycling of disused cellular constituents to facilitate physiological turnover for maintaining homeostasis in cells. The auto-lysosome, which is formed by the fusion of the autophagosome and lysosome, is a characteristic vesicular structure where disused proteins are degraded by lysosomal enzymes [46]. These autophagic vesicles have been found in the experimental models of several prion diseases including scrapie, BSE, and CJD [47, 48], as well as brain biopsies of human patients of prion diseases [49]. Autophagy may play a role in the clearance of PrP^{Sc}, as the induction of autophagy can reduce PrP^{Sc} level in persistently prion-infected Neuro2a cells [50, 51]. Also, continuous intraperitoneal administration of rapamycin, an autophagy-inducing drug, diminished insoluble fraction of PrP and amyloid plaques in the brain and delayed the onset of disease in a mouse model of human-inherited prion disease [52]. Nonetheless, these mice finally succumbed to the disease, suggesting that the frequent observations of autophagy may be due to a passive response to prions but not to a causative mechanism of neurodegeneration.

Among various cellular functions, unfolded protein response (UPR), in particular the

pathway mediated by protein kinase R-like endoplasmic reticulum kinase (PERK) and eukaryotic translation initiation factor 2 subunit alpha (eIF2α), has been suggested as one of the possible cellular mechanisms that may be involved in the pathogenesis of prion diseases. The PERK-eIF2α pathway of UPR copes with endoplasmic reticulum (ER) stress and disrupts proteostasis by restraining global translation activity through phosphorylation of PERK and eIF2α, decreasing ER tasks and enabling cells time to refold or dispose of inaccurately synthesized proteins [53-56]. When the cells can no longer keep up with continual ER stress, however, downstream activating transcription factor 4 (ATF4) and C/EBP-homologous protein (CHOP) will sensitize the cells for apoptosis by downregulation of the anti-apoptotic protein Bcl-2 and by perturbation of cellular redox systems [57, 58]. As regards the pathogenesis of prion diseases, there has been a report on the upregulation of ER chaperones and enzymes, including Grp58, Grp78, and Grp94, which indicates the induction of UPR, in the brain of patients with sporadic and variant CJD as well as prion-infected mice [59-61]. Experimental interventions which restore the normal translation activity by impeding the activity of PERK or releasing eIF2α from functional repression successfully prolonged the survival of prion-infected mice, clearly demonstrating that sustained activation of the PERK-eIF2α pathway is involved in the prion pathogenesis [62, 63].

It is still an open question that which cell types are primarily responsible for neurodegeneration in prion diseases. Several examinations on the roles of microglia and astrocytes in prion diseases have been carried out due to their remarkable activation. Pharmacological ablation of microglia resulted in a dramatic increase in prion titers and the amount of PrP^{Sc} as well as an increase in susceptibility to prion infection in cerebellar slices [64], implying a microglial function to suppress the propagation of prions. Astrocytes also support prion propagation in cell cultures [65-67] and modify the microenvironment into what is stressful for the sensitized prion-infected neurons [68]. Even though the contributions of glial

cells and their functional molecules to neurodegeneration have been energetically studied, it is still unclear whether the activation of glial cells is protective or harmful to prion-infected neurons. Crucial glial factors that modify the progress of disease have not been found so far [69, 70], and the effect of microglia depletion varied either neuro-protective or neuro-detrimental, in accordance with the period of treatment [71-74]. Anyhow, studies on glial cells have not totally explained the neurodegeneration mechanisms caused by prions, which is a reminder of the importance of a specific analysis of prion-induced neuronal responses to discover whether the neurodegeneration is consequent exclusively on neuron-autonomous mechanisms.

Mice that are inoculated with prions have been the conventional models of prion diseases as they faithfully reproduce the neurodegeneration process. However, the analysis of specific to neuronal phenomena will be hampered in animal models because of the structural complexity of the brain as well as the presence of activated glial cells that obscure the genuine neuronal responses. The use of immortalized neural cell lines is one of the options; however, there are only a few cell lines that are capable of stable and continual prion propagation [75-79]. Unfortunately, those prion-susceptible cell lines showed no sign of cytotoxicity associated with persistent prion infection, excluding one report that used the GT1 hypothalamic cell line [80].

Primary neurons may serve as versatile *ex vivo* models, judging from some reports that showed that cultured neurons allowed prion propagation and resulting neuronal death and degeneration [81-83]. Thus, primary cultures of murine cerebral cortical and thalamic neurons were established, in which the growth of glial cells, especially astrocytes that easily contaminate neuronal cultures, was successfully and strongly repressed by anti-mitotic drug treatment. These primary neurons were susceptible to infection with mouse-adapted scrapie prions (22L, Chandler, and Obihiro strains). When assessed using immunofluorescent staining and immunoblotting, PrP^{Sc} produced in this primary culture of cortical neurons shows unique

features; the neuronal PrP^{Sc} is localized in the vicinity of the cell surface and neurites [84]. The characteristic neuronal PrP^{Sc} localization takes after that observed in brains of prion-infected mice [85, 86] but not in immortalized cell lines in which intracellular, the N-terminally truncated PrP^{Sc} is dominant [20-24, 87]. Thus, my study was extended with the use of the primary cultures to analyze neuron-autonomous events.

In my thesis, I extensively analyzed prion-induced neuron-autonomous alterations with the use of primary neuronal cultures to elucidate the mechanisms of neurodegeneration in prion diseases. In Chapter I, I describe the induction of the early event in UPR as a neuron-autonomous response to the propagation of prions, and in Chapter II, I describe the transcriptome analysis of prion-infected neurons to evaluate any changes in neurons caused by the propagation of prions.

CHAPTER I

Characterization of neuron-autonomous phenotypic alterations caused by prion propagation in neuron-enriched murine primary cultures.

INTRODUCTION

Numbers of prion diseases have been known in humans and animals, however, knowledge of the molecular mechanisms of neurodegeneration is insufficient to understand the neuropathobiology of prion diseases. It has been strongly suggested that intraneuronal misfolding of PrP and a primary response of neurons to it are essential for the prion pathogenesis [9-14]. However, the cellular and molecular mechanisms remain to be elucidated.

One of cellular machineries to deal with protein misfolding is called UPR (unfolded protein response), which is a set of important physiological processes induced by ER stress to maintain the proteostasis in cells [53]. The ER stress initially activates a sensor molecule, PERK, by inducing autophosphorylation which confers kinase activity on it. The activated PERK then phosphorylates eIF2α. Phosphorylated eIF2α deprives a critical function of eIF2 in translation, resulting in repression of global protein synthesis in the cell [53-56]. Simultaneously, ATF4 will be selectively induced due to its eIF2α-independent translation. ATF4 upregulates several stress-responsive genes such as ATF3 (*atf3*) [88], negative feedback associated-GADD34 (*Ppp1r15A)* [89], and pro-apoptotic CHOP (*Ddit3*) [57, 58]. CHOP finally sensitizes cells that cannot keep up with persistent ER stress for cell death [90, 91]. In the last decade, Dr. Moreno and her colleagues have demonstrated a crucial role of sustained activation of the PERK-eIF2α pathway in the prion pathogenesis. They showed that overexpression of GADD34 or pharmacological inhibition of PERK activity, both of which can reduce the phosphorylation level of eIF2α, rescued mice from disease progression, whereas administration of an eIF2α phosphatase inhibitor, salubrinal, accelerated the disease [62, 63]. It is still an open question as to whether production of PrP^{Sc} in neurons directly induces ER stress, and if it does, whether neuronal PrP^{Sc} fully activates neurotoxic signaling pathways downstream of the PERK-eIF2α pathway which may lead to loss of synapses or neuronal cell death.

To analyze neuron-autonomous events specifically, a highly neuronal, but experimentally

tractable models are needed. Unfortunately, lines of immortalized neural and neuronal cells rarely showed any alterations associated with persistent prion propagation [75-79]. Primary culture of neurons is another option, which usefulness in the study on neurodegeneration has been indicated in recent studies [81-83]. These primary neuronal cultures used in previous studies allowed the growth of astrocytes, partially due to a need for their neurotrophic support during a long-term culture. For the purpose of analyzing the neuron-autonomous events, I optimized a neuron-enrichment protocol which is able to control astrocytic growth in cortical and thalamic neuronal cultures over four weeks.

In Chapter I, I extensively analyzed the consequences of autonomous neuronal responses on prion propagation using neuron-enriched cortical and thalamic primary cultures. Although no apparent neuronal loss or neurite loss was associated with the continuous production of PrP^{Sc} in the primary neurons, I found that phosphorylation of PERK was enhanced in prion-infected cortical neurons in accordance with the amount of PrP^{Sc} in a cell. Interestingly, this did not fully activate the downstream pathway of UPR.

MATERIALS & METHODS

1. Antibodies

For PrP^{Sc}-specific detection in immunofluorescence assay (IFA), mouse monoclonal antibodies (mAbs) 132 and 8D5 that recognize mouse PrP amino acids 119–127 [92] and 31–39 [93], were used. Anti-PrP mAb 31C6 that recognizes mouse PrP amino acids 143–149 [92] was used to detect proteinase K-resistant prion protein (PrP-res) by immunoblotting. Other commercially available antibodies used in this study are listed in Table 1.

Table I-1. Commercially available antibodies used in this study

Antigen	Host	Poly /Mono	Clone	Manufacturer	Product No.
ATF4	rabbit	Mono	D4B8	CST	#11815
Beta-III tubulin	rabbit	Poly		abcam	ab18207
Bip	rabbit	Poly		abcam	ab21685
CHOP	rabbit	Mono	D46F1	CST	#5554
eIF2-alpha	rabbit	Mono	D7D3	CST	#5324
GluR1(AMPA subtype)	rabbit	Poly		abcam	ab31232
MAP2	chicken	Poly		abcam	ab5392
NeuN	rabbit	Mono	EPR12763	abcam	ab177487
NMDAR1	rabbit	Mono	EPR2481(2)	abcam	ab109182
p-EIF2S1(S51)	rabbit	Mono	E90	abcam	ab32157
PERK	rabbit	Mono	C33E10	CST	#3192
p-PERK(Thr980)	rabbit	Mono	16F8	CST	#3179
PSD95	mouse	Mono	7E3-1B8	abcam	ab13552
SAP102	rabbit	Poly		abcam	ab152132
SNAP25	rabbit	Poly		abcam	ab5666
synaptophysin	rabbit	Mono	EP1098Y	abcam	ab52636
syntaxin1a	rabbit	Poly		abcam	ab41453
VAMP2	rabbit	Poly		abcam	ab3347

CST: Cell Signaling Technology

2. Preparation of neuron-enriched primary cultures

All of the procedures for animal experiments were conducted in accordance with protocols approved by the Institutional Animal Care and Use Committee at Hokkaido University (approval No.18-0110). Pregnant ICR mice were purchased from CLEA Japan, and primary cortical and thalamic neurons were prepared as described previously [84]. Briefly,

meninges, hippocampi and olfactory bulbs were carefully removed from embryonic brains at day 14 under a stereo microscope. Cerebral cortex and thalamus were collected separately, and the tissues pieces were enzymatically dissolved using Neural Tissue Dissociation Kit (P) (Miltenyi Biotec, 130-092-628) according to the manufacturer's instructions except for a modification on enzymatic reactions performed on ice. Cells were resuspended into Neurobasal medium supplemented with B-27 and GlutaMAX supplements (Gibco, 21103049,17504044, and 35050061), seeded at a density of 1.0×10^5 cells/cm^2 on μ-slide and μ-plate polymer coverslips (ibidi, 80826 & 89626) for immunostaining, and cell culture multidishes (Thermo Scientific). For neuron-enrichment, cells were treated with cytosine β-D-arabinofuranoside (AraC) (Sigma-Aldrich, C6645) at a final concentration of 0.25 μM from 4 to 7 days *in vitro* (div). At 7 div, cells were exposed to microsomal fractions prepared from brain homogenates of terminally ill mice infected with mouse-adapted scrapie Chandler- and Obihiro-strains at an amount equivalent to 5 ng of PrP-res per 10^5 cells simultaneously with half-replacement of the media. Inoculum prepared from brains of age-matched healthy mice was used for mock-infection at an equivalent total protein amount to prion-containing inocula. At 4 days post infection (dpi), the media were completely replaced with AraC-free, fresh media; thereafter, media were half-replaced with fresh media twice a week. In some experiments, uninfected neurons were treated with tunicamycin (Sigma-Aldrich, T7765) at a final concentration of 5 μg/ml for 24 hrs just before the experiments to induce ER stress and UPR.

3. Immunoblot analysis

3-1. Immunoblotting for synaptic proteins

Primary neurons were lysed by scratching in lysis buffer [78] and subjected to DC protein assay (Bio-Rad, 5000112JA) to measure total protein concentrations. For each set of lysates collected at the same dpi, an equivalent amount of total protein was subjected to sodium dodecyl

sulfate-polyacrylamide gel electrophoresis (SDS-PAGE) on 8% to 15% which concentration was determined according to the molecular size of target proteins. Proteins were transferred onto a PVDF membrane (Millipore, IPVH00010), and blocked with 1% skimmilk and 0.1% Tween20 in phosphate-buffered saline (PBS). Membranes were cut into strips in accordance with protein size standard to detect targets and internal marker (βIII-tubulin) on the same membrane for normalization. The blots were probed with appropriate antibodies followed by chemiluminescence detection as described elsewhere [78]. βIII-tubulin was used as an internal marker for normalization.

3-2. Immunoblotting for UPR-related proteins

Primary neurons were directly lysed in SDS-sample buffer supplemented with a cOmplete protein inhibitor cocktail and PhosSTOP phosphatase inhibitor cocktail (Roche, 4693124001 & 4906845001), then subjected to SDS-PAGE and following immunoblotting as described in 2-1.

3-3. Immunoblotting for PrP-res

From each lysate, 30 μg of total protein were used for proteinase K (PK)-digestions with 20 ug of PK. SDS-PAGE, immunoblotting and chemiluminescence detection were performed as previously described [78, 94] except that PrP-res were detected by direct immunostaining with Fab fractions of mAb 31C6 that were genetically conjugated with human placental alkaline phosphatase [95].

4. Quantitative reverse transcription polymerase chain reaction (qRT-PCR)

Neurons cultured on 12-well multidish plates were directly dissolved into TRIzol reagent (Invitrogen, 15596018) and total RNA was isolated according to the manufacturer's instructions.

RNA was resuspended into nuclease-free water (Invitrogen, AM9932), and the concentration was determined using a Nano Drop (Thermo Scientific). cDNA was synthesized from 300-600 ng of the total RNA using First-Strand cDNA Synthesis kit (GE Healthcare, 27-9261-01) with $pd(N)_6$ primer. Quantitative PCR was carried out using TaqMan Fast Universal PCR Mater Mix and TaqMan Probes (Applied Biosystems, 4352042) on a 7900HT Fast Real-Time PCR system (Applied Biosystems). The TaqMan Probes used in this analysis are listed in Table 2. Data was analyzed by delta-delta cycle threshold method using *Tubb3* (βIII-tubulin) as an internal control.

Table 2. Commercially available TaqMan Probes used in this study.

Target gene	Product No.	Target gene	Product No.
Atf3	Mm00476033_m1	*Ppp1r15A*	Mm01205601_g1
Ddit3	Mm01135937_g1	*Snap25*	Mm01276449_m1
Dlg4	Mm00492193_m1	*Stx1a*	Mm00444008_m1
Gria1	Mm00433753_m1	*Syp*	Mm00436850_m1
Hspa5	Mm00517691_m1	*Tubb3*	Mm00727586_s1

5. Preparation of recombinant adeno-associated viral vector (rAAV)

To visualize neurons in primary cultures, a rAAV expressing enhanced green fluorescence protein (EGFP) under the control of the human synapsin promoter was used. rAAV was prepared as described by Challis et al. [96] with slight modifications. Briefly, the viral genome was packaged into AAV-PHP.eB capsid by triple-transfection of HEK293T cells with three plasmids; pAAV-hSyn-EGFP was a gift from Bryan Roth (Addgene, plasmid #50465), pUCmini-iCAP-PHP.eB was a gift from Viviana Gradinaru (Addgene, plasmid #103005) [97], and pHelper vector in AAVpro® CRISPR/SaCas9 Helper Free System (AAV2) (Takara Bio, 632619). rAAV-PHP.eB-hSyn-EGFP was purified by iodixanol-density gradient centrifugation using a SW32 Ti rotor at 175,000 × *g* (32,000 rpm) for 6.5 hrs at 18°C followed by ultrafilteration using Amicon Ultra-15 Ultracel-100K columns (Merck Millipore, UFC910024). Titration of rAAV was performed using quantitative PCR. To prepare the viral DNA sample, rAAV was digested with PK at 50 μg/ml at 50°C overnight. PK digestion was stopped by adding

Pefabloc SC (Roche, 1585916/Sigma-Aldrich 11585916001) at a final concentration of 2.2 mM and boiling for 20 min. Quantitative PCR was carried out using a custom-designed TaqMan Probe targeting the woodchuck hepatitis posttranscriptional regulatory element sequence with TaqMan Fast Universal PCR Mater Mix (Applied Biosystems). Linearized pAAV-hSyn-EGFP (5,265 base pairs) with *Pvu*I digestion was used as the DNA standard. Of note, 10 ng of the linearized dsDNA fragments correspond to 7.4×10^9 ssDNA molecules.

6. Immunofluorescence assay of primary neurons

Immunostaining of primary neurons was performed as previously described [24, 84]. Briefly, neurons were fixed with 4% paraformaldehyde in PBS at room temperature (RT) for 10 min and permeabilized with 0.1% TritonX-100, 0.1 M Glycine in PBS. For PrP^{Sc}-specific staining with mAb 132, cells were treated with 5 M guanidine thiocyanate at RT for 10 min and washed with PBS. After blocking with 5% fetal bovine serum-PBS, cells were incubated with primary antibodies at 4°C overnight. Appropriate second antibodies conjugated with Alexa Fluor dyes (Molecular Probes) were selected for each experiment, and nuclei were counterstained with 4',6-diamidino-2-phenylindole (DAPI). An LSM700 inverted confocal microscope and ZEN2009 software (ZEISS) were used for image acquisition, except for the experiments for Figure I-3 described in the next section.

7. Image analysis of cell density and neurite outgrowth

Neurons cultured on ibidi µ-plates were immunostained for NeuN and microtubule-associated protein 2 (MAP2) with DAPI counterstaining as described above. Images were acquired at 9 fixed positions in each well configured by XY-coordinates prior to experiments (in total 1.36×10^6 μm^2 from one well) using an Olympus IX71 fluorescence microscope with ×10 objective lens operated by MetaMorph software version 7.8.4.0 (Molecular Devices) (multiple stage positions and auto focus functions were used). MetaMorph was also used for

image analyses. Living neuronal nuclei were identified as DAPI-positive objects whose size was ≥ 60 μm^2 and average NeuN intensity was above the threshold. I used the same threshold for both mock-infected and prion-infected preparations in the same experiment. Neurite density was measured using a threshold function and was represented as the surface coverage (%) by MAP2-positive area. In these measurements, an average of the 9 positions was acquired to calculate a representative score of the well, and 9 wells from 3 independent experiments were used for each group.

8. Three-dimensional (3D) image analyses

8-1. Quantification of the signal frequency of phosphorylated PERK (p-PERK)

Z-series of confocal images (z-stack) from the bottom to the top of cell bodies of neurons immunostained for p-PERK, MAP2, and PrP^{Sc} (with mAb 8D5) were acquired at 0.78 μm steps with a ×630 final magnification. The z-stacks were reconstructed by 3D rendering to build a segmented object designated as "surface" using Surface function of Imaris software version 7.6.1. (Bitplane). Surfaces of MAP2 (cell body), DAPI (nucleus), mAb 8D5 (PrP^{Sc}) and p-PERK were reconstructed for each of neurons. Neurites were manually pruned away to separate individual neurons. The number of p-PERK granular surfaces inside the cell body (MAP2 surface) but outside the nucleus (DAPI surface) of each neuron was counted and represented as the signal frequency (granule/cell). The number of PrP^{Sc} surfaces inside or adherent to the cell body was also counted, which was used to classify prion-infected neurons into three subpopulations according to the amount of PrP^{Sc} as described in Figure I-7.

8-2. Quantification of the density of synaptic terminals

Neurons transduced with the rAAV vector expressing EGFP were immunostained for PrP^{Sc} (with mAb 8D5) and PSD95 or synaptophysin. For double staining of PrP^{Sc} and PSD95,

the immunostaining procedure was slightly modified since both of the antibodies are mouse IgGs. First, immunostaining for PSD95 was completed by indirect method, then free Fab regions of the anti-mouse IgG secondary antibodies were blocked with a mouse IgG isotype control antibody (mAb P2-284 [98]) to avoid cross-reaction with mAb 8D5. Alexa Fluor 555-conjugated mAb 8D5 was used for the PrP^{Sc}-specific immunostaining [84]. Z-stacks of EGFP-expressing neurons were acquired from the bottom to the top of neurites at 0.78 μm steps with a ×63 objective lens and ×0.5 digital zoom, which resulted in acquisition of images of a 203 μm × 203 μm size at ×315 final magnification. The surfaces of signals from EGFP (neuron), DAPI (nucleus), mAb 8D5 (PrP^{Sc}), and PSD95- or synaptophysin (post- or pre-synaptic terminals) were reconstructed using Imaris software. The number of PSD95 or synaptophysin surfaces inside EGFP surfaces were counted and divided by the volume of each EGFP surface to represent the densities of post- and pre-synaptic terminals for each neuron (number of terminals/cell volume of 1000 voxels). The number of PrP^{Sc} surfaces was also counted as described above.

RESULTS

I-i. Time-course of prion propagation in primary cultures of mouse cerebral cortical and thalamic neurons.

I previously reported that the primarily cerebral cortical neuronal culture (CxN) propagate mouse-adapted scrapie prions (22L, Chandler, and Obihiro strains) [84]. In the current study, I prepared primary neuronal cultures from thalamus (ThN) as well as the cortex considering any differences in the efficiency of prion propagation *ex vivo*. To analyze neuron-autonomous events triggered by PrP^{Sc} production in neurons, primary cultures were briefly treated with AraC to suppress glial cells growth (hereafter referred to as neuron-enrichment). Proportion of neuronal cells in primary cultures were shown in Figure I-1. NeuN-positive, GFAP-positive, and NeuN- and GFAP-double negative cells were 89.3%, 3.5%, and 7.2%, respectively in AraC treated, mock-infected CxN. GFAP-positive cells were 13.8% in CxN without AraC treatment, indicating successful reduction of astrocyte growth in our CxN. Similar tendency was observed in ThN. Immunoblotting showed linear increases in the amount of PrP-res from 7 dpi to 28 dpi, in CxNs and ThNs exposed to Chandler and Obihiro prions. As expected, there was no signal of PrP-res in mock-infected neurons at 28 dpi, demonstrating successful prion propagations in prion-infected cultures (Figures I-2A and I-2B). PrP-res levels in CxNs were equivalent to those in ThNs for both prion strains tested at 21 dpi (Figure I-2C). The level of PrP-res in Obihiro-infected neurons appeared higher than that in Chandler-infected neurons; this may be explained by difference in prion titer of the same amount of PrP-res, and also by difference in intrinsic PK-resistance of PrP^{Sc} between prion strains [99]. PrP^{Sc}-specific immunostaining with mAb 132 displayed PrP^{Sc} clinging to neuronal cell bodies and neurites in prion-infected CxNs and ThNs (Figure I-2D). The frequencies of PrP^{Sc}-positive neurons (Figure I-2D, filled arrowheads) in Obihiro-infected CxN and ThN were 42.9% and 54.8%, respectively, when examined at 200× final magnification (21 dpi). Notably, some PrP^{Sc}-positive neurons

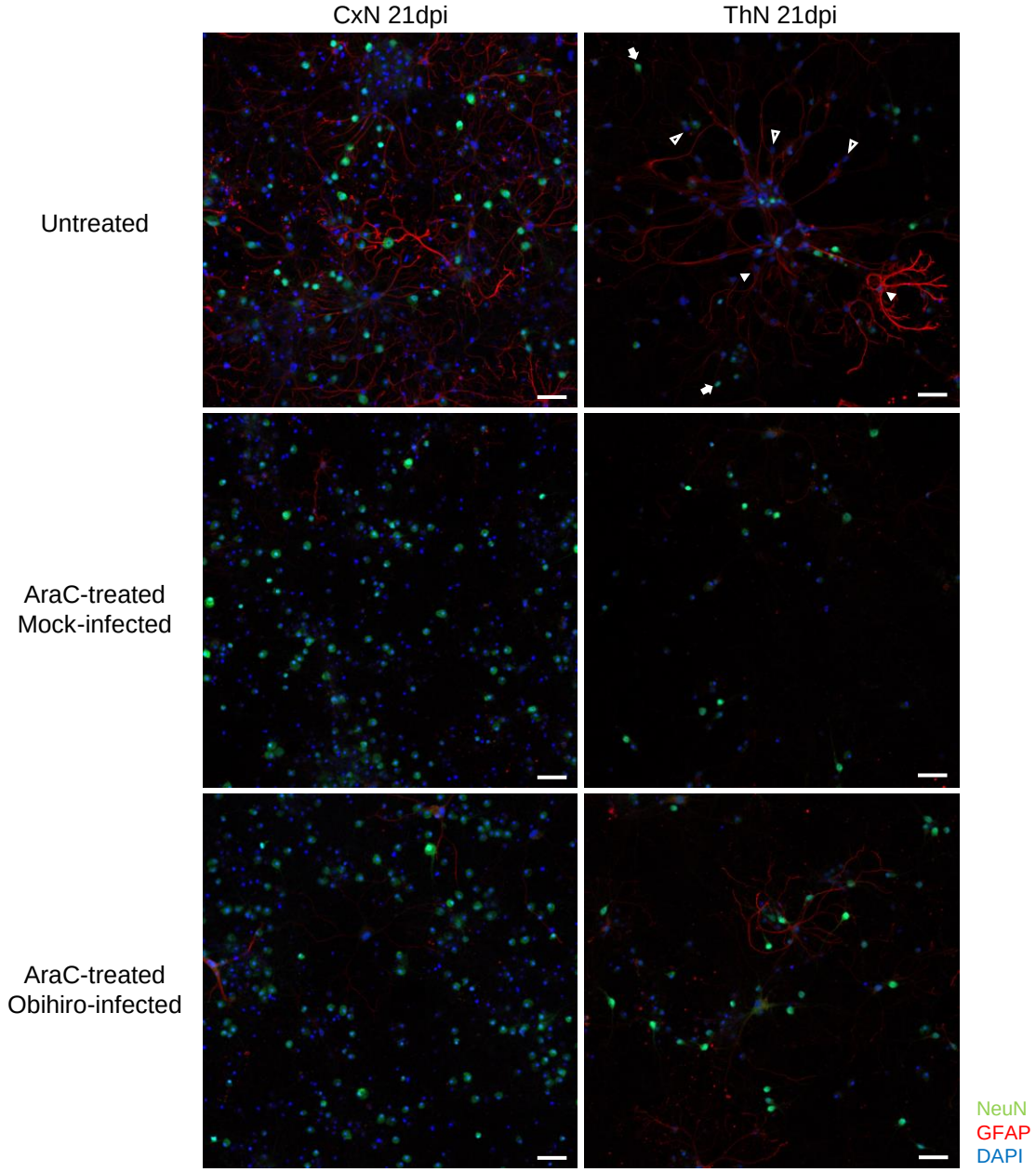

	CxN			ThN		
AraC	-	+	+	-	+	+
Infection (Obihiro strain)	-	-	+	-	-	+
NeuN+ neurons (%)	65.9	89.3	81.4	28.0	89.4	77.5
GFAP+ astrocytes (%)	13.8	3.5	6.2	28.0	1.5	2.9
Unidentified cells (%)	20.3	7.2	12.4	44.1	9.1	19.6
The number of cells counted	782	424	271	472	131	306

Figure I-1. Proportions of NeuN-positive neurons and GFAP-positive astrocytes in primary cultures used in this study.
Primary neuronal cultures were treated with antimitotic AraC at 0.25 μM from 4 days in vitro (div) to 7 div in the first week. Cells were immunostained for NeuN and GFAP to identify neurons and astrocytes in the cultures at 21 days post infection (21 dpi corresponds to 28 div). MetaMorph software was used to set a threshold of fluorescent intensity for each cell marker. Cells which were not immunostained for NeuN and GFAP, and have shrunk and condensed nuclei (DAPI+ area $\leq$ 80 μm^2) were considered as putative dead cells and removed from counting. Images show representative CxNs and ThNs cultured under each condition. Arrows, filled arrowheads, and open arrowheads indicate NeuN-positive neurons, GFAP-positive astrocytes, and unidentified cells (NeuN- and GFAP-negative cells), respectively. The table shows percentages of each cell type in the cultures. Bars, 50 μm.

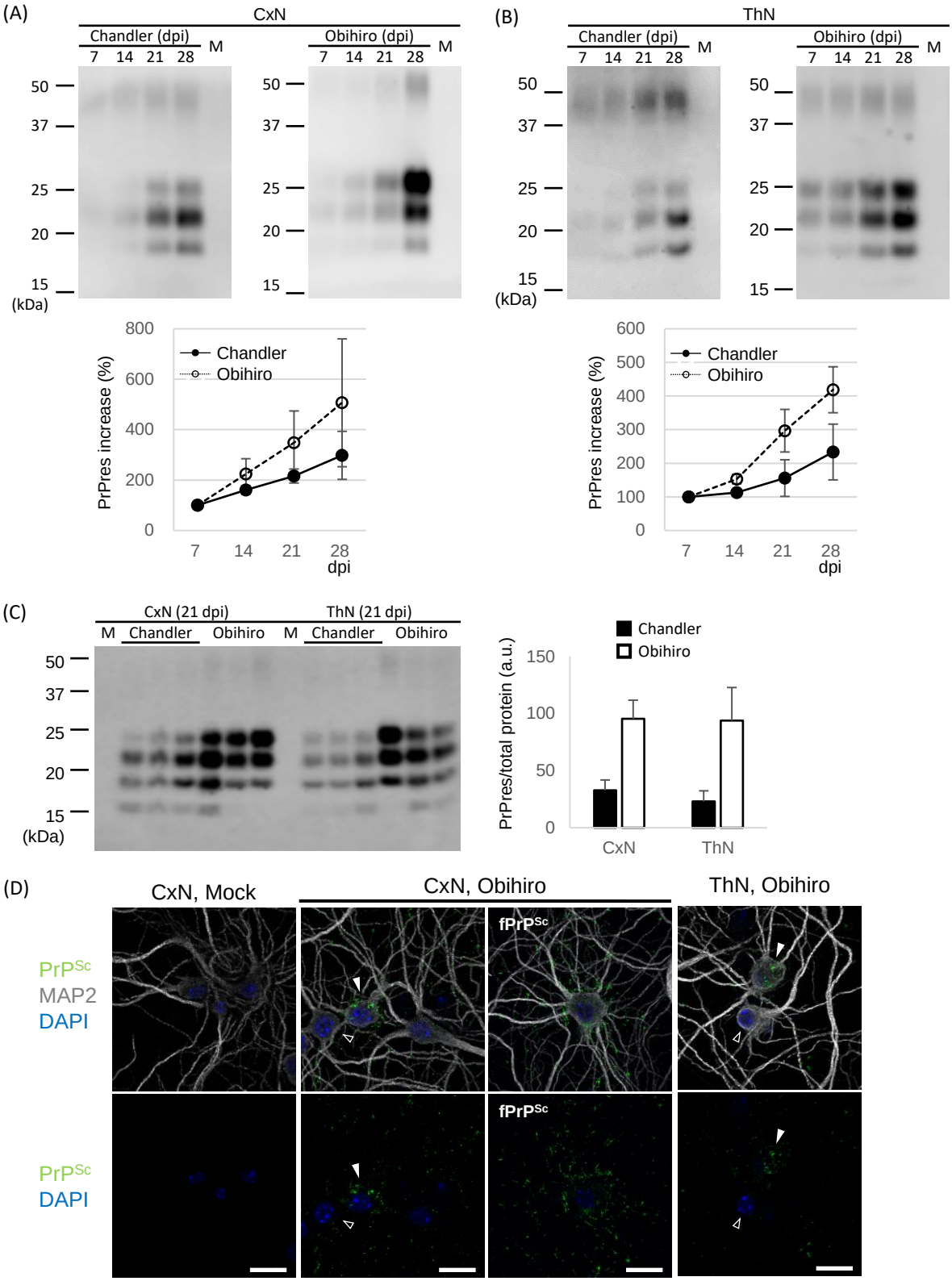

Figure I-2. Prion propagation in primary cultures of mouse cerebral cortical and thalamic neurons.
(A, B) Representative immunoblots for PK-resistant PrP^{Sc} (PrP-res) in (A) cerebral cortical neurons (CxN) and (B) thalamic neurons (ThN), infected with mouse-adapted scrapie Chandler and Obihiro strains. Graphs show the results of quantification as a mean ± SE of three independent experiments performed in triplicate. Mean intensities at 7 dpi were used as benchmarks (100%) for time-course comparisons: dpi, days post infection; M, mock-infected neurons at 28 dpi. (C) Comparison of PrP-res levels between neuronal types or prion strains at 21 dpi. The graph shows the mean ± SD for experiments performed in triplicate. (D) Immunofluorescent detection of PrP^{Sc} in primary neurons at 21 dpi. Cells were denatured with guanidine thiocyanate but not digested with PK for PrP^{Sc}-specific detection by mAb132. Panels labeled $fPrP^{Sc}$ show neurons with a swarm of typical filamentous PrP^{Sc} staining. Filled arrowheads, neurons with PrP^{Sc} staining (PrP^{Sc}-positive neurons); open arrowheads, neurons with apparently no PrP^{Sc} staining. Figures are shown as maximum intensity projection images created from z-stack confocal sections at ×315 final magnification. Bars, 20 μm.

possessed a swarm of filamentous PrP^{Sc} staining around their cell bodies and neurites ($fPrP^{Sc}$ neurons, Figure I-2D). $fPrP^{Sc}$ neurons accounted for 10.0% and 7.5% of the total neurons in Obihiro-infected CxN and ThN (21 dpi), respectively.

I-ii. Influence of prion propagation on the densities of neuronal cells and neurites.

CxN and ThN successfully propagated Chandler and Obihiro prions (Figure I-2). To examine whether production of PrP^{Sc} can cause any immediate alteration in CxN and ThN, I began a series of analyses with a quantitative image analysis to evaluate the number of neurons and their density of neurites in CxN and ThN. MAP2 is mainly distributed over the dendrites and cell bodies of mature neurons and is widely used as a neuronal marker in immunostaining. NeuN is an alternative splicing factor of pre-mRNAs named *Rbfox3*, and is also a reliable marker for mature neurons. Since NeuN is detected in neuronal nuclei and disappears when cells die, immunostaining for NeuN is a convenient way for counting live neurons in primary culture where dead cell populations are inevitable over time. As shown in Figure I-3, there were time-dependent changes in the number of NeuN-positive cells and MAP2-positive neurite extensions; CxN grew slowly and displayed the highest densities of neuronal cells at 14 dpi followed by continued elaboration into a dense neurite network (Figure I-3A, 3B), whereas ThN had the highest densities of both neuronal cells and neurites at 7 dpi (Figure I-3D, 3E). Taking into consideration experimental variations that exist between independently prepared primary neuronal cultures, measurements was normalized to the average of mock-treated neurons in the same experiment at each time point. Neuronal cell density was lower in prion-infected CxNs than in mock-infected CxN at 7 dpi, however, the decreasing trends were not continuous (Figure I-3C); in fact, the density of neuronal cells in prion-infected CxNs were comparable to mock-infected CxN at 21 dpi when 42.9% of cells were positive for PrP^{Sc} in Obihiro-infected CxN. Neurite densities of prion-infected CxNs were slightly lower than those of mock-infected CxN at all experimental timepoints, but neurodegenerative alterations, such as exacerbation of

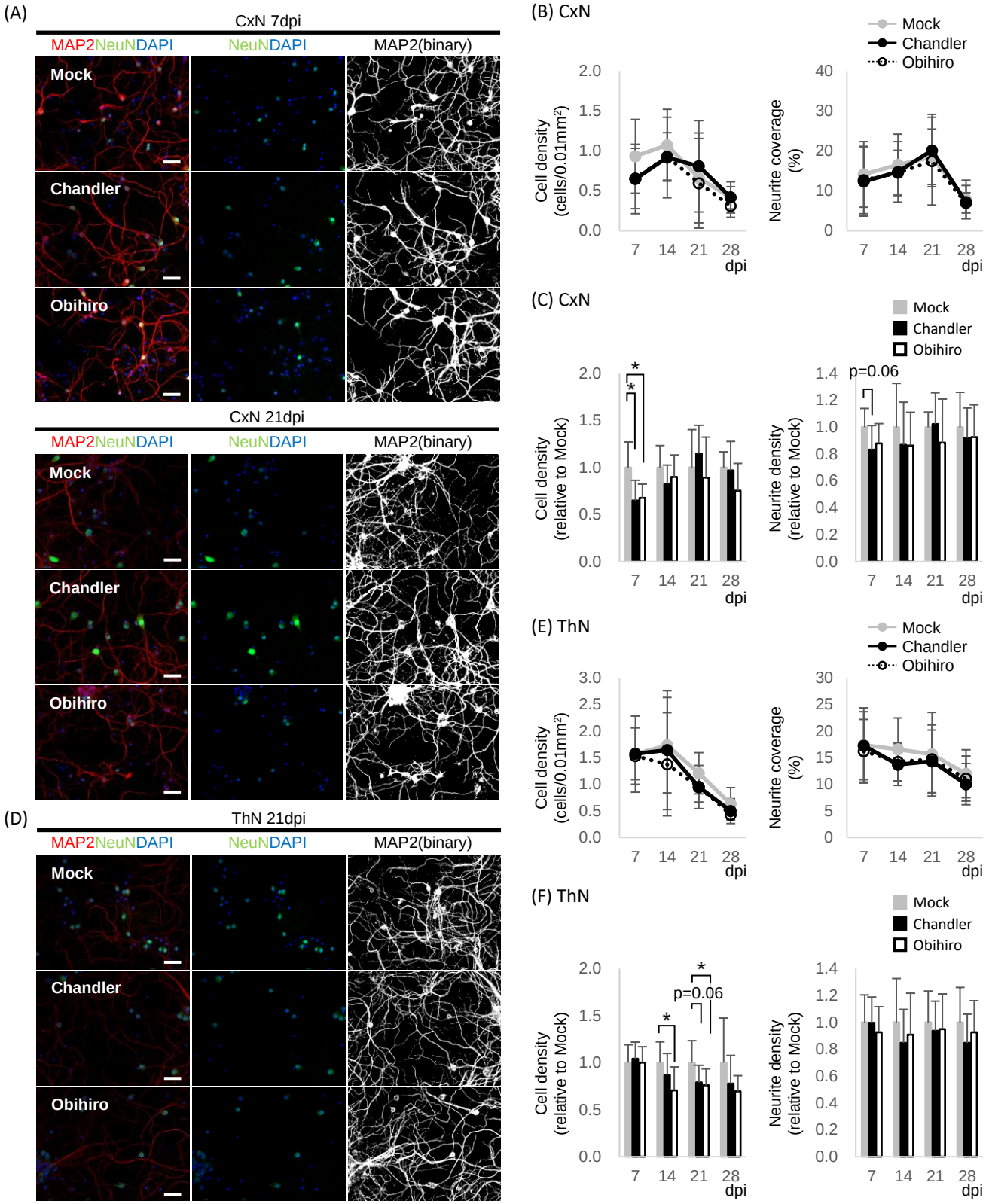

Figure I-3. Influence of prion propagation on the densities of neuronal cells and neurites.
(A&D) Representative images of neurons used for the quantitative image analysis. (A) CxNs at 7 and 21dpi, and (D) ThNs at 21 dpi. From the left, panels show merged images, subsets of NeuN and DAPI, and binary images of MAP2 signals. (B&C) Neuronal cell density and neurite density of CxNs were measured by image analysis of immunofluorescent images stained for MAP2 and NeuN using MetaMorph software. Cell density and neurite density were defined as the number of NeuN-positive nuclei per 0.01 mm^2 and the surface coverage (%) by MAP2-positive neurites, respectively (B), which are normalized to the averages of dpi-matched mock-infected neurons in each experiment for comparison with independent experiments at different dpi (C). Bar graphs show mean ± SD of 9 replicates from 3 independent experiments. *, $p < 0.05$ by Dunnett's test using dpi-matched mock-infected neurons as control groups. (E&F) Results of image analysis of ThNs performed as described in (B&C).

neurite sparseness, were not observed despite the rising levels of PrP-res (Figure I-3C). In prion-infected ThNs, the number of neurons decreased to approximately 70% of mock-infected ThN by 14 dpi, implying the existence of subpopulation(s) that are more susceptible to acute prion toxicity [34, 100] *ex vivo* (Figure I-3F). However, prion-infected ThNs did not show progressive neuronal loss despite continuous increases in PrP-res levels. Moreover, prion-infected ThNs maintained dense neurite-networks comparable to mock-infected ThNs throughout the experiment (Figure I-3F), suggesting that the production of PrP^{Sc} did not solely induce neuronal death nor neurite loss detectable by immunostaining for MAP2 and NeuN.

I-iii. ER stress and UPR in prion-infected neurons.

The PERK-eIF2α pathway of UPR copes with disrupted proteostasis by restraining global protein synthesis *via* phosphorylation of PERK and eIF2α; reducing ER tasks and enabling cells time to refold or dispose of inaccurately synthesized proteins [53]. ATF4 is a key molecule in this pathway as it induces effector molecule production, including the pro-apoptotic protein CHOP [101]. The involvement of ER stress and the PERK-eIF2α pathway in prion pathogenesis has been demonstrated in prion-infected mice [62, 63], though it is still unclear whether prion propagation directly evokes ER stress and induces UPR in neurons. To examine the activation state of UPR during the continuous production of PrP^{Sc} in CxN and ThN, I first analyzed phosphorylation levels of PERK and eIF2α, and the induction of ATF4 in Obihiro-infected neurons. Immunoblotting revealed that enhanced phosphorylation of PERK in prion-infected CxNs at 7 dpi and thereafter. The prion-infected CxNs also had a tendency to increase the phosphorylation level of eIF2α, although it was not statistically significant (Figures I-4A & I-4C). On the other hand, phosphorylation levels of PERK and eIF2α in Obihiro-infected ThN were comparable to those of uninfected ThN (Figures I-4B & I-4C), despite the comparable amounts of PrP-res in Obihiro-infected ThN and CxN (Figures I-2C). In contrast to the

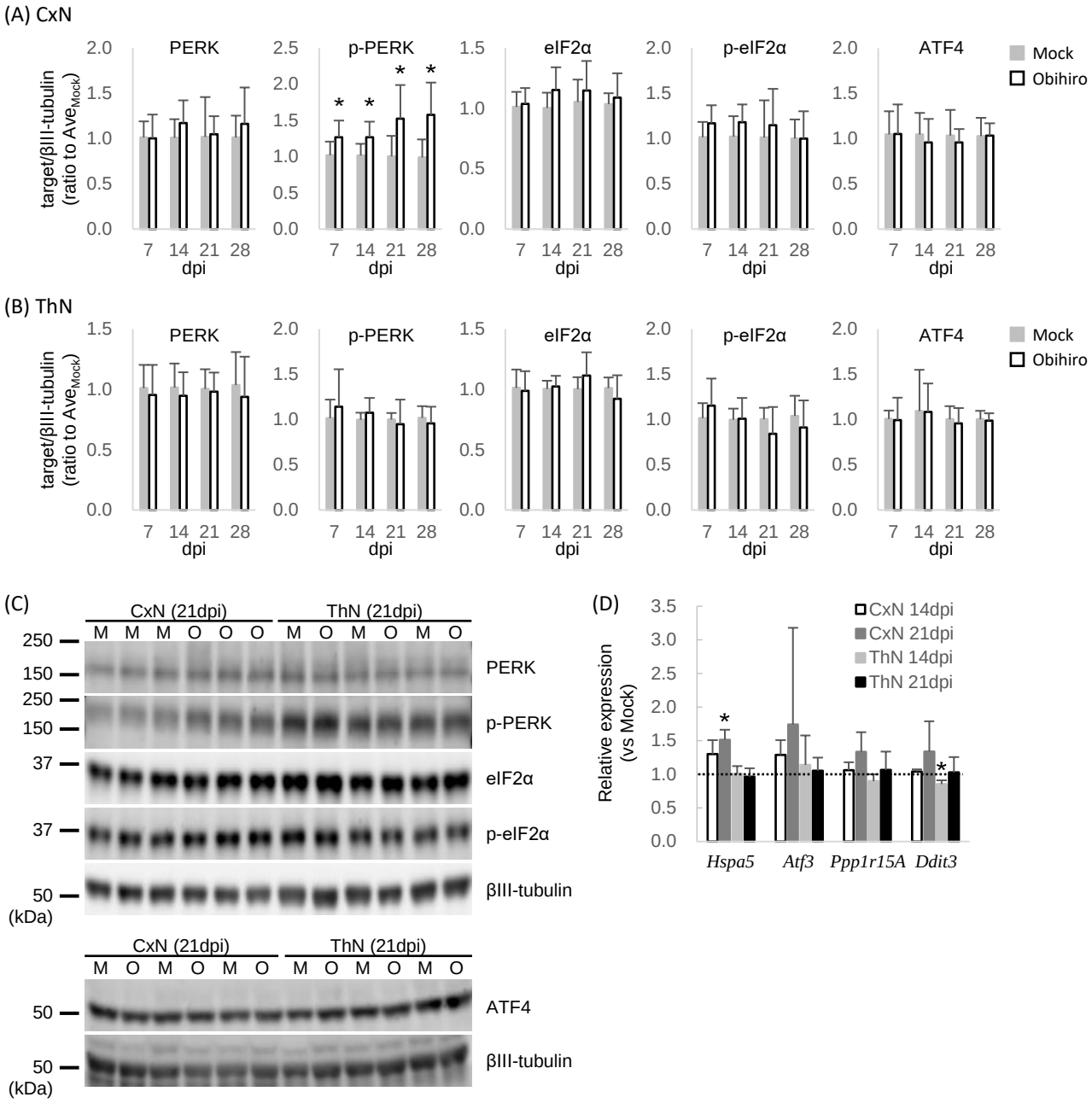

Figure I-4. ER stress and unfolded protein response in prion-infected neurons.
(A, B) Immunoblot analysis of molecules involved in the PERK-eIF2α pathway in CxNs (A) and ThNs (B). Protein levels are represented as relative values to the average of mock-infected, dpi-matched neurons (mean ± SD of 6 replicates from 2 independent experiments). p-PERK, phosphorylated PERK; p-eIF2α, phosphorylated eIF2α. *, $p < 0.05$ by Student's *t* test. (C) Representative blots used for quantification shown in (A) and (B). βIII-tubulin from the same blot were used as internal controls. M, mock-infected neurons; O, Obihiro-infected neurons. For the detection of βIII-tubulin in the analysis of ATF4, peroxidase conjugated with anti-rabbit IgG secondary antibodies used for the detection of ATF4 was deactivated with 15% hydrogen peroxide solution, then βIII-tubulin was detected with peroxidase-conjugated anti-chicken IgY secondary antibodies. M, Mock-infected; O, Obihiro-infected. (D) Expression of genes in the PERK-ATF4 axis analyzed by qRT-PCR. Relative expression levels in Obihiro-infected CxNs and ThNs to dpi-matched mock-infected neurons are shown as mean ± SD of 3 independent experiments. The broken line indicates relative expression levels = 1. *, $p < 0.05$ by One sample *t* test.

enhanced phosphorylation of PERK, protein levels of ATF4 in prion-infected CxN and ThN were not elevated (Figures I-4A-4C). I further examined gene expression levels for *Atf3*, *Ddit3*, *Ppp1r15A*, and *Hspa5*, which encode ATF3, CHOP, GADD34, and Bip, respectively, all of which are known to be up-regulated during ER stress through the PERK-ATF4 axis [88, 89, 101-103]. Upregulation of these genes was not observed in prion-infected CxNs and ThNs, except for Hspa5 in prion-infected CxNs at 21dpi (Figure I-4D), which can be upregulated by other pathways of UPR, such as ATF6-mediated signaling [104]. As a whole, the results of transcriptional analysis were consistent with no increase ATF4 protein levels. Ratios of p-PERK to total PERK and p-eIF2α to eIF2α were calculated (Figure I-5). Although differences were not statistically significant, p-PERK/total PERK ratios tended to be higher in prion-infected CxN and ThN than mock-infected CxN and ThN. In contrast to ratios of p-PERK/total PERK, those of p-eIF2α/ total eIF2α did not differ between prion-infected and mock-infected primary neurons. Taken together, the results suggest that phosphorylation of PERK was induced in response to prion propagation in CxNs, which may reflect ER stress in prion-infected CxNs. However, the downstream pathway of PERK was not activated.

I-iv. Influence of prion propagation on the amounts of post- and pre-synaptic proteins.

Synaptic loss and disfunctions have been observed in the brain of prion-affected animals prior to neuronal loss [32, 105]. Of those alterations, decreases in the protein levels of several synaptic proteins such as SNAP25 and PSD95 have been reported in association with sustained activation of the UPR PERK-eIF2α pathway [62]. To confirm whether prion propagation has any influence on synaptic proteins in cultured neurons, I analyzed a total of 8 post- and pre-synaptic proteins by immunoblotting (Figure I-6): post-synaptic AMPAR and NMDAR1 (glutamate receptors), and PSD95 and SAP102 (scaffold proteins); pre-synaptic syntaxin1a, SNAP25, and VAMP2 (SNARE proteins involved in intracellular membrane fusion during exocytosis of neurotransmitters), and synaptophysin (an integral membrane protein of synapse

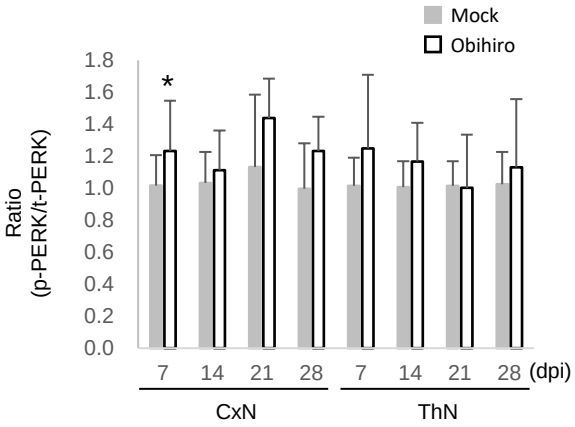

Ratio (p-PERK/t-PERK)

		7dpi	14dpi	21dpi	28dpi
CxN	Mock	1.02 ± 0.19	1.03 ± 0.19	1.13 ± 0.45	1.00 ± 0.28
	Obihiro	1.23 ± 0.31*	1.11 ± 0.25	1.44 ± 0.25	1.23 ± 0.21
ThN	Mock	1.02 ± 0.18	1.01 ± 0.16	1.02 ± 0.16	1.03 ± 0.20
	Obihiro	1.25 ± 0.46	1.17 ± 0.24	1.00 ± 0.33	1.13 ± 0.43

*p = 0.09 by Student's *t* test

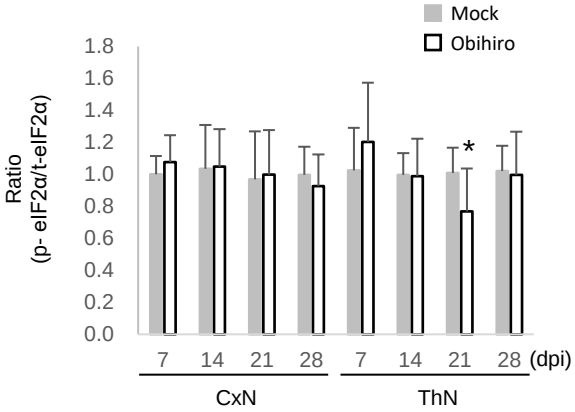

Ratio (p-eIF2α/t-eIF2α)

		7dpi	14dpi	21dpi	28dpi
CxN	Mock	1.00 ± 0.11	1.04 ± 0.27	0.97 ± 0.30	1.00 ± 0.18
	Obihiro	1.08 ± 0.17	1.05 ± 0.24	1.00 ± 0.28	0.93 ± 0.20
ThN	Mock	1.02 ± 0.27	1.00 ± 0.14	1.01 ± 0.16	1.02 ± 0.16
	Obihiro	1.20 ± 0.37	0.99 ± 0.23	0.77 ± 0.27*	1.00+ 0.27

*p = 0.09 by Student's *t* test

Figure I-5. Ratios of phosphorylated PERK (p-PERK) to total PERK (t-PERK) and phosphorylated eIF2α (p-eIF2α) to total eIF2α (t-eIF2α).

Phosphorylation levels of PERK and eIF2α were assessed as ratio between the phosphorylated and total protein signals quantified by immunoblotting described in Fig 3. Ratios of p-PERK/t-PERK (top) and p-eIF2α/ t-eIF2α (bottom) are indicated in Tables (mean ± SD). Although differences were not statistically significant, p-PERK/t-PERK ratios tended to be higher in prion-infected CxNs and ThNs than mock-infected CxNs and ThNs. In contrast to ratios of p-PERK/t-PERK, those of p-eIF2α/t-eIF2α did not differ between prion-infected and mock-infected primary neurons.

vesicles). At 7 dpi, although most differences were not statistically significant except for SNAP25 ($p < 0.05$), the levels of these synaptic proteins in Chandler- and Obihiro-infected CxNs showed tendencies toward decreased levels in comparison to mock-infected CxNs (Figure I-6A), which allowed us to speculate that prion propagation had a repressive influence on the expression of synaptic proteins in the early phase of prion infection. Intriguingly, this trend unexpectedly reversed; leading to increased synaptic markers by 21 dpi. In particular, the levels of PSD95, syntaxin1a, and VAMP2 in Obihiro-infected CxNs were significantly higher than mock-infected CxNs. Of note, several studies conducted in the last decade using animal models and brain slices also reported that increased numbers of synaptic terminals or spines and the size of post-synaptic densities in the early phases of disease, either just before or after the first detection of PrP-res [62, 106, 107], which were similar to the autonomous neuronal events I observed.

Obihiro-infected ThNs at 7 dpi also had a tendency for decreased synaptic protein levels, similar to CxNs. The levels of AMPAR, VAMP2, and SNAP25 were significantly decreased ($p < 0.05$) compared to mock-infected ThNs (Figure I-6B). The decrease in protein levels appeared to be restored by 21 dpi; however, transient increases in synaptic protein levels were less obvious in prion-infected ThNs when compared to CxNs. Taken as a whole, the results show a tendency for the loss of both post- and pre-synaptic proteins in the early stages of prion infection in primary neurons (at 7 dpi). Unexpectedly, the trend was not observed thereafter, despite the continuous prion propagation.

I-v. Phosphorylation of PERK in PrP^{Sc}-positive neurons.

Prion-infected CxNs and ThNs did not show any evident neuronal death or neurodegeneration in the current study. However, considering that the ratio of PrP^{Sc}-positive neurons as examined by IFA were 42.9% in CxNs and 54.8% in ThNs including $fPrP^{Sc}$ neurons (10.0% and 7.5%, respectively) at 21 dpi, I analyzed individual PrP^{Sc}-positive neurons to

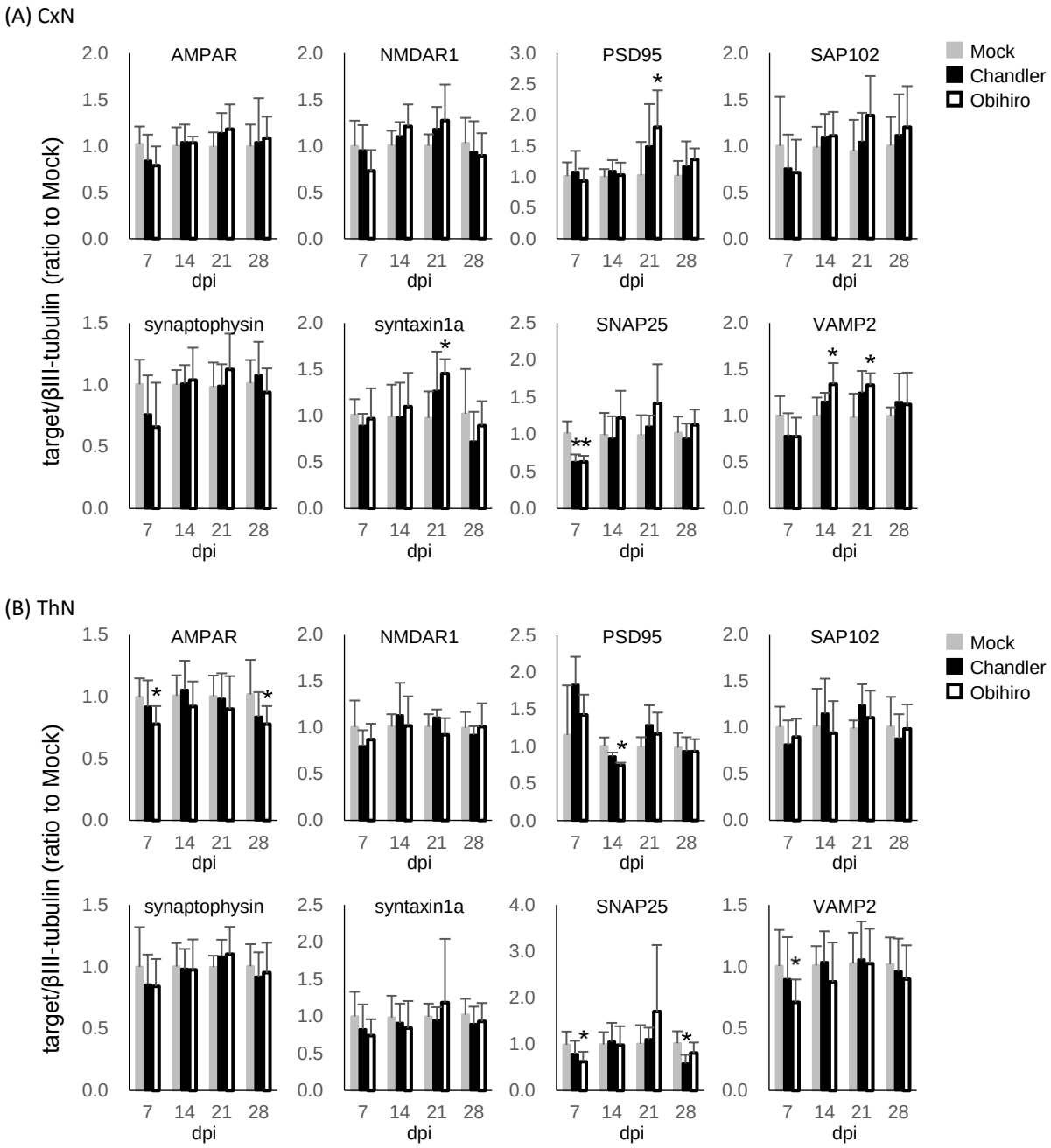

Figure I-6. Influence of prion propagation on the amounts of post- and pre-synaptic proteins.

(A, B) Immunoblot analysis of post- and pre-synaptic proteins in CxNs (A) and ThNs (B). βIII-tubulin from the same blot were used as internal controls. Protein levels of post- (AMPAR, NMDAR1, PSD95 and SAP102) and pre- (synaptophysin, syntaxin1a, SNAP25 and VAMP2) synapse-associated molecules are represented as relative values to the average of mock-infected, dpi-matched neurons (mean ± SD of 7-8 biological replicates from 2 independent experiments; *, $p < 0.05$ by Dunnett's test using mock-infected neurons as control groups).

examine the effects of PrP^{Sc} production on neurons more carefully. The mAb 8D5 has the unique property that it selectively binds to native PrP^{Sc} in IFA without treating cells with chaotropic agents such as guanidine thiocyanate [84, 93], which enabled us to carry out a PrP^{Sc}-positive neuron-selective analysis.

I examined neurons in mock- and Obihiro-infected CxNs at 21 dpi for p-PERK and PrP^{Sc} by immunofluorescence staining to ascertain whether initial UPR events were triggered by PrP^{Sc} production (Figure I-7). Granular stains of p-PERK were observed in the soma of mock-infected and Obihiro-infected neurons in CxNs at 21dpi, indicating that phosphorylation of PERK is not an event specific to prion infection (Figure I-7A). Interestingly, however, intense granular stains of p-PERK were often observed in neurons with a larger number of granular and/or filamentous PrP^{Sc} signals (Figure I-7A, arrow). Quantitative image analysis of p-PERK and PrP^{Sc} signals in each neuron identified a positive correlation between these two molecules in neurons in Obihiro-infected CxN (Figure I-7B, correlation coefficient = 0.49). When neurons in Obihiro-infected CxNs were divided into three subpopulations according to the frequency of PrP^{Sc} signal at its soma (PrP^{Sc}_low, PrP^{Sc}+, and PrP^{Sc}++), the frequency of p-PERK signals was significantly increased in PrP^{Sc}+ neurons, and PrP^{Sc}++ neurons when compared to either mock-infected neurons or PrP^{Sc}_low neurons (Figure I-7C). These data strongly suggest that the production of PrP^{Sc} caused ER stress to neurons and accelerated the phosphorylation of PERK, which is known to be the initial event for activating the PERK-ATF4 axis of UPR. The acceleration of PERK phosphorylation was also observed in PrP^{Sc}++ neurons of ThN (Figure I-8A-8C). I re-examined the expression of ATF4 by co-immunofluorescence staining to see if the PERK-ATF4 axis was activated in the neurons with PrP^{Sc}. While induction and nuclear localization of ATF4 were observed in both CxNs and ThNs treated with tunicamycin, an ER stressor, no ATF4-positive neurons were observed in Obihiro-infected CxNs or ThNs (Figures I-7D & I-8D).

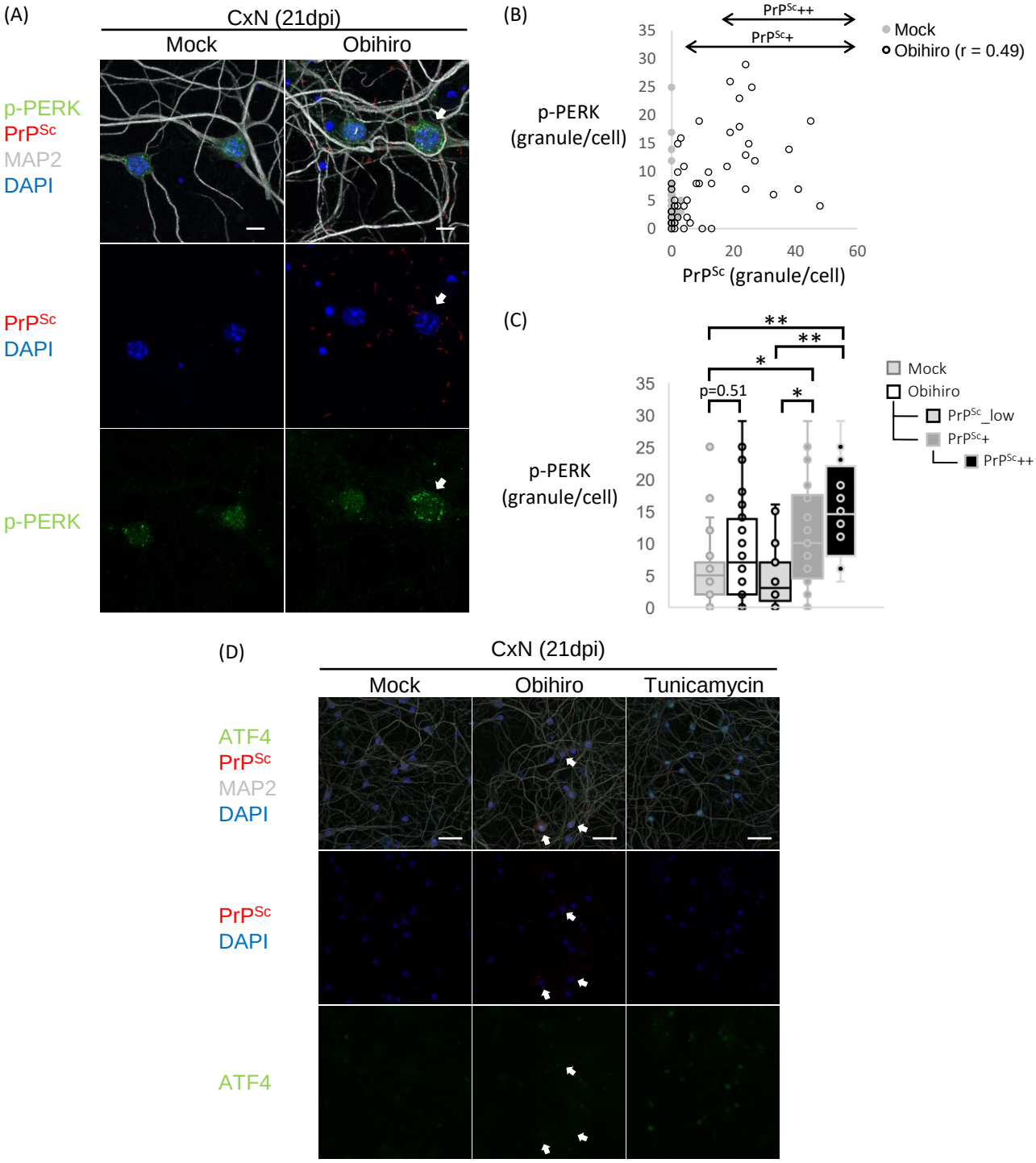

Figure I-7. Phosphorylation of PERK in PrP^{Sc}-positive cortical neurons.
(A) Multiple immunofluorescence staining for p-PERK and PrP^{Sc} with counter staining for cell bodies (MAP2) and nuclei (DAPI) in CxNs at 21 dpi. PrP^{Sc} was stained with mAb 8D5. Figures are shown as maximum intensity projection images created from z-stacks of confocal images at ×630 final magnification. Arrows, PrP^{Sc}++ neurons; bars, 10 μm. (B, C) Quantification of p-PERK and PrP^{Sc} in individual neurons by 3D-image analysis using Imaris software. Each dot in the scatter diagram (B) represents an individual neuron (r, correlation coefficient). In (C), Obihiro-infected CxN was analyzed as a whole (Obihiro) and as three subpopulations classified by the frequency of PrP^{Sc} signals at the soma. The definition of the three subpopulations classified by the frequency of PrP^{Sc} signals at tha soma. The definition of the three subpopulations and the number of cells used for this analysis are as follows: PrP^{Sc}_low (< 4 PrP^{Sc} signals/cell, n = 19), PrP^{Sc}+ (≥ 4 PrP^{Sc} signals/cell, n = 29), PrP^{Sc}++ (≥ 18 PrP^{Sc} signals/cell, n= 16). The number of cells in mock-infected CxN and Obihiro-infected CxN used for the analysis are n = 35 and n= 48 (a total of PrP^{Sc}_low and PrP^{Sc}+ subpopulations), respectively. Differences between the groups were analyzed by Steel-Dwass's multiple comparison test (*, $p < 0.05$; **, $p < 0.01$). (D) Co-immunofluorescence staining for ATF4 and PrP^{Sc} with counter staining for MAP2 and DAPI in CxNs at 21 dpi. PrP^{Sc} was stained with mAb8D5. Uninfected neurons treated with tunicamycin was used as a positive control for ATF4-staining. The green fluorescence in mock- and Obihiro-infected CxNs is the autofluorescence from condensed nuclei of dead cells. Arrows, PrP^{Sc}++ neurons; Bars, 50 μm.

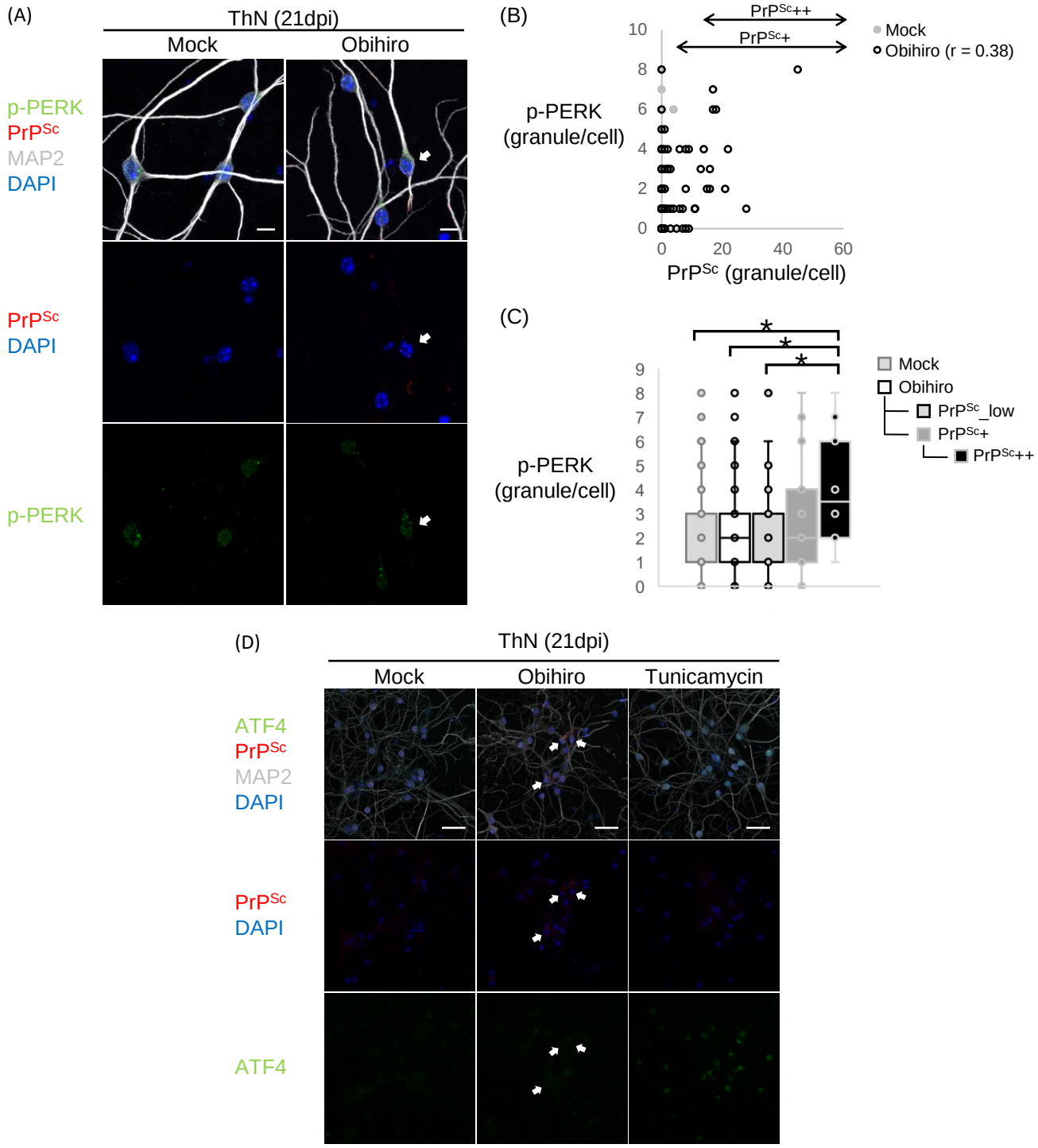

Figure I-8. Phosphorylation of PERK in PrP^{Sc}-positive thalamic neurons.
(A) Multiple immunofluorescence staining for p-PERK and PrP^{Sc} (mAb 8D5) in ThNs at 21 dpi. Figures are shown as maximum intensity projection images at ×630 final magnification. Arrows, PrP^{Sc}++ neurons; bars, 50 μm. (B, C) Quantification of p-PERK and PrP^{Sc} in individual neurons by 3D-image analysis using Imaris software. Each dot in the scatter diagram (B) represents an individual thalamic neuron although some neurons are spotted at the same position (r, correlation coefficient). In (C), Obihiro-infected ThN was analyzed as a whole (Obihiro) and as three subpopulations classified by the frequency of PrP^{Sc} signals at the soma. The definition of the three subpopulations and the number of cells used for this analysis are as follows: PrP^{Sc}_low (< 4 PrP^{Sc} signals/cell, n = 49), PrP^{Sc}+ (≥ 4 PrP^{Sc} signals/cell, n = 26), and PrP^{Sc}++ (≥ 13 PrP^{Sc} signals/cell, n = 12). The number of cells in mock-infected ThN and Obihiro-infected ThN used for the analysis are n = 49 and n= 75 (a total of PrP^{Sc}_low and PrP^{Sc}+ subpopulations), respectively. Differences between the groups were analyzed by Steel-Dwass's multiple comparison test (*, $p < 0.05$). (D) Co-immunofluorescence staining for ATF4 and PrP^{Sc} (mAb 8D5) in ThNs at 21 dpi.Tunicamycin-treated, uninfected neurons were used as a positive control for ATF4-staining. The green fluorescence in mock- and Obihiro-infected CxNs is the autofluorescence from condensed nuclei of dead cells. Arrows, PrP^{Sc}++ neurons; Bars, 50 μm.

I-vi. Synapse densities of PrP^{Sc}-positive neurons.

In the end of the series of experiments, I examined synaptic alterations in PrP^{Sc}-positive neurons by co-immunostaining. The dense networks of neurites in the primary cultures made it difficult to identify processes from a single neuron by immunofluorescence staining for MAP2; therefore, EGFP was expressed in neurons using an adeno-associated viral vector. In this analysis I focused on the densities at post- and pre-synaptic terminals, i.e., the number of synaptic terminals in a unit volume of a cell, inside and in close proximity to EGFP-expressing neurons by 3D-measurement using a z-series of confocal images (Figure I-9A). Obihiro-infected CxNs were divided into three subpopulations according to the density of PrP^{Sc} signals as described above (Figure I-9B, right). Quantitative image analyses of post- and pre-synaptic terminals, using PSD95 and synaptophysin as markers respectively, did not show any synaptic losses in Obihiro-infected CxNs at 21 dpi, even in PrP^{Sc}++ subpopulations (Figure I-9B, left & center). The average density of PSD95-positive post-synaptic terminals was slightly higher in PrP^{Sc}++ neurons when compared to mock-infected neurons ($p = 0.08$); which may reflect the increased levels of PSD95 in Obihiro-infected CxN at 21 dpi detected by immunoblot analysis (Figure I-6). No differences were observed in the densities of post- and pre-synaptic terminals between neurons in mock- and Obihiro-infected ThNs at 21 dpi (Figure I-10).

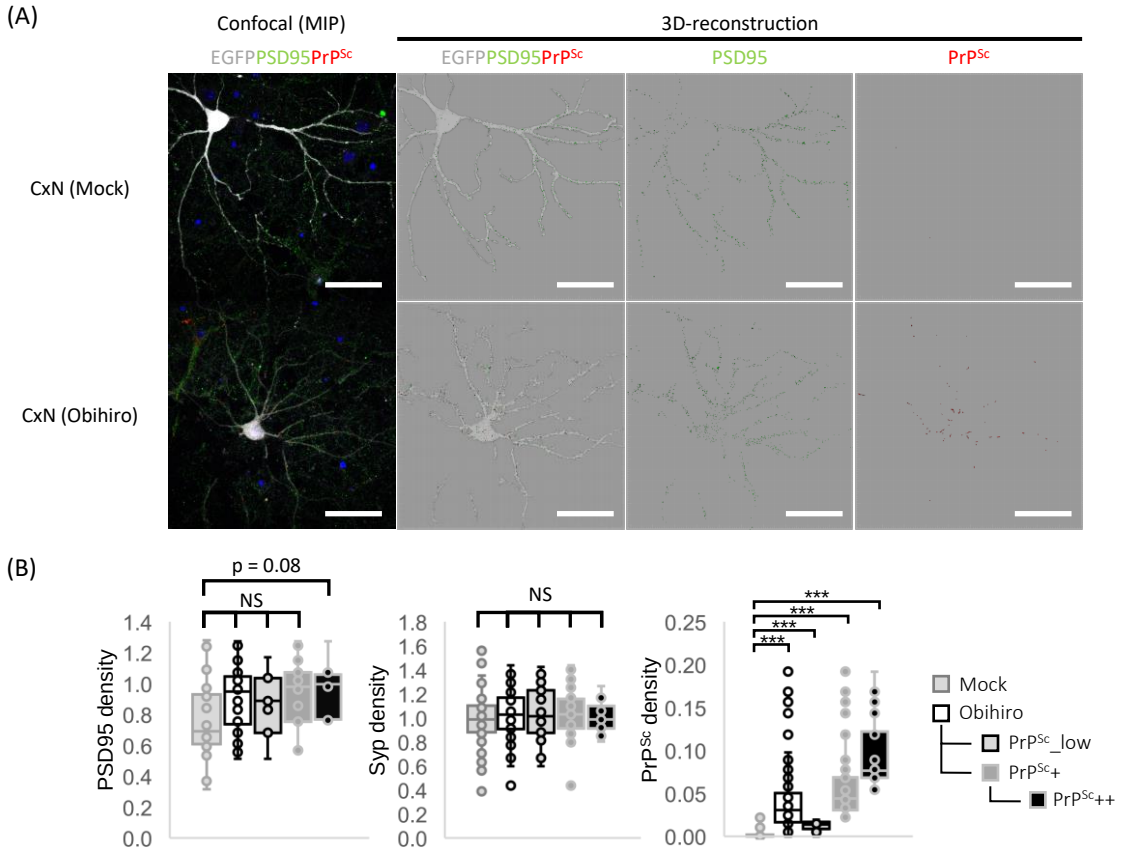

Figure I-9. Synapse densities of PrP^{Sc}-positive cortical neurons

CxNs were transduced with the rAAV for EGFP expression before immunostaining at 21 dpi. Z-series of confocal images at a final magnification of 315× were reconstructed in 3D-images for analysis using Imaris software. (A) Representative confocal images (MIP, maximum intensity projection) and 3D-images (surfaces) of EGFP-expressing neurons immunostained for PrP^{Sc} (with mAB 8D5) and PSD95 in CxNs. (B) Densities of PSD95-positive post-synaptic terminals, synaptophysin-positive pre-synaptic terminals, and PrP^{Sc} of cortical neurons in CxNs. The density was defined as the number of signals per a unit volume of cell. Obihiro-infected CxN were analyzed as a whole (Obihiro) and as three subpopulations classified by the PrP^{Sc} density of the cell. The rightmost graph shows the density of PrP^{Sc} from a representative data set used for pre-synapse quantification. The numbers of neurons used for this measurement were as follows: for the post-synaptic density measurement, 20 neurons from mock-infected CxN and 26 neurons from Obihiro-infected CxN were used (PrP^{Sc}_low, n = 7; PrP^{Sc}+, n = 19 including PrP^{Sc}++, n = 8). For the pre-synaptic density measurement, 73 neurons from mock-infected CxN and 78 neurons from Obihiro-infected CxN were used (PrP^{Sc}_low, n = 26; PrP^{Sc}+, n = 52 including PrP^{Sc}++, n = 19). Differences between the groups were analyzed by Steel's test using mock-infected neurons as control groups (NS, no significant differences; ***, $p < 0.001$).

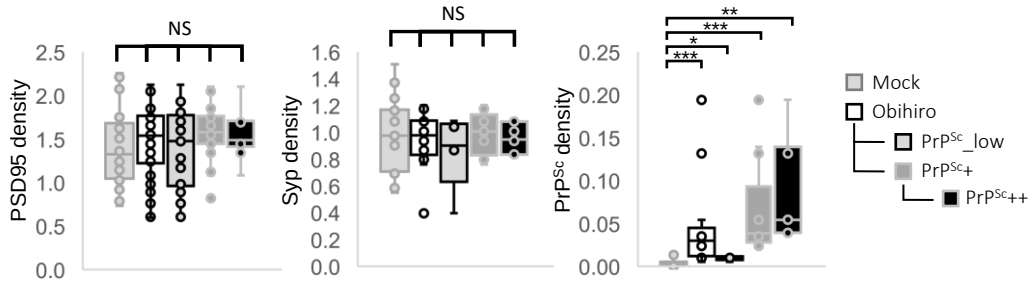

Figure I-10. Synapse densities of PrP^{Sc}-positive thalamic neurons

The densities of synaptic terminals of thalamic neurons in ThNs at 21 dpi were analyzed following the same procedure described in Figure I-9. The numbers of neurons used for this measurement were as follows: for the post-synaptic density measurement, 41 neurons from mock-infected ThN and 42 neurons from Obihiro-infected ThN were used (PrP^{Sc}_low, n = 19; PrP^{Sc}+, n = 23 including PrP^{Sc}++, n = 12). For the pre-synaptic density measurement, 18 neurons from mock-infected ThN and 18 neurons from Obihiro-infected ThN were used (PrP^{Sc}_low, n = 5; PrP^{Sc}+, n = 13 including PrP^{Sc}++, n = 7). Differences between the groups were analyzed by Steel's test using mock-infected neurons as control groups (NS, no significant differences; *, $p < 0.05$; **, $p < 0.01$; ***, $p < 0.001$).

DISCUSSION

Conversion of neuronal PrP^{C} into PrP^{Sc} is a central event that leads to neurodegenerative consequences in prion diseases [12-14]; however, the precise process of neurodegeneration and its molecular mechanisms remain unclear. While involvement of glial cells, especially of microglia, in the neuropathogenesis is getting evident [71, 72, 74], little is known about autonomous neuronal responses to prion propagation which may be a clue to understand the pathogenesis of prion diseases. Primary cell cultures prepared from mouse brains may serve as versatile ex vivo models to analyze molecular mechanisms of neurodegeneration caused by prion infection [81-83]; however, it is difficult to evaluate autonomous neuronal response to prion propagation due to the presence of astrocytes in those cultures, particularly if cultures are kept for long periods [81]. Thus, in the current study, I used neuron-enriched primary cultures from cortices and thalami by inhibiting astrocyte growth with AraC treatment, which inhibits astrocyte growth [84].

Previously, Cronier et al. observed an increase of fragmented nuclei that intimate apoptotic cell death in prion-infected cerebellar granule neurons (CGNs) of mice cultured on an astrocyte feeder layer [82]. Also, Hannaoui and colleagues reported decreases in the proportion of MAP2-positive neurons in prion-exposed CGNs from 14 to 21 days post exposure (dpe), as well as in striatal and cortical neuronal cultures from 7 to 11 dpe. They also disclosed that GFAP-positive astrocytes accounted for 20-30% of cells when neuronal losses were observed [81]. In contrast to these studies, no continuous decline of NeuN-positive neurons or MAP-2-positive neurite densities in prion-infected cells were observed in CxNs or ThNs infected with either the Chandler or Obihiro prion strains (Figure I-3), in spite of the continuous increasing of PrP-res levels over 28 dpi. Differences in experimental conditions, including mouse strains used for neuronal cultures and prion strains, may account for some of the inconsistency of observed neurotoxicity. One of critical differences between the previous studies and the current study was presence of astrocytes. Astrocytes can be infected with prions

and support the propagation and transmission of prions in cell cultures [65-67, 82] and change the microenvironment, which accelerates degeneration of prion-infected neurons [68]. Thus, it is possible that efficient prion propagation in primary neuronal cultures with astrocytes attributes to the differences in observed neurotoxicity.

Induction of ER stress, probably due to misfolded PrP, have been recognized by upregulation of ER chaperone proteins in the brains of patients with sporadic or variant CJD [59, 60] and prion-infected mice [59]. More recently, involvement of the PERK-eIF2α-ATF4 pathway of UPR in the pathogenesis of prion diseases has been demonstrated by experimental interventions to inhibit the PERK activity and/or to reduce the phosphorylation level of eIF2α, which successfully prolonged the survival of prion-infected transgenic mice overexpressing PrP [62, 63]. I analyzed the PERK pathway-related molecules to assess whether UPR is evoked in prion-infected CxNs and ThNs as an autonomous neuronal response. A fine analysis of individual neurons by IFA identified a positive correlation between the amounts of PrP^{Sc} and p-PERK in cortical neurons at 21 dpi (Figure I-7A-7C), indicating that the production of PrP^{Sc} directly provoked neuronal ER stress and enhanced phosphorylation of PERK as an autonomous neuronal response. ATF4 is a pivotal transcription factor for full activation of the PERK-eIF2α pathway ultimately transducing ER stress into a CHOP-mediated proapoptotic phase [91, 101]. Indeed, a time-dependent increase of CHOP level and increased translation of ATF4 in the brain of prion-infected transgenic mice suggest activation of this axis with the disease progression [62]. Interestingly, neither induction of ATF4 nor upregulation of its downstream genes was observed, even in PrP^{Sc}++ neurons in prion-infected CxNs and ThNs (Figure I-4D, I-7D & I-8D). These data suggest that ER stress and PERK phosphorylation are enhanced by prion propagation in a neuron-autonomous manner, whereas activation of downstream cascades in the PERK-eIF2α-ATF4 pathway will not take place as a consequence of an autonomous neuronal response to prion propagation.

Recently, Smith *et al.* have reported that activation of the PERK signaling pathway in

astrocytes changed their reactivity state into “UPR-reactive” state, which was harmful to neurons in mice with prion neurodegeneration [108]. They also showed that repression of this signaling exclusively in astrocytes by overexpressing an active fragment of GADD34 under the GFAP promoter using lentiviral vectors was able to prevent neuronal loss in the hippocampus and to prolong survival of the mice, providing evidence of a non-cell-autonomous mechanism of neurodegeneration in prion diseases. Given that the activation of glial cells is one of the most characteristic observations in the brain of animals and human suffering from prion diseases, it is likely that the activated microglia and/or astrocytes play intrinsic roles in the process of neurodegeneration in prion diseases [109-111]. In fact, depletion and inhibition of microglial activity altered disease progression of prion-infected mice [71-73]. Astrogliosis may also modify the neuropathological process of prion diseases [112-114]. In addition, there are several pieces of evidence for so-called “cross talk” [115, 116] between neurons and glial cells that regulates their activation states each other; transducing both neuroprotective and neurotoxic signals under pathological conditions [67, 117-120]. Therefore, additional stimuli, possibly from activated glial cells as non-autonomous factors, may be required for the full activation of the PERK-eIF2α-ATF4 pathway in the brains of prion-infected mice to proceed neurodegeneration observed in prion diseases.

Decrease in levels of synaptic proteins has been observed in brains prion-infected mice [32, 105, 121]. It is known that phosphorylation of eIF2α by p-PERK induces global repression of translation as a consequence of UPR [54], which targets include several synaptic proteins [62]. In neuron-enriched CxN and ThN at 21 dpi, when accumulation of PrP-res were obvious in those cultures, no differences were observed in the densities of PSD95- or synaptophysin-positive granular signals between mock-infected and prion-infected neurons, even in PrP^{Sc}++ neurons (Figure I-9 & I-10). These results suggest that not only selective translation of ATF4, but also repression of global protein synthesis was not autonomously induced in prion-infected neurons by PERK phosphorylation, consistent with no differences in p-eIF2α levels being

observed between mock- and prion-infected neurons at 21 dpi (Figure I-4). Incidentally, at 7 dpi, I found that phosphorylation levels of eIF2α were significantly higher, which coincided with decreased expression of several synaptic proteins, in prion-infected CxNs than in mock-infected CxNs in immunoblot analyses. This suggests that activation of UPR via p-PERK is somehow limited to a relatively early phase after exposure to prions, even though the ER stress and phosphorylation of PERK are sustained in prion-infected neurons. The importance of the early PERK-eIF2α pathway activation in neurodegenerative disorders has been also indicated by immunoreactivity of p-PERK in pre-tangle neurons rather than in neurons with neurofibrillary tangles in Alzheimer's disease (AD) [122] and in dopaminergic neurons with diffused α-synuclein in Parkinson's disease postmortem brains [123]. Although I focused on the later time point (21 dpi) when apparent PrP^{Sc} accumulation was observed in neurons, it is of interest if acute toxicity of PrP^{Sc} [33, 34, 100] or an immediate response of neurons to prions strongly stimulates the activation of PERK and its downstream pathways despite a significantly lower level of PrP^{Sc} accumulation than later time points.

In this chapter, I described induction of ER stress as genuine neuronal responses to prion propagation; however, it did not proceed to a pro-apoptotic phase nor synaptic loss autonomously in neurons *ex vivo*. These findings highlight the presence of additional non-neuronal factor(s) in the mechanism of neurodegeneration in prion diseases, which may provide clues for understanding of the pathogenesis and for therapeutics to prion diseases and other misfolding disorders.

SUMMARY

Conversion of PrP^{C} into PrP^{Sc} in neurons is one of the key pathophysiological events in prion diseases. However, the molecular mechanism of neurodegeneration in prion diseases has yet to be fully elucidated because of a lack of suitable experimental models for analyzing neuron-autonomous responses to prion infection. In the present study, I used neuron-enriched primary cultures of cortical and thalamic mouse neurons to analyze autonomous neuronal responses to prion infection. PrP^{Sc} levels in neurons increased over the time after prion infection; however, no obvious neuronal losses or neurite alterations were observed. Interestingly, a finer analysis of individual neurons co-stained with PrP^{Sc} and p-PERK, the early cellular response of the PERK- eIF2α pathway, demonstrated a positive correlation between the number of PrP^{Sc} granular stains and p-PERK granular stains, in cortical neurons at 21 dpi. Although the phosphorylation of PERK was enhanced in prion-infected cortical neurons, there was no sign of subsequent translational repression of synaptic protein synthesis or activations of downstream UPR in the PERK-eIF2α pathway. These results suggest that PrP^{Sc} production in neurons induces ER stress in a neuron-autonomous manner; however, it does not fully activate UPR in prion-infected neurons. These findings provide insights into the autonomous neuronal responses to prion propagation and the involvement of neuron-non-autonomous factor(s) in the mechanisms of neurodegeneration in prion diseases.

CHAPTER II

Analysis of the neuron-autonomous responses to prion-infected neurons by transcriptome analysis

INTRODUCTION

Conversion of PrP^{C} into PrP^{Sc} in neurons is one of the key events in the pathogenesis of prion diseases. A number of studies has been carried out to elucidate mechanisms for pathogenesis of prion diseases; however, cellular and molecular mechanisms of the neurodegeneration remain to be elucidated yet [62]. Identification of host factors differentially expressed in prion-infected tissues and neurons will contribute to elucidation of the mechanism for pathogenesis of prion diseases. Earlier studies on comprehensive gene expression analysis using microarray have identified differentially expressed genes in brains of prion-infected mice [124], natural sheep scrapie cases [125], and human sporadic CJD cases [126] in the clinical phase of the diseases. These genes included Cathepsin S, C1q B chain of complement, apolipoprotein D [127], β_2-microglobulin, F4/80, metallothionein II [128], and α-hemoglobin stabilizing factor (*Edrf*) [129]. Unfortunately, alterations of the gene expressions were not attributed to changes in neurons but mostly to reactive glial cell responses.

The next generation sequencing technology and bioinformatics tools have boosted investigations of gene expression profiles in the brains of patients and animals affected by prions. However, it is still difficult to identify alterations of transcripts in neurons affected by prion propagation from the tissue transcriptome, since the use of whole brain tissue may dilute modest changes in the gene expression occurring in a specific brain region or specific cell types. Moreover, the brain tissue transcriptome will be heavily influenced by changes in constituent cell populations in the brain that are caused by neuronal loss and proliferation of microglia [130-132].

There have been several attempts to unveil the authentic neuronal responses during the course of prion diseases. Microdissection of the lesions may be effective in identifying disease-specific changes in those regions [131, 133]; however, it is still difficult to distinguish neuron-specific responses from transcriptome changes in the lesions. Cell sorting is another method

though it is not easy to separate neurons [134, 135]. In the last decade, bioinformatics projects have made rapid progress in establishing cell-type specific transcriptomics and proteomics resources [136-139]. By utilizing these data sources, several groups have realized selective analyses of so-called “cell type-enriched genes”, though the genes analyzed were limited to only a part of the whole transcriptome instead. Neuron-specific transcriptome will be of interest to understand genuine neuronal responses to prion propagation and to understand pathogenesis of prion diseases; however, no data available to date.

In Chapter I, I described that phosphorylation of PERK, the initial molecular event of UPR, was evoked in the prion-infected primary neurons as a neuron-autonomous response to prion propagation. This finding suggests that prion propagation affects neuronal homeostasis, and alterations other than UPR may also be induced in neurons by prion propagation as neuron-autonomous responses, even though such alterations would be insufficient to lead neuronal cell death *ex vivo*. Therefore, in Chapter II, I performed transcriptome analysis of prion-infected neuron-enriched cultures to identify any neuron-autonomous responses to prion infection using next generation sequencing.

MATERIALS & METHODS

1. RNA extraction

Primary cultures of cortical and thalamic neurons were prepared and infected with Obihiro strain of mouse-adapted scrapie prion as described in Chapter I. Total RNA was extracted with TRIzol reagent (Invitrogen) from neurons cultured in an area of 7.0 cm^2 at 14 and 21 dpi. Concentration and quality of each RNA pellet resuspended in nuclease-free water (NFW) was measured by nanodrop (Thermo Scientific) and 2100 Bioanalyzer with the Agilent RNA6000 Nano Kit (Agilent Technologies). RNA samples which the RNA Integrity Number (RIN) [140] were higher than 7.0 were used to construct cDNA libraries.

2. Purification of mRNA for RNA-sequencing (RNA-Seq)

To concentrate mRNA for RNA-Seq, 500 ng of the total RNA was used as a start material for each sample. Ribosomal RNA (rRNA) were removed from the total RNA using Low Input RiboMinus Eukaryote System v2 (Thermo Fisher Scientific) according to the manufacturer's instructions. Briefly, total RNA was denatured at 70°C for 10 min then incubated with RiboMinus Eukaryote Probe Mix labeled with biotin, at 37°C for 20 min. The samples were incubated with RiboMinus Magnetic Beads conjugated with streptavidin, at 37°C for 5 min to capture rRNA hybridized with the biotinylated probes. The rRNA captured with magnetic beads in the samples was removed using Magnetic Stand. The rRNA depleted total RNA samples were concentrated using Nucleic Acid Binding Beads (Thermo Fisher Scientific). To remove small RNAs, the samples were incubated with 2.5 M LiCl at 4°C for 2.5 hrs and centrifuged at 22,500 × *g* at 4 for 30 min. After washing with 75% ethanol, the pellets were dissolved into 12 µl of NFW. Removal of 18s and 28s rRNAs and small RNAs were confirmed using Bioanalyzer with Agilent RNA 6000 Pico Kit.

3. Synthesis of cDNA libraries

The whole transcriptome cDNA libraries were synthesized from the purified mRNA samples using Ion Total RNA-Seq Kit v2 (Thermo Fisher Scientific) according to the manufacturer's instructions with some modifications. The mRNA was fragmented with RNase III at 37°C for 5 min and immediately purified using Nucleic Acid Binding Beads. The size distribution of the fragmented RNA was analyzed using Bioanalyzer. RNA samples were concentrated into 3 μl by centrifugal vacuum concentrator (Eppendorf) for next procedure. Ion Adaptor mix v2 containing random hexamers with adaptor nucleotides were hybridized with the fragmented RNA at 65°C for 10 min followed by incubation at 30°C for 5min. The ligation reaction of the adaptor-hybridized fragmented RNA was performed at 30°C for 1 h. After denaturing the samples at 70°C for 10 min, reverse transcription was performed using Ion RT Primer v2 and 10 × SuperScript III Enzyme Mix at 42°C for 30 min. The synthesized cDNA libraries were purified using Nucleic Acid Binding Beads, eluted in 12 μl of NFW and amplified by PCR using Ion Xpress RNA 3' Barcode Primer. After purification of the amplified cDNA samples, the size distribution and molar concentration of the cDNA libraries were measured by Bioanalyzer using Agilent High Sensitivity DNA Kit (Agilent Technologies).

4. Sequencing by Ion Proton

The amplified cDNA samples were adjusted to 10 nM and equal volume of four samples were mixed for each run of sequencing. The mixture of the samples was adjusted to 100 pM before it was subjected to preparation of the template by Ion OneTouch 2 Instrument and Ion OneTouch ES module using with Ion PI Hi-Q OT2 200 Kit (Thermo Fisher Scientific). The templates were sequenced using Ion pI Hi-Q Sequencing 200 Kit and Ion PI Chip Kit v3 on Ion Proton System (Thermo Fisher Scientific) to a depth of ≥ 20 million reads for each sample.

5. Data analysis

Ion Torrent Suit software version 5.0.2.1 (Thermo Fisher Scientific) was used to separate out the data for each sample based on their 3' barcodes. Ion Torrent Suit was also used to align the RNA-Seq data to the mm10 mouse reference genome (UCSC) and generate bam files to export to StrandNGS software v2.1 (Strand Life Sciences). Using Strand NGS, the RNA-Seq data were annotated by Ensemble ver. 14.03.01 and reads were quantified and normalized by DESeq method [141] baselined to the mean of all samples. At the quantification, the reads were filtered by using quality criteria (read length ≥ 26 nucleotides and mapping quality ≥ 20). StrandNGS was also used for expression analyses including calculation of fold change (FC) and statistical significance, clustering analysis, and describing Venn diagram. Because there was no candidate gene using False Discovery Rate = 0.1, I chose as criteria an unadjusted p-value < 0.05 by paired *t* test for selecting potential differentially expressed genes in this study. Data were further analyzed for Gene Ontology [142] (the Gene Ontology Consortium, http://www.geneontology.org) using MetaScape (http://metascape.org) [143] and QuickGO (https://www.ebi.ac.uk/QuickGO/) [144] online software packages. Ingenuity Pathway Analysis (QIAGEN, www.qiagen.com/ingenuity) was used for pathway analysis to find unique biological processes that differentially regulated in prion-infected neurons.

RESULTS AND DISCUSSION

II-i. Identification of neuronal genes expressed differentially by prion infection in neuron-enriched primary cultures of cortical and thalamic neurons.

For the transcriptome analysis of prion-infected neurons, CxNs and thalamic neurons ThNs were prepared and infected with Obihiro strain as described in Chapter I. Complementary DNA (cDNA) libraries were constructed from ribosomal and small RNAs-removed mRNA pools from three independent primary cultures at 14 and 21 dpi when a substantial amount of PrP^{Sc} was detected in CxNs and ThNs (Figure I-2). Mock-infected, and dpi-matched CxNs and ThNs were used as control samples in each experiment. RNA-Seq data were acquired and pre-processed as described in Materials & Methods section in this chapter. I confirmed the neuron-enrichment in these primary cultures with AraC-treatment in terms of transcriptome based on the normalized RPKM (Read count per Kilobase of exon per Million reads) values (Figure II-1); expression levels of cell marker genes for neurons (*Tubb3, Nefh, Nefm, Nefl, and Rbfox3*) were generally high. Compared with these neuronal markers, expression of astrocyte (*Aldh1l1, Gfap, S100b, and Sox9*) and microglia (*Itgam, Cx3cr1, Cd68, and Aif1l*) marker genes were detected at much lower levels. In addition, there was no increased expression of glial markers in prion-infected neurons. The selective expression of marker genes for neurons such as *Tubb3*, *Nfh*, and *Rbfox3* was consistent with the results of IFA in Figure I-1 in Chapter I.

Relative gene expression levels were determined as normalized signal values (NSVs) which represent log2-formatted expression values normalized between samples by DeSeq method [141] using StrandNGS software. A total of 38,887 genes were identified, and those genes expressed at extremely low levels (read count per kilobase exon per million reads, RPKM, were less than 0.1 in all of the 24 samples) were filtered out. From the remaining genes, those coding proteins (19,208 genes) were finally submitted for a hierarchal clustering analysis (Figure II-2A).

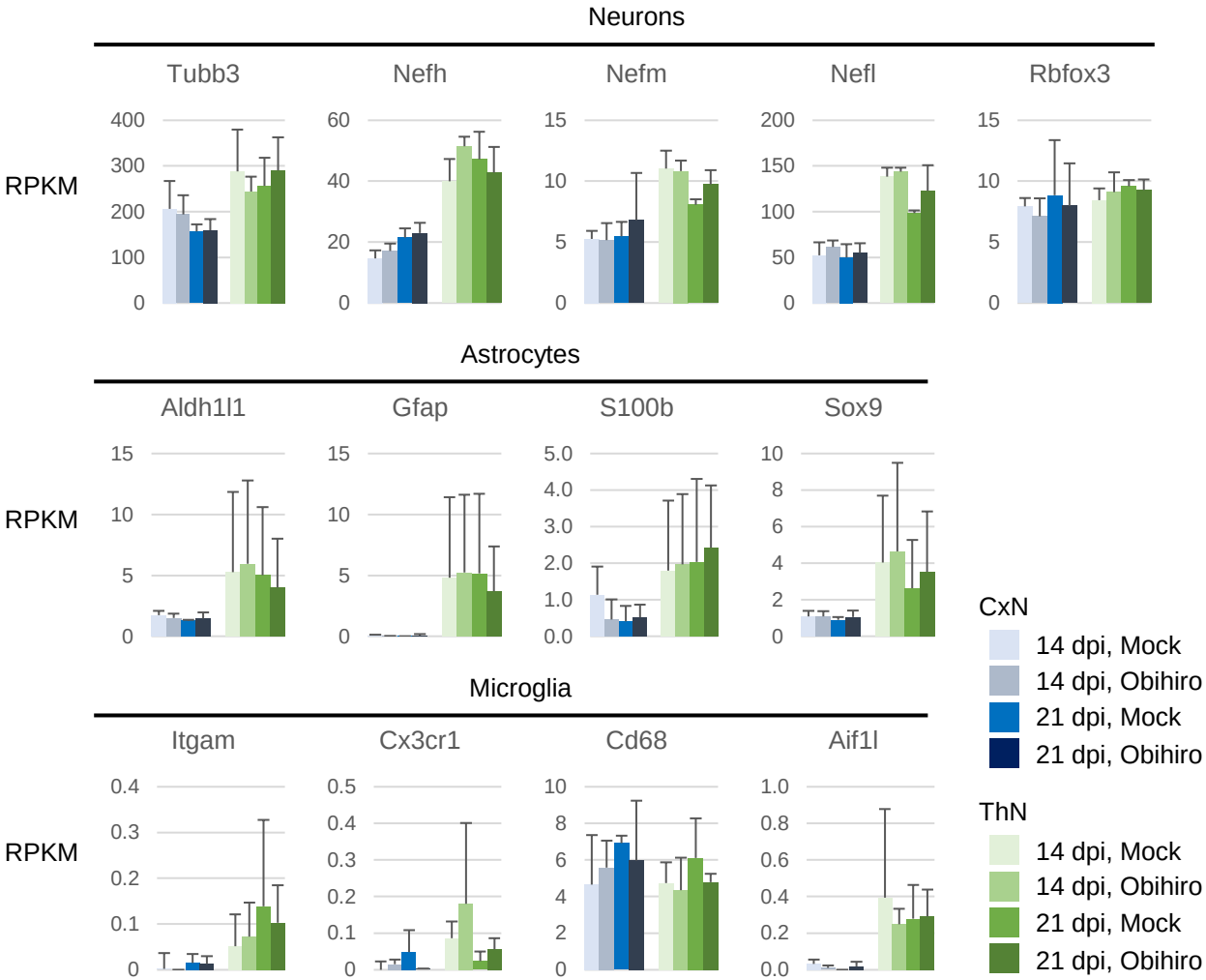

Figure II-1. Expression levels of cell marker genes.
The RPKM values of representative cell marker genes for neurons (*Tubb3*, *Nefh*, *Nefm*, *Nefl*, and *Rbfox3*), astrocytes (*Aldh1l1*, *Gfap*, *S100b*, and *Sox9*) and microglia (*Itgam*, *Cx3cr1*, *Cd68*, and *Aif1l*). Data are shown as mean ± SD of biological triplicates.

The hierarchical clustering analysis of the 24 samples (CxNs or ThNs, 14 or 21 dpi, biological triplicates) showed that they were clearly divided into region-specific clusters, CxNs and ThNs, but were not into prion-infection specific clusters (Figure II-2A). There were four unique gene clusters (i-iv); gene clusters i & ii were composed of genes with high expression in CxNs but low in expression in ThNs, and clusters iii & iv were composed of genes with high expression in ThNs but low expression in CxNs. The clustering analysis revealed that a large number of genes were expressed excessively in either CxNs or ThNs, suggesting that these *ex vivo* cultures had unique transcriptomic features reflecting brain regions. Additionally, no clusters that distinguished prion-infected neurons from mock-infected neurons was generated, suggesting the impact of prion propagation on CxNs and ThNs would be mild even if it happened.

Although the impact of prion propagation on the whole gene expression profile in neurons seemed to be limited, I carefully looked into the neuronal transcriptome to find any characteristic alteration caused by prions. Concerning a possible influence of the uneven distribution of gene expression between CxNs and ThNs on the normalization, hereafter I separately analyzed one neuronal type from another to optimize the normalization and gene selection. NSVs of genes identified in CxNs were re-calculated and protein-coding genes except for those expressed at an extremely low level (RPKM < 0.1 in all of the 12 samples) were selected for following analyses to identify neuron-autonomous alterations induced by prion infection (18,016 genes, Figure II-2B). As for ThNs, 18,297 genes were selected in the same way.

The changes in an expression level of each gene was determined as fold change (FC) which was calculated as NSV[Obihiro]/NSV[Mock] for genes upregulated in Obihiro-infected neurons, and as $-(\mathrm{NSV[Obihiro]/NSV[Mock]})^{-1}$ for genes downregulated in Obihiro-infected neurons. Because there was no candidate gene using false discovery rate = 0.1, I chose as

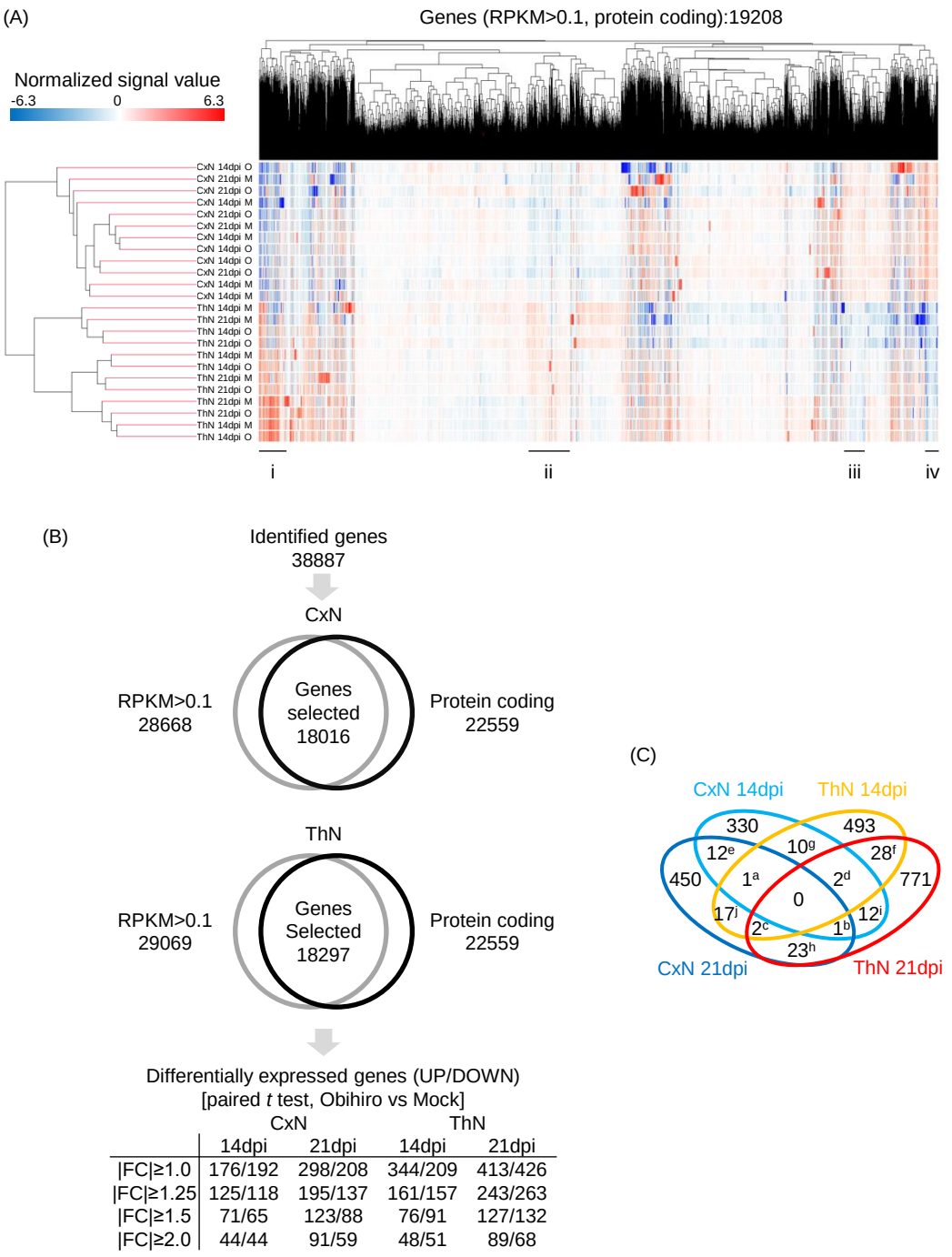

	CxN		ThN	
	14dpi	21dpi	14dpi	21dpi
|FC|≥1.0	176/192	298/208	344/209	413/426
|FC|≥1.25	125/118	195/137	161/157	243/263
|FC|≥1.5	71/65	123/88	76/91	127/132
|FC|≥2.0	44/44	91/59	48/51	89/68

Figure II-2. Identification of differentially expressed genes in prion-infected CxN and ThN.
(A) Hierarchical clustering of samples (left) and genes (top) based on sample conditions (combination of a neuronal type and dpi) and expression levels (normalized signal values, NSVs) of the genes meeting the following criteria: protein-coding, and RPKM ≥ 0.1 in at least 1 of 24 samples. The clustering was performed using Euclidean distance coefficient metric and Ward's linkage rule on StrandNGS (Strand Life Sciences). The heatmap shows NSVs of the genes with color intensity as indicated on right of the heatmap. Underbars i-iv highlight gene clusters that characterize each of neuronal types (CxN, cortical neurons; ThN, thalamic neurons). M, mock-infected; O, Obihiro-infected. (B) Selection of genes used for bioinformatics analysis. Genes expressed at extremely low levels in all samples of CxN or ThN were removed from a total of 38,887 identified genes, then protein-coding genes were selected to proceed to fold change calculation. A difference in expression is represented as fold change (FC) that is calculated as NSV[Obihiro]/NSV[Mock] for genes upregulated in Obihiro-infected neurons, and as $-$(NSV[Obihiro]/NSV[Mock])$^{-1}$ for genes downregulated in Obihiro-infected neurons. Differentially expressed genes between Obihiro- and mock-infected neurons were chosen by paired *t*-test ($p < 0.05$) in which dpi-matched mock- and Obihiro-infected neurons from the same experiment were paired for a comparison. (C) Venn diagram illustrating overlap of differentially expressed genes across conditions. Genes differentially expressed in at least 2 conditions are indicated with indexes (a-h) and further described in Table II-1 and Figure II-3.

criteria an unadjusted p-value < 0.05 by paired *t* test for selecting potential differentially expressed genes in this study. The differentially expressed genes were defined as a gene which absolute fold change was greater than 1.0 ($|FC| \geq 1.0$) with a p-value < 0.05 by paired t test in which dpi-matched, Obihiro- and mock-infected neurons from the same experiment were paired for a comparison.

Figure II-2B shows the numbers of differentially expressed genes in prion-infected CxNs and ThNs that displayed equal to or greater than absolute fold change of |1.0|-, |1.25|-, |1.5|-, and |2.0|-folds in expression. For instance, a total of 368 genes were differentially expressed in prion-infected CxNs at 14 dpi; of those, 176 genes were upregulated (among them, 44 genes were 2-fold upregulated), and 192 genes were downregulated (44 genes were 2-fold downregulated). Some of the differentially expressed genes were common in prion-infected neurons in several conditions. As represented with small letter-indexes in the Venn's diagram (Figure II-2C), 6 genes (a, *Vars*; b, *Gm8444*; c, *Slc30a2* and *Rangrf*; d, *Otud7b* and *Dlec1*) were differentially expressed over three experimental conditions). A total of 108 genes were included in the overlap across 2 or 3 conditions (indexes a-h). Brief description and accession numbers (Ensembl Gene IDs) are listed in Table II-1. Figure II-3 describes expression patterns of these 108 differentially expressed genes in each of experimental conditions (CxNs at 14 and 21 dpi, ThNs at 14 and 21dpi). Among the 108 genes, *Pin 4* was downregulated both in CxNs (FC = -2.54) and ThNs (FC = -2.09) at 21 dpi; *Unc119b* was upregulated both in CxNs (FC = 1.49) and ThNs (FC = 1.37) at 21 dpi; *Bcl2l11* was upregulated in CxNs at 14 (FC = 1.32) and 21 dpi (1.46); *Ppme1* and *Ncstn* were upregulated in ThNs at 14 (FC = 1.13 and FC = 1.24, respectively) and 21 dpi (FC = 1.19 and FC = 1.26, respectively). Most of the 108 genes have not been reported as differentially expressed genes in the transcriptome analyses of tissues from prion-infected animals, except for 4 genes, *Pmch* [145], *Robo1* [131], *Ubtf* [125], and *Ctsz* [145-147]. The expression levels of these genes were low; therefore, it might have been hidden

Table II-1. Differentially expressed genes in prion-infected neurons across conditions

Index	Gene Symbol	Description	Ensembl ID
A	Vars	valyl-tRNA synthetase	ENSMUSG00000007029
B	Gm8444	predicted gene 8444	ENSMUSG00000069439
C	Slc30a2	solute carrier family 30 (zinc transporter), member 2	ENSMUSG00000028836
	Rangrf	RAN guanine nucleotide release factor	ENSMUSG00000032892
D	Otud7b	OTU domain containing 7B	ENSMUSG00000038495
	Dlec1	deleted in lung and esophageal cancer 1	ENSMUSG00000038060
E	Bcl2l11	BCL2-like 11 (apoptosis facilitator)	ENSMUSG00000027381
	Tomm34	translocase of outer mitochondrial membrane 34	ENSMUSG00000018322
	Acp6	acid phosphatase 6, lysophosphatidic	ENSMUSG00000028093
	Gm12666	predicted gene 12666	ENSMUSG00000066107
	Gtf2h1	general transcription factor II H, polypeptide 1	ENSMUSG00000006599
	Fadd	Fas (TNFRSF6)-associated via death domain	ENSMUSG00000031077
	Cd24a	CD24a antigen	ENSMUSG00000047139
	Tdg	thymine DNA glycosylase	ENSMUSG00000034674
	Pmch	pro-melanin-concentrating hormone	ENSMUSG00000035383
	Kcnj12	potassium inwardly-rectifying channel, subfamily J, member 12	ENSMUSG00000042529
	Naa35	N(alpha)-acetyltransferase 35, NatC auxiliary subunit	ENSMUSG00000021555
	Ppm1b	protein phosphatase 1B, magnesium dependent, beta isoform	ENSMUSG00000061130
F	Ncstn	nicastrin	ENSMUSG00000003458
	Mfsd7b	feline leukemia virus subgroup C cellular receptor 1	ENSMUSG00000066595
	Gpr155	G protein-coupled receptor 155	ENSMUSG00000041762
	Tchh	trichohyalin	ENSMUSG00000052415
	Khdrbs1	KH domain containing, RNA binding, signal transduction associated 1	ENSMUSG00000028790
	Faap20	Fanconi anemia core complex associated protein 20	ENSMUSG00000073684
	Ube2j2	ubiquitin-conjugating enzyme E2J 2	ENSMUSG00000023286
	Paics	phosphoribosylaminoimidazole carboxylase, phosphoribosylaminoribosylaminoimidazole, succinocarboxamide synthetase	ENSMUSG00000029247
	2610524H06Rik	RIKEN cDNA 2610524H06 gene	ENSMUSG00000092486
	Pde6h	phosphodiesterase 6H, cGMP-specific, cone, gamma	ENSMUSG00000064330
	Aebp2	AE binding protein 2	ENSMUSG00000030232
	Slco1a6	solute carrier organic anion transporter family, member 1a6	ENSMUSG00000079262
	Zfp28	zinc finger protein 28	ENSMUSG00000062861
	Trim28	tripartite motif-containing 28	ENSMUSG00000005566
	Trappc6a	trafficking protein particle complex 6A	ENSMUSG00000002043
	Ppme1	protein phosphatase methylesterase 1	ENSMUSG00000030718
	Lcmt1	leucine carboxyl methyltransferase 1	ENSMUSG00000030763
	Fam198a	golgi associated kinase 1A	ENSMUSG00000038233
	Gid4	GID complex subunit 4, VID24 homolog	ENSMUSG00000018415
	Cdc6	cell division cycle 6	ENSMUSG00000017499
	Ubtf	upstream binding transcription factor, RNA polymerase I	ENSMUSG00000020923
	Nrde2	nrde-2 necessary for RNA interference, domain containing	ENSMUSG00000021179
	Robo1	roundabout guidance receptor 1	ENSMUSG00000022883
	Tead3	TEA domain family member 3	ENSMUSG00000002249
	Stk19	serine/threonine kinase 19	ENSMUSG00000061207
	Enpp4	ectonucleotide pyrophosphatase/phosphodiesterase 4	ENSMUSG00000023961
	Minar2	membrane integral NOTCH2 associated receptor 2	ENSMUSG00000050875
	Pcna-ps2	proliferating cell nuclear antigen pseudogene 2	ENSMUSG00000067608
G	Coq10b	coenzyme Q10B	ENSMUSG00000025981
	Ppp6c	protein phosphatase 6, catalytic subunit	ENSMUSG00000026753
	Lrrc8d	leucine rich repeat containing 8D	ENSMUSG00000046079
	Tmem194	nuclear envelope integral membrane protein 1	ENSMUSG00000040195
	Gm17541	ribosomal protein L18A pseudogene	ENSMUSG00000091732
	Akap8	A kinase (PRKA) anchor protein 8	ENSMUSG00000024045
	Gstp2	glutathione S-transferase, pi 2	ENSMUSG00000038155
	Fibp	fibroblast growth factor (acidic) intracellular binding protein	ENSMUSG00000024911
	Gm2174	predicted gene 2174	ENSMUSG00000058932
	Rpl36a	ribosomal protein L36A	ENSMUSG00000079435

Table II-1 (continued)

Index	Gene Symbol	Description	Ensembl ID
H	Rasal2	RAS protein activator like 2	ENSMUSG00000070565
	Fjx1	four jointed box 1	ENSMUSG00000075012
	Gm9396	predicted gene 9396	ENSMUSG00000063328
	Pnrc1	proline-rich nuclear receptor coactivator 1	ENSMUSG00000040128
	Epb4.1l4b	erythrocyte membrane protein band 4.1 like 4b	ENSMUSG00000028434
	Kmt2c	lysine (K)-specific methyltransferase 2C	ENSMUSG00000038056
	Unc119b	unc-119 lipid binding chaperone B	ENSMUSG00000046562
	Slc23a4	solute carrier family 23 member 4	ENSMUSG00000029847
	Chd2	chromodomain helicase DNA binding protein 2	ENSMUSG00000078671
	St5	suppression of tumorigenicity 5	ENSMUSG00000031024
	Acsl1	acyl-CoA synthetase long-chain family member 1	ENSMUSG00000018796
	Lace1	AFG1 like ATPase	ENSMUSG00000038302
	Mrm1	mitochondrial rRNA methyltransferase 1	ENSMUSG00000018405
	Fgd3	FYVE, RhoGEF and PH domain containing 3	ENSMUSG00000037946
	Uggt2	UDP-glucose glycoprotein glucosyltransferase 2	ENSMUSG00000042104
	Gga1	golgi associated, gamma adaptin ear containing, ARF binding protein 1	ENSMUSG00000033128
	Prpf40b	pre-mRNA processing factor 40B	ENSMUSG00000023007
	Kctd5	potassium channel tetramerisation domain containing 5	ENSMUSG00000016946
	A930017K11Rik	RIKEN cDNA A930017K11 gene	ENSMUSG00000025727
	Lbh	limb-bud and heart	ENSMUSG00000024063
	Greb1l	growth regulation by estrogen in breast cancer-like	ENSMUSG00000042942
	Slmo1	PRELI domain containing 3A	ENSMUSG00000024530
	Pin4	protein (peptidyl-prolyl cis/trans isomerase) NIMA-interacting, 4 (parvulin)	ENSMUSG00000079480
I	Klf11	Kruppel-like factor 11	ENSMUSG00000020653
	Nfil3	nuclear factor, interleukin 3, regulated	ENSMUSG00000056749
	3830408C21Rik	RIKEN cDNA 3830408C21 gene	ENSMUSG00000071181
	Ift88	intraflagellar transport 88	ENSMUSG00000040040
	Ppl	periplakin	ENSMUSG00000039457
	Apool	apolipoprotein O-like	ENSMUSG00000025525
	Ivns1abp	influenza virus NS1A binding protein	ENSMUSG00000023150
	Srsf6	serine/arginine-rich splicing factor 6	ENSMUSG00000016921
	Ubqln4	ubiquilin 4	ENSMUSG00000008604
	Zfp691	zinc finger protein 691	ENSMUSG00000045268
	Stx12	syntaxin 12	ENSMUSG00000028879
	Utp20	UTP20 small subunit processome component	ENSMUSG00000004356
J	Agap1	ArfGAP with GTPase domain, ankyrin repeat and PH domain 1	ENSMUSG00000055013
	Ctsz	cathepsin Z	ENSMUSG00000016256
	Ralyl	RALY RNA binding protein-like	ENSMUSG00000096025
	Acad9	acyl-Coenzyme A dehydrogenase family, member 9	ENSMUSG00000027710
	Gbp7	guanylate binding protein 7	ENSMUSG00000040253
	Ccne2	cyclin E2	ENSMUSG00000028212
	Frmpd1	FERM and PDZ domain containing 1	ENSMUSG00000035615
	Dhdds	dehydrodolichyl diphosphate synthase	ENSMUSG00000012117
	Sparcl1	SPARC-like 1	ENSMUSG00000029309
	Cd97	adhesion G protein-coupled receptor E5	ENSMUSG00000002885
	Crtap	cartilage associated protein	ENSMUSG00000032431
	Lcp2	lymphocyte cytosolic protein 2	ENSMUSG00000002699
	Gm17330	predicted gene, 17330	ENSMUSG00000095329
	Bnip5	BCL2 interacting protein 5	ENSMUSG00000048905
	Ldlrad4	low density lipoprotein receptor class A domain containing 4	ENSMUSG00000024544
	Setbp1	SET binding protein 1	ENSMUSG00000024548
	Upf3b	UPF3 regulator of nonsense transcripts homolog B (yeast)	ENSMUSG00000036572

Differentially expressed genes in prion-infected neurons across several conditions were listed with their gene symbols, brief descriptions, and gene IDs (Ensembl ID). Expression levels and p values by paired t test for these genes are given in Figure II-2.

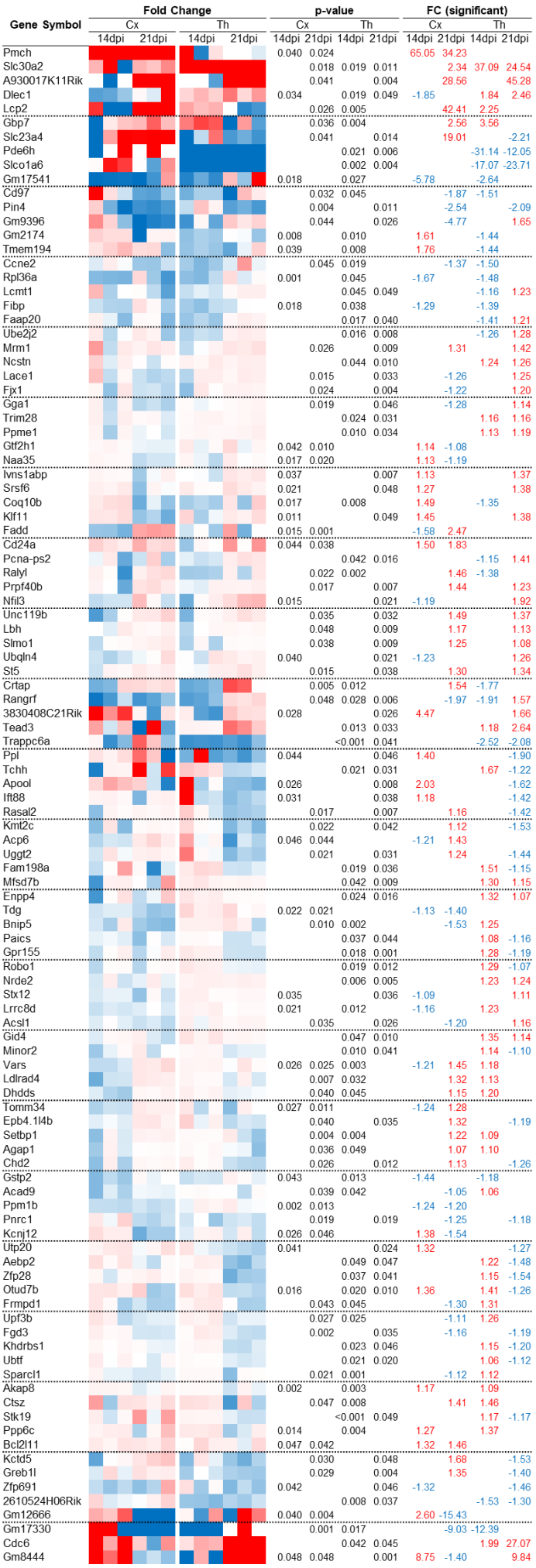

Gene Symbol	Fold Change				p-value				FC (significant)			
	Cx		Th		Cx		Th		Cx		Th	
	14dpi	21dpi	14dpi	21dpi	14dpi	21dpi	14dpi	21dpi	14dpi	21dpi	14dpi	21dpi
Pmch					0.040	0.024			65.05	34.23		
Slc30a2						0.018	0.019	0.011		2.34	37.09	24.54
A930017K11Rik						0.041		0.004		28.56		45.28
Dlec1					0.034		0.019	0.049	-1.85		1.84	2.46
Lcp2						0.026	0.005			42.41	2.25	
Gbp7						0.036	0.004			2.56	3.56	
Slc23a4						0.041		0.014		19.01		-2.21
Pde6h							0.021	0.006			-31.14	-12.05
Slco1a6							0.002	0.004			-17.07	-23.71
Gm17541					0.018		0.027		-5.78		-2.64	
Cd97						0.032	0.045			-1.87	-1.51	
Pin4						0.004		0.011		-2.54		-2.09
Gm9396						0.044		0.026		-4.77		1.65
Gm2174					0.008		0.010		1.61		-1.44	
Tmem194					0.039		0.008		1.76		-1.44	
Ccne2						0.045	0.019			-1.37	-1.50	
Rpl36a					0.001		0.045		-1.67		-1.48	
Lcmt1							0.045	0.049			-1.16	1.23
Fibp					0.018		0.038		-1.29		-1.39	
Faap20							0.017	0.040			-1.41	1.21
Ube2j2							0.016	0.008			-1.26	1.28
Mrm1						0.026		0.009		1.31		1.42
Ncstn							0.044	0.010			1.24	1.26
Lace1						0.015		0.033		-1.26		1.25
Fjx1						0.024		0.004		-1.22		1.20
Gga1						0.019		0.046		-1.28		1.14
Trim28							0.024	0.031			1.16	1.16
Ppme1							0.010	0.034			1.13	1.19
Gtf2h1					0.042	0.010			1.14	-1.08		
Naa35					0.017	0.020			1.13	-1.19		
Ivns1abp					0.037			0.007	1.13			1.37
Srsf6					0.021			0.048	1.27			1.38
Coq10b					0.017		0.008		1.49		-1.35	
Klf11					0.011			0.049	1.45			1.38
Fadd					0.015	0.001			-1.58	2.47		
Cd24a					0.044	0.038			1.50	1.83		
Pcna-ps2							0.042	0.016			-1.15	1.41
Ralyl						0.022	0.002			1.46	-1.38	
Prpf40b						0.017		0.007		1.44		1.23
Nfil3					0.015			0.021	-1.19			1.92
Unc119b						0.035		0.032		1.49		1.37
Lbh						0.048		0.009		1.17		1.13
Slmo1						0.038		0.009		1.25		1.08
Ubqln4					0.040			0.021	-1.23			1.26
St5						0.015		0.038		1.30		1.34
Crtap						0.005	0.012			1.54	-1.77	
Rangrf						0.048	0.028	0.006		-1.97	-1.91	1.57
3830408C21Rik					0.028			0.026	4.47			1.66
Tead3							0.013	0.033			1.18	2.64
Trappc6a							<0.001	0.041			-2.52	-2.08
Ppl					0.044			0.046	1.40			-1.90
Tchh							0.021	0.031			1.67	-1.22
Apool					0.026			0.008	2.03			-1.62
Ift88					0.031			0.038	1.18			-1.42
Rasal2						0.017		0.007		1.16		-1.42
Kmt2c						0.022		0.042		1.12		-1.53
Acp6					0.046	0.044			-1.21	1.43		
Uggt2						0.021		0.031		1.24		-1.44
Fam198a							0.019	0.036			1.51	-1.15
Mfsd7b							0.042	0.009			1.30	1.15
Enpp4							0.024	0.016			1.32	1.07
Tdg					0.022	0.021			-1.13	-1.40		
Bnip5						0.010	0.002			-1.53	1.25	
Paics							0.037	0.044			1.08	-1.16
Gpr155							0.018	0.001			1.28	-1.19
Robo1							0.019	0.012			1.29	-1.07
Nrde2							0.006	0.005			1.23	1.24
Stx12					0.035			0.036	-1.09			1.11
Lrrc8d					0.021		0.012		-1.16		1.23	
Acsl1						0.035		0.026		-1.20		1.16
Gid4							0.047	0.010			1.35	1.14
Minor2							0.010	0.041			1.14	-1.10
Vars					0.026	0.025	0.003		-1.21	1.45	1.18	
Ldlrad4						0.007	0.032			1.32	1.13	
Dhdds						0.040	0.045			1.15	1.20	
Tomm34					0.027	0.011			-1.24	1.28		
Epb4.1l4b						0.040		0.035		1.32		-1.19
Setbp1						0.004	0.004			1.22	1.09	
Agap1						0.036	0.049			1.07	1.10	
Chd2						0.026		0.012		1.13		-1.26
Gstp2					0.043		0.013		-1.44		-1.18	
Acad9						0.039	0.042			-1.05	1.06	
Ppm1b					0.002	0.013			-1.24	-1.20		
Pnrc1						0.019		0.019		-1.25		-1.18
Kcnj12					0.026	0.046			1.38	-1.54		
Utp20					0.041			0.024	1.32			-1.27
Aebp2							0.049	0.047			1.22	-1.48
Zfp28							0.037	0.041			1.15	-1.54
Otud7b					0.016		0.020	0.010	1.36		1.41	-1.26
Frmpd1						0.043	0.045			-1.30	1.31	
Upf3b						0.027	0.025			-1.11	1.26	
Fgd3						0.002		0.035		-1.16		-1.19
Khdrbs1							0.023	0.046			1.15	-1.20
Ubtf							0.021	0.020			1.06	-1.12
Sparcl1						0.021	0.001			-1.12	1.12	
Akap8					0.002		0.003		1.17		1.09	
Ctsz						0.047	0.008			1.41	1.46	
Stk19							<0.001	0.049			1.17	-1.17
Ppp6c					0.014		0.004		1.27		1.37	
Bcl2l11					0.047	0.042			1.32	1.46		
Kctd5						0.030		0.048		1.68		-1.53
Greb1l						0.029		0.004		1.35		-1.40
Zfp691					0.042			0.046	-1.32			-1.46
2610524H06Rik							0.008	0.037			-1.53	-1.30
Gm12666					0.040	0.004			2.60	-15.43		
Gm17330						0.001	0.017			-9.03	-12.39	
Cdc6							0.042	0.045			1.99	27.07
Gm8444					0.048	0.048		0.001	8.75	-1.40		9.84

Figure II-3. Genes differentially expressed in prion-infected neurons.
The heatmap displays the difference in gene expression in Obihiro-infected neurons from mock-infected neurons as average Fold Change (FC) of three independent experiments. The mean normalized signal value of each gene is mapped to a color-intensity value shown in the color-range on the right of the heatmap. The genes were ordered as the result of hierarchical clustering on the expression pattern over samples. The middle column displays p-values computed by paired *t* test without no multiple testing correction carried out that compared Obihiro-infected and Mock-infected neurons from the same neuronal type, dpi, and sequencing date. The absolute values of fold change satisfying p-value cut-off 0.05 were displayed in the right column.

behind the prominent upregulation of glia-derived genes in the transcriptome analyses of brain tissues of animals infected with prions. Although the information on the association of the 108 genes with prion diseases are limited, 10 of the 108 genes have been reported to be directly or indirectly involved in neuronal disorders and functional abnormalities in the brain including AD (*Ncstn* [148], *Ppme1* [149, 150]), multiple sclerosis (*Cd24*) [151], amyotrophic lateral sclerosis (*Ubqln4* [152]), epilepsy (*Chd2* [153]), learning disorder (*Robo1* [154]), autism (*Agap1* [155], *Gstp2* [156], *Upf3b* [157]), and neurodegeneration with brain atrophy (*Ubtf* [158]). Our laboratory has acquired tissue transcriptome data from thalamus of prion-infected mice at pre-clinical and clinical stages of the disease (conducted by Dr. Yamasaki and Ms. Shimakura, unpublished data). Based on normalized RPKM values (nRPKM) in the tissue transcriptome, I confirmed upregulation of *Ncstn* (mean ± SD of nRPKM = 12.3 ± 0.9 in mock-infected mice versus nRPKM = 13.2 ± 1.0 and 15.4 ± 0.7 in Obihiro- and Chandler-infected mice, respectively) and *Bcl2l11* (nRPKM = 1.3 ± 0.4 in mock-infected mice versus nRPKM = 2.5 ± 1.7 and 2.3 ± 0.8 in Obihiro- and Chandler-infected mice respectively).

Ncstn encodes Nicastrin, a type I transmembrane glycoprotein that is a constitutive component of the multimeric gamma-secretase complex [159]. This endoprotease complex is known to catalyze the intramembrane cleavage of integral membrane proteins such as Notch receptors and amyloid precursor protein [160]. While there is no report that indicates association of the function of Nicastrin with prion diseases, several genetic variants of *Ncstn* have been found in familial and sporadic AD patients [161-164] and inhibition of Nicastrin restricted amyloid deposition in a mouse model of AD [148], implying a possible association of *Ncstn* with the development of AD. In this study, *Ncstn* was upregulated in prion-infected ThNs at 14 and 21 dpi. Additionally, transcriptome analysis of the thalamus of Obihiro-infected mice showed that the expression of *Ncstn* tended to be upregulated in the thalamus of Obihiro-

infected mice at a clinical stage (unpublished data), suggesting the implication of *Ncstn* in the pathogenesis of prion diseases.

Another gene of my interest is *Bcl2l11*, which showed significant upregulation in prion-infected CxNs (14 and 21 dpi) as well as tendency toward upregulation in prion-infected ThNs at 14 dpi, as well as in the thalamus of Obihiro-infected mice at a clinical stage (unpublished data). *Bcl2l11*, also known as *Bim*, encodes a pro-apoptotic protein that belongs to the Bcl2 family. Induction of *Bcl2l11* expression has been observed in mouse models of Parkinson's disease [165, 166] and amyotrophic lateral sclerosis [167] that also showed facilitated neurodegenerative manifestations. *Bcl2l11* is also founded to be upregulated in postmortem brain tissues of AD patients [168, 169]. Regarding prion diseases, drug-mediated inhibition of cAbl-MST1-Bim pathway alleviated the neurotoxicity of PrP106-126 fragment [170], also suggesting that Bcl2l11 functions as a neurotoxic mediator in prion diseases.

II-ii. Biological characterization of the differentially expressed genes in prion-infected neurons.

To gain insight into biological characteristics of the differentially expressed genes, I annotated the genes with Gene Ontology (GO)[142] using MetaScape online software package [143]. Of the 243 genes differentially regulated by $|FC| \geq 1.25$ in CxNs at 14 dpi, 228 genes had known biological functions and were subjected to a biological process GO enrichment analysis. GO and Kyoto encyclopedia of genes and genomes (KEGG) terms (Reactome knowledgebase [171], https://reactome.org/) enriched in prion-infected CxNs at 14 dpi were associated with processes of immune cells and molecules, nucleotide metabolism, and neurofunctions such as lymphocyte apoptotic process (GO:0070227), regulation of type I interferon-mediated signaling pathway (GO:0060338), purine nucleotide catabolic process (GO:0006195), pyrimidine nucleobase metabolic process (GO:0006206), and regulation of behavior (GO: 0050795) (Table II-2-1).

Table II-2-1. GO terms enriched in genes differentially expressed (|FC|≥1.25) in prion-infected CxN at 14 dpi

Cluster	Term	Description	-LogP	InTerm /InList	Genes in list
1	GO:0043029	T cell homeostasis	3.98	5/46	Bcl2l11,Cd24a,Fadd,Rag1,Chst3
	GO:0070227	**Lymphocyte apoptotic process**	3.29	6/98	Bcl2l11,Cd24a,Fadd,Rag1,Ripk1,Traf3ip2
	GO:0002260	Lymphocyte homeostasis	2.91	5/78	Bcl2l11,Cd24a,Fadd,Rag1,Chst3
	GO:0071887	Leukocyte apoptotic process	2.62	6/132	Bcl2l11,Cd24a,Fadd,Rag1,Ripk1,Traf3ip2
	GO:0070231	T cell apoptotic process	2.53	4/58	Bcl2l11,Fadd,Rag1,Ripk1
2	R-MMU-5357786	TNFR1-induced proapoptotic signaling	3.66	3/12	Fadd,Ripk1,Otud7b
	GO:0060544	Regulation of necroptotic process	3.19	3/17	Fadd,Ripk1,Ybx3
	GO:0060338	**Regulation of type I interferon-mediated signaling pathway**	2.69	3/25	Fadd,Mmp12,Samhd1
	GO:0010939	Regulation of necrotic cell death	2.54	3/28	Fadd,Ripk1,Ybx3
	GO:0070266	Necroptotic process	2.46	3/30	Fadd,Ripk1,Ybx3
3	GO:1901136	Carbohydrate derivative catabolic process	3.62	7/120	Mmp12,Pnliprp2,Samhd1,Nudt9,Dpyd,Dera,Pde5a
	GO:0072523	Purine-containing compound catabolic process	3.14	4/40	Samhd1,Nudt9,Dpyd,Pde5a
	GO:0006195	**Purine nucleotide catabolic process**	2.54	3/28	Samhd1,Nudt9,Pde5a
4	R-MMU-8956319	Nucleobase catabolism	3.36	4/35	Samhd1,Tymp,Nudt9,Dpyd
	GO:0006206	**Pyrimidine nucleobase metabolic process**	2.97	3/20	Ctps,Tymp,Dpyd
	GO:0006213	Pyrimidine nucleoside metabolic process	2.64	3/26	Ctps,Tymp,Dpyd
	R-MMU-15869	Metabolism of nucleotides	2.47	5/98	Ctps,Samhd1,Tymp,Nudt9,Dpyd
5	GO:0048739	Cardiac muscle fiber development	3.19	3/17	Myh11,Tcap,Obsl1
6	R-MMU-5576891	Cardiac conduction	2.79	6/122	Kcnj12,Kcnq1,Atp2a3,Atp1a2,Kcnj14,Npr2
	R-MMU-397014	Muscle contraction	2.64	7/176	Kcnj12,Kcnq1,Tcap,Atp2a3,Atp1a2,Kcnj14,Npr2
7	GO:0050795	**Regulation of behavior**	2.51	5/96	Crh,Mc4r,Rag1,Opn4,Pmch
8	GO:0060537	Muscle tissue development	2.44	12/474	Csrp2,Fadd,Fhl2,Myh11,Mapk11,Ripk1,Tcap,Ybx3,Cdon,Rps6kb1, Obsl1,Cenpf
9	GO:0048535	Lymph node development	2.41	3/31	Fadd,Ltb,Cd248

GO and KEGG terms in Reactome knowledgebase (https://reactome.org/) enriched in the differentially expressed genes in prion-infected CxN at 14 dpi (-LogP > 2.3, equivalent to $p < 0.005$). The enriched terms were hierarchically clustered based on their gene memberships by Metascape (http://metascape.org), and representative terms in each cluster are listed with accession numbers, brief descriptions, and the numbers and names of genes in a data list of the differentially expressed genes used for the analysis.

As for CxNs at 21 dpi, 303 of the 331 differentially expressed genes (|FC| ≥ 1.25) had known biological functions. The enrichment analysis showed that GO terms also related to processes of immune cells and molecules, such as activated T cell proliferation (GO:0050798), regulation of T cell activation (GO:0050863). In addition, GO terms in other categories such as regulation of cysteine-type endopeptidase activity (GO:2000116) were enriched at 21 dpi, implying that not only immune processes, but also the caspase-mediated apoptotic processes were possibly affected by prion infection in cortical neurons (Table II-2-2). The enrichment of genes related to the cysteine-type peptidase activity was previously reported in mice infected with several strains of prions [147].

In ThNs at 14 dpi, 281 of the 318 differentially expressed genes with |FC| ≥ 1.25 were annotated with known functions represented by GO and/or KEGG terms, and the terms enriched in those genes were related to lipid metabolism (lipid localization, GO:0010876 and glycerolipid metabolic process, GO:0046486) and glycosylphosphatidylinositol (GPI)-anchored protein synthesis (glycoprotein biosynthetic process, GO:0009101, and post-translational modification: synthesis of GPI-anchored proteins, R-MMU-163125). At 21 dpi, 466 of the 506 differentially expressed genes (|FC| ≥ 1.25) in prion-infected ThNs were annotated with known biological functions. The enriched GO and KEGG terms at 21 dpi also had association with lipid metabolism (positive regulation of lipid transport, GO:0032370), translocation of proteins to the membrane (regulation of protein localization to cell surface, GO:2000008; endosome to plasma membrane protein transport, GO:0099638) (Table II-2-3 & 2-4). Implication of lipid metabolism-related biological functions were also suggested in patients of sporadic CJD [126] and mice infected with prions [147]. In addition, considering that the neuronal PrP^{Sc} was primarily found around the plasma membrane [84], the pathways involved in the lipid metabolism and transport can be a target for further investigation.

Table II-2-2. GO terms enriched in genes differentially expressed (|FC|>1.5) in prion-infected CxN at 21dpi

Cluster	Term	Description	-LogP	InTerm /InList	Gene Symbols
1	GO:0010950	Positive regulation of endopeptidase activity	4.35	10/153	Rhoa,Bcl2l11,Fadd,Ccn1,Psme3,Syk,Bok,Dap,St18,Aim2
	GO:0010952	Positive regulation of peptidase activity	4.14	10/162	Rhoa,Bcl2l11,Fadd,Ccn1,Psme3,Syk,Bok,Dap,St18,Aim2
	GO:2001056	Positive regulation of cysteine-type endopeptidase activity	4.01	9/136	Rhoa,Bcl2l11,Fadd,Ccn1,Syk,Bok,Dap,St18,Aim2
	GO:2000116	**Regulation of cysteine-type endopeptidase activity**	3.58	11/226	Rhoa,Bcl2l11,Fadd,Ccn1,Syk,Bok,Bcl2l12,Dap,Lamp3,St18,Aim2
	GO:0052548	Regulation of endopeptidase activity	3.16	13/337	Rhoa,Bcl2l11,Fadd,Ccn1,Psme3,Syk,Bok,Bcl2l12,Dap,Serpina3f, Lamp3,St18,Aim2
	GO:0043280	Positive regulation of cysteine-type endopeptidase activity involved in apoptotic process	2.93	7/119	Rhoa,Bcl2l11,Ccn1,Syk,Bok,Dap,St18
	GO:0052547	Regulation of peptidase activity	2.84	14/411	Rhoa,Bcl2l11,Fadd,Ccn1,Psme3,Syk,Bok,Bcl2l12,Dap,Serpina3f, Lamp3,St18,Wfikkn2,Aim2
	GO:0043281	Regulation of cysteine-type endopeptidase activity involved in apoptotic process	2.76	9/202	Rhoa,Bcl2l11,Ccn1,Syk,Bok,Bcl2l12,Dap,Lamp3,St18
2	GO:0050870	Positive regulation of T cell activation	4.31	11/187	Rhoa,Cd24a,Fadd,H2-T23,Igf2,Il4ra,Syk,Tgfb1,Lgals8,Pdcd1lg2, Dock8
	GO:1903039	Positive regulation of leukocyte cell-cell adhesion	3.99	11/203	Rhoa,Cd24a,Fadd,H2-T23,Igf2,Il4ra,Syk,Tgfb1,Lgals8,Pdcd1lg2, Dock8
	GO:0050798	**Activated T cell proliferation**	3.38	5/47	Cd24a,Fadd,Igf2,Pdcd1lg2,Itgad
	GO:0022409	Positive regulation of cell-cell adhesion	3.33	11/242	Rhoa,Cd24a,Fadd,H2-T23,Igf2,Il4ra,Syk,Tgfb1,Lgals8,Pdcd1lg2, Dock8
	GO:0032946	Positive regulation of mononuclear cell proliferation	3.24	8/138	Cd24a,Fadd,H2-T23,Igf2,St6gal1,Syk,Pdcd1lg2,Gpr183
	GO:0070665	Positive regulation of leukocyte proliferation	3.10	8/145	Cd24a,Fadd,H2-T23,Igf2,St6gal1,Syk,Pdcd1lg2,Gpr183
	GO:0050863	**Regulation of T cell activation**	3.00	12/307	Rhoa,Cd24a,Fadd,H2-T23,Igf2,Il4ra,Syk,Tgfb1,Trex1,Lgals8, Pdcd1lg2,Dock8
	GO:0045785	Positive regulation of cell adhesion	2.83	14/412	Rhoa,Cd24a,Fadd,H2-T23,Igf2,Ccn1,Il4ra,Syk,Tgfb1,Epb41l4b, Lgals8,Pdcd1lg2,Smoc2,Dock8
	GO:0046631	Alpha-beta T cell activation	2.82	8/160	Rhoa,Cd24a,H2-T23,Il4ra,Syk,Tgfb1,Psmb11,Gpr183
	GO:0046006	Regulation of activated T cell proliferation	2.78	4/38	Cd24a,Fadd,Igf2,Pdcd1lg2
	GO:1903037	Regulation of leukocyte cell-cell adhesion	2.73	11/287	Rhoa,Cd24a,Fadd,H2-T23,Igf2,Il4ra,Syk,Tgfb1,Lgals8,Pdcd1lg2, Dock8
	GO:0042098	T cell proliferation	2.70	9/206	Cd24a,Fadd,H2-T23,Igf2,Syk,Tgfb1,Pdcd1lg2,Dock8,Itgad
	GO:0042102	Positive regulation of T cell proliferation	2.67	6/98	Cd24a,Fadd,H2-T23,Igf2,Syk,Pdcd1lg2
	GO:0046635	Positive regulation of alpha-beta T cell activation	2.62	5/69	Rhoa,Cd24a,H2-T23,Il4ra,Syk
	GO:0050671	Positive regulation of lymphocyte proliferation	2.60	7/136	Cd24a,Fadd,H2-T23,Igf2,Syk,Pdcd1lg2,Gpr183
	GO:0022407	Regulation of cell-cell adhesion	2.54	13/395	Rhoa,Cd24a,Fadd,H2-T23,Igf2,Il4ra,Jag1,Swap70,Syk,Tgfb1, Lgals8,Pdcd1lg2,Dock8
	GO:0046641	Positive regulation of alpha-beta T cell proliferation	2.51	3/22	Cd24a,H2-T23,Syk
	GO:0042110	T cell activation	2.51	15/495	Rhoa,Cd24a,Fadd,H2-T23,Igf2,Il4ra,Syk,Tgfb1,Trex1,Lgals8, Pdcd1lg2,Psmb11,Dock8,Gpr183,Itgad
	GO:0046634	Regulation of alpha-beta T cell activation	2.48	6/107	Rhoa,Cd24a,H2-T23,Il4ra,Syk,Tgfb1
	GO:0032943	Mononuclear cell proliferation	2.46	11/311	Cd24a,Fadd,H2-T23,Igf2,St6gal1,Syk,Tgfb1,Pdcd1lg2,Dock8, Gpr183,Itgad
	GO:0032944	Regulation of mononuclear cell proliferation	2.42	9/227	Cd24a,Fadd,H2-T23,Igf2,St6gal1,Syk,Tgfb1,Pdcd1lg2,Gpr183
	GO:0007159	Leukocyte cell-cell adhesion	2.38	11/319	Rhoa,Cd24a,Fadd,H2-T23,Igf2,Il4ra,Syk,Tgfb1,Lgals8,Pdcd1lg2, Dock8
	GO:0046632	Alpha-beta T cell differentiation	2.33	6/115	Rhoa,Il4ra,Syk,Tgfb1,Psmb11,Gpr183
	GO:0042104	Positive regulation of activated T cell proliferation	2.30	3/26	Cd24a,Fadd,Igf2
3	R-MMU-397014	Muscle contraction	3.84	10/176	Itgb5,Kcnj12,Myh3,Ryr1,Abcc9,Tnnt1,Tnnt2,Corin,Rangrf,Kcnk13
4	GO:0043029	T cell homeostasis	3.43	5/46	Bcl2l11,Cd24a,Fadd,Tgfb1,Cacna1f
	GO:0002260	Lymphocyte homeostasis	3.19	6/78	Bcl2l11,Cd24a,Fadd,Tgfb1,Slc40a1,Cacna1f
	GO:0001776	Leukocyte homeostasis	3.14	7/110	Bcl2l11,Cd24a,Fadd,Tgfb1,Slc40a1,Cacna1f,Gpr183
5	GO:0031032	Actomyosin structure organization	3.33	10/204	Rhoa,Edn1,Itgb5,Tnnt1,Tnnt2,Epb41l4b,Ankrd23,Ppfia1,Cdc42bpg, Kank4
6	GO:0042832	Defense response to protozoan	2.96	4/34	Il4ra,Tspan32,Gbp7,Gbp11
	GO:0001562	Response to protozoan	2.78	4/38	Il4ra,Tspan32,Gbp7,Gbp11
7	GO:0007229	Integrin-mediated signaling pathway	2.89	6/89	Rhoa,Itgb5,Syk,Tec,Tspan32,Itgad
8	GO:0009150	Purine ribonucleotide metabolic process	2.72	14/423	Adcy6,Ak2,Ampd3,Rhoa,Atp5f1,Myh3,Sucla2,Tgfb1,Trex1,Acss2, Acot12,Acot4,Afg1l,Acot6
	GO:0009259	Ribonucleotide metabolic process	2.63	14/433	Adcy6,Ak2,Ampd3,Rhoa,Atp5f1,Myh3,Sucla2,Tgfb1,Trex1,Acss2, Acot12,Acot4,Afg1l,Acot6
	GO:0055086	Nucleobase-containing small molecule metabolic process	2.59	18/635	Adcy6,Ak2,Ampd3,Rhoa,Atp5f1,Myh3,Sucla2,Tgfb1,Trex1,Acss2, Acot12,Tgds,Nadsyn1,Acot4,Aox2,Afg1l,Acot6,Cyb5r4
	GO:0072521	Purine-containing compound metabolic process	2.55	15/490	Adcy6,Ak2,Ampd3,Rhoa,Atp5f1,Myh3,Sucla2,Tgfb1,Trex1,Acss2, Acot12,Acot4,Aox2,Afg1l,Acot6
	GO:0006163	Purine nucleotide metabolic process	2.50	14/447	Adcy6,Ak2,Ampd3,Rhoa,Atp5f1,Myh3,Sucla2,Tgfb1,Trex1,Acss2, Acot12,Acot4,Afg1l,Acot6
	GO:0019693	Ribose phosphate metabolic process	2.48	14/450	Adcy6,Ak2,Ampd3,Rhoa,Atp5f1,Myh3,Sucla2,Tgfb1,Trex1,Acss2, Acot12,Acot4,Afg1l,Acot6
	GO:0009117	Nucleotide metabolic process	2.43	16/555	Adcy6,Ak2,Ampd3,Rhoa,Atp5f1,Myh3,Sucla2,Tgfb1,Trex1,Acss2, Acot12,Nadsyn1,Acot4,Afg1l,Acot6,Cyb5r4
	GO:0006753	Nucleoside phosphate metabolic process	2.36	16/564	Adcy6,Ak2,Ampd3,Rhoa,Atp5f1,Myh3,Sucla2,Tgfb1,Trex1,Acss2, Acot12,Nadsyn1,Acot4,Afg1l,Acot6,Cyb5r4
9	GO:0043931	Ossification involved in bone maturation	2.63	3/20	Rhoa,Ryr1,Rflna
	GO:0070977	Bone maturation	2.51	3/22	Rhoa,Ryr1,Rflna
	mmu04921	Oxytocin signaling pathway	2.32	7/153	Adcy6,Rhoa,Kcnj12,Kcnj5,Ryr1,Cacna1f,Raf1
	GO:0048799	Animal organ maturation	2.30	3/26	Rhoa,Ryr1,Rflna
10	GO:0036336	Dendritic cell migration	2.63	3/20	Slamf8,Dock8,Gpr183
11	GO:0000271	Polysaccharide biosynthetic process	2.46	5/75	Igf2,Tgfb1,Extl3,Pask,B3gnt6
12	GO:0035813	Regulation of renal sodium excretion	2.40	3/24	Edn1,Anpep,Corin
	GO:0035812	Renal sodium excretion	2.30	3/26	Edn1,Anpep,Corin
13	GO:0090305	Nucleic acid phosphodiester bond hydrolysis	2.36	6/113	Endog,Parn,Mei4,Dxo,Fan1,Edc3
14	GO:1903671	Negative regulation of sprouting angiogenesis	2.35	3/25	Rhoa,Klf2,E2f2
15	GO:0030728	Ovulation	2.35	3/25	Inhbb,Pgr,Gpr149
16	GO:0072337	Modified amino acid transport	2.35	3/25	Slc22a21,Slc6a8,Slc5a6

GO and KEGG terms in Reactome knowledgebase (https://reactome.org/) enriched in the differentially expressed genes in prion-infected CxN at 21 dpi (-LogP > 2.3, equivalent to $p < 0.005$). The enriched terms were hierarchically clustered based on their gene memberships by Metascape (http://metascape.org), and representative terms in each cluster are listed with accession numbers, brief descriptions, and the numbers and names of genes in a data list of the differentially expressed genes used for the analysis.

Table II-2-3. GO terms enriched in genes differentially expressed (|FC|≥1.25) in prion-infected ThN at 14dpi

Cluster	Term	Description	-LogP	InTerm /InList	Genes in list
1	GO:0006066	Alcohol metabolic process	4.23	14/314	Pcbd1,Dpm1,Gpd1,Ntsr1,Sord,Hnf1a,Dhrs4,Angptl3,Tm7sf2, Akr7a5,Acer2,Disp3,Ip6k3,Gm9745
	GO:1901615	Organic hydroxy compound metabolic process	3.76	17/481	Pcbd1,Dpm1,Gpd1,Ntsr1,Sord,Hnf1a,Slc27a2,Dhrs4,Slco1a6, Angptl3,Tm7sf2,Akr7a5,Acer2,Disp3,Ip6k3,Rtl4,Gm9745
	GO:0044283	Small molecule biosynthetic process	2.70	18/652	Cnp,Pcbd1,Gpd1,Ntsr1,Sord,Sephs2,Hnf1a,Nr1h2,Slc27a2,Nupr1, Coq10b,Hacd2,Tm7sf2,Acly,Acer2,Ip6k3,Gm9745,Gm3839
	GO:0019751	Polyol metabolic process	2.38	6/118	Pcbd1,Ntsr1,Sord,Angptl3,Acer2,Ip6k3
2	R-MMU-212436	Generic Transcription Pathway	3.39	21/717	Ccne2,Kras,Mnat1,Ncor2,Supt4a,Nr1h2,Skp2,Sfn,Zfp235,Yeats4, Taf12,Rffl,Tmem219,Med6,Dek,Zfp809,Hist1h3c,Hist1h2ap, Hist1h2af,Hist1h2bh,Zfp967
	R-MMU-212165	Epigenetic regulation of gene expression	2.49	6/112	Phf1,Dek,Hist1h3c,Hist1h2ap,Hist1h2af,Hist1h2bh
	R-MMU-212300	PRC2 methylates histones and DNA	2.48	5/78	Phf1,Hist1h3c,Hist1h2ap,Hist1h2af,Hist1h2bh
3	GO:0000079	Regulation of cyclin-dependent protein serine/threonine kinase activity	2.63	5/72	Ccne2,Mnat1,Cdc6,Sfn,Bccip
	R-MMU-69052	Switching of origins to a post-replicative state	2.62	4/44	Ccne2,Mcm7,Cdc6,Skp2
	GO:1904029	Regulation of cyclin-dependent protein kinase activity	2.53	5/76	Ccne2,Mnat1,Cdc6,Sfn,Bccip
	R-MMU-68949	Orc1 removal from chromatin	2.41	3/25	Mcm7,Cdc6,Skp2
4	GO:0010876	**Lipid localization**	2.49	12/371	Ntsr1,Hnf1a,Tex2,Nr1h2,Esyt1,Slc27a2,Slco1a6,Angptl3,Osbpl9, Atp8b5,Serac1,Rft1
	GO:0006869	Lipid transport	2.42	11/331	Ntsr1,Hnf1a,Tex2,Nr1h2,Esyt1,Slc27a2,Slco1a6,Osbpl9,Atp8b5, Serac1,Rft1
5	GO:0009101	**Glycoprotein biosynthetic process**	2.48	10/278	Dpm1,Galnt3,Hs3st1,Alg2,Krtcap2,B3galnt2,Acot8,Hs3st2,Acer2, Gal3st4
	GO:1901137	Carbohydrate derivative biosynthetic process	2.30	16/601	Dpm1,Galnt3,Gpd1,Hs3st1,Nupr1,Alg2,Krtcap2,Pigx,B3galnt2,Acly, Acot8,Hs3st2,Gmds,Acer2,Gal3st4,Gm3839
6	GO:0046486	**Glycerolipid metabolic process**	2.47	11/326	Dpm1,Fgf7,Gpd1,Nr1h2,Angptl3,Pi4k2b,Gdpd3,Pigx,Serinc5,Ip6k3, Serac1
7	R-MMU-163125	**Post-translational modification: synthesis of GPI-anchored proteins**	2.36	5/83	Dpm1,Ceacam9,Prnd,Pigx,Art3

GO and KEGG terms in Reactome knowledgebase (https://reactome.org/) enriched in the differentially expressed genes in prion-infected ThN at 14 dpi (-LogP > 2.3, equivalent to p < 0.005). The enriched terms were hierarchically clustered based on their gene memberships by Metascape (http://metascape.org), and representative terms in each cluster are listed with accession numbers, brief descriptions, and the numbers and names of genes in a data list of the differentially expressed genes used for the analysis.

Table II-2-4. GO terms enriched in genes differentially expressed (|FC|≥1.25) in prion-infected ThN at 21dpi

Cluster	Term	Description	-LogP	InTerm /InList	Genes in list
1	GO:2000010	Positive regulation of protein localization to cell surface	4.11	5/22	Cd247,Erbb4,Commd1,Abca7,Rangrf
	GO:2000008	**Regulation of protein localization to cell surface**	3.70	6/41	Cd247,Cdh1,Erbb4,Commd1,Abca7,Rangrf
	GO:0034394	Protein localization to cell surface	2.59	6/66	Cd247,Cdh1,Erbb4,Commd1,Abca7,Rangrf
2	GO:0060314	Regulation of ryanodine-sensitive calcium-release channel activity	3.55	4/16	Dmd,Fkbp1b,Pkd2,Jsrp1
3	mmu05203	Viral carcinogenesis	3.41	14/231	Cdkn2b,Atf6b,Egr2,Egr3,H2-Q10,H2-Q4,H2-T22,Hdac3,Rbl1,Rbl2, Hist1h4d,Hist1h4n,Hist1h2bm,Hist4h4
	R-MMU-212165	Epigenetic regulation of gene expression	2.60	8/112	Aebp2,Myo1c,Polr1a,Cd3eap,Hist1h4d,Hist1h4n,Hist1h2bm,Hist4h4
	R-MMU-73772	RNA Polymerase I Promoter Escape	2.47	7/93	Ercc3,Polr1a,Cd3eap,Hist1h4d,Hist1h4n,Hist1h2bm,Hist4h4
	R-MMU-5250913	Positive epigenetic regulation of rRNA expression	2.44	7/94	Myo1c,Polr1a,Cd3eap,Hist1h4d,Hist1h4n,Hist1h2bm,Hist4h4
	R-MMU-5250924	B-WICH complex positively regulates rRNA expression	2.44	7/94	Myo1c,Polr1a,Cd3eap,Hist1h4d,Hist1h4n,Hist1h2bm,Hist4h4
	GO:0045653	Negative regulation of megakaryocyte differentiation	2.30	3/17	Hist1h4d,Hist1h4n,Hist4h4
4	GO:0046697	Decidualization	3.15	4/20	Cdh1,Il11ra1,Ptgis,Ash1l
	GO:0001893	Maternal placenta development	2.42	4/31	Cdh1,Il11ra1,Ptgis,Ash1l
5	GO:0034655	Nucleobase-containing compound catabolic process	3.14	20/426	Rida,Khk,Ppara,Zfp36,Nt5e,Esrrb,Lsm4,Zbtb20,Exosc3,Nudt16l1, Rnaseh2c,Exosc8,Brf1,Gale,Nudt17,Csdc2,Mettl14,Dcp1b,Lin28b, Gm5519
	GO:0044270	Cellular nitrogen compound catabolic process	2.63	20/470	Rida,Khk,Ppara,Zfp36,Nt5e,Esrrb,Lsm4,Zbtb20,Exosc3,Nudt16l1, Rnaseh2c,Exosc8,Brf1,Gale,Nudt17,Csdc2,Mettl14,Dcp1b,Lin28b, Gm5519
	GO:0046700	Heterocycle catabolic process	2.57	20/476	Rida,Khk,Ppara,Zfp36,Nt5e,Esrrb,Lsm4,Zbtb20,Exosc3,Nudt16l1, Rnaseh2c,Exosc8,Brf1,Gale,Nudt17,Csdc2,Mettl14,Dcp1b,Lin28b, Gm5519
	GO:0019439	Aromatic compound catabolic process	2.48	20/485	Rida,Khk,Ppara,Zfp36,Nt5e,Esrrb,Lsm4,Zbtb20,Exosc3,Nudt16l1, Rnaseh2c,Exosc8,Brf1,Gale,Nudt17,Csdc2,Mettl14,Dcp1b,Lin28b, Gm5519
	GO:0006733	Oxidoreduction coenzyme metabolic process	2.37	10/177	Khk,Ppara,Esrrb,Zbtb20,Rpe,Nmnat3,Gale,Nudt17,Nmrk1,Coq4
	GO:0006401	RNA catabolic process	2.32	12/239	Rida,Zfp36,Lsm4,Exosc3,Nudt16l1,Rnaseh2c,Exosc8,Brf1,Csdc2, Mettl14,Dcp1b,Lin28b
6	GO:0008356	Asymmetric cell division	3.07	4/21	Sox5,Tead3,Etv5,Insc
	GO:0098722	Asymmetric stem cell division	2.88	3/11	Sox5,Tead3,Etv5
	GO:0017145	Stem cell division	2.38	5/51	Fzd7,Sox5,Tead3,Esrrb,Etv5
7	GO:0009650	UV protection	3.01	3/10	Cat,Ercc3,Mfap4
8	GO:0060346	Bone trabecula formation	2.88	3/11	Col1a1,Thbs3,Grem1
	GO:0060343	Trabecula formation	2.64	4/27	Col1a1,Tgfbr3,Thbs3,Grem1
	GO:0061430	Bone trabecula morphogenesis	2.46	3/15	Col1a1,Thbs3,Grem1
9	GO:0050678	Regulation of epithelial cell proliferation	2.81	17/358	Cdh1,Cdkn2b,Egr3,Erbb4,Fzd7,Hes5,Rida,Nkx3-1,Scn5a,Tgfbr3, Ift88,Zfp36,Srsf6,Pbld1,Marveld3,Esrp2,Iqgap3
	GO:0050673	Epithelial cell proliferation	2.39	18/426	Cdh1,Cdkn2b,Egr3,Erbb4,Fzd7,Hes5,Rida,Nkx3-1,Scn5a,Tgfbr3, Ift88,Zfp36,Ncstn,Srsf6,Pbld1,Marveld3,Esrp2,Iqgap3
10	GO:0035051	Cardiocyte differentiation	2.75	11/184	Parp2,Folr1,Fzd7,Hdac3,Sik1,Pdgfrb,Ppara,Tgfbr3,Ift88,Grem1, Pbrm1
	GO:2000725	Regulation of cardiac muscle cell differentiation	2.49	5/48	Parp2,Fzd7,Hdac3,Ppara,Grem1
11	GO:0048505	Regulation of timing of cell differentiation	2.55	3/14	Hes5,Sox5,Nr2e1
	GO:0040034	Regulation of development, heterochronic	2.38	3/16	Hes5,Sox5,Nr2e1
12	mmu04974	Protein digestion and absorption	2.55	7/90	Col4a5,Col6a2,Col1a1,Eln,Slc1a1,Slc7a8,Slc15a1
13	GO:0045292	mRNA cis splicing, via spliceosome	2.52	4/29	Srsf2,Srsf6,Srsf7,Gm12355
	R-MMU-159236	Transport of Mature mRNA derived from an Intron-Containing Transcript	2.46	6/70	Ranbp2,Srsf2,Thoc7,Srsf6,Srsf7,Gm8994
14	GO:0032370	**Positive regulation of lipid transport**	2.49	6/69	Commd1,Nkx3-1,Sstr4,Pla2g10,Abca7,Cyp4f18
	GO:0032305	Positive regulation of icosanoid secretion	2.30	3/17	Sstr4,Pla2g10,Cyp4f18
15	R-MMU-180024	DARPP-32 events	2.46	3/15	Prkar2b,Ppp2r1b,Pde4c
16	R-MMU-450513	Tristetraprolin (TTP, ZFP36) binds and destabilizes mRNA	2.46	3/15	Zfp36,Exosc3,Exosc8
	GO:0034661	ncRNA catabolic process	2.32	4/33	Exosc3,Nudt16l1,Exosc8,Lin28b
17	GO:0015669	Gas transport	2.46	3/15	Aqp1,Car2,Ngb
18	GO:0000079	Regulation of cyclin-dependent protein serine/threonine kinase activity	2.40	6/72	Ccng2,Ccni,Cdkn2b,Pkd2,Cdc6,Psmd10
19	GO:0099638	**Endosome to plasma membrane protein transport**	2.38	3/16	Commd1,Trarg1,Lrrc7
20	GO:0006359	Regulation of transcription by RNA polymerase III	2.38	3/16	Ell,Maf1,Brf1

GO and KEGG terms in Reactome knowledgebase (https://reactome.org/) enriched in the differentially expressed genes in prion-infected ThN at 21 dpi (-LogP > 2.3, equivalent to p < 0.005). The enriched terms were hierarchically clustered based on their gene memberships by Metascape (http://metascape.org), and representative terms in each cluster are listed with accession numbers, brief descriptions, and the numbers and names of genes in a data list of the differentially expressed genes used for the analysis.

II-iii. Prediction of influence of prion infection on biological pathways and functions.

The GO analysis revealed that alterations in gene expression induced neuron-autonomously by PrP^{Sc} production were involved in several biological functions including immune processes, neurofunctions, the lipid metabolism and the protein translocation to the membrane. To interpret and/or speculate influences of prion-induced differentially expressed genes on biological functions in neurons, I used the Ingenuity Pathway Analysis (IPA). The IPA can identify canonical pathways and biological functions & diseases that are most relevant to the gene set, which is similar to the GO enrichment analysis though IPA uses its original terms (canonical pathways and diseases & functions) in the IPA knowledgebase. In addition to such an enrichment analysis, IPA predicts activation states of the pathways and the functions by computing the activation z-score statistically based on alterations in expressions of the gene set. Basically, positive z-score means predicted activation, whereas negative z-score means predicted inhibition of the pathways and functions.

The IPA analysis using the data set of differentially expressed genes in prion-infected CxNs at 14 dpi ($|FC| \geq 1.25$) showed canonical pathways significantly associated with prion-related changes in the gene expression (Figure II-4-1A). Sumoylation pathway was the only pathway that was predicted to be slightly activated ($z = 1.34$) as the significantly enriched canonical pathways in CxNs at 14 dpi ($p < 0.05$). IPA predicted activation/inhibition of 2 canonical pathways that are related to cytoskeleton organization and neurite outgrowth, RhoGDI signaling ($z = -2.00$) and signaling by Rho family GTPase ($z = 1.34$), although their enrichments were not statistically significant ($p > 0.05$). RhoGDI functions as an inhibitory regulator of Rho family GTPase proteins [172] so that negative regulation of the RhoGDI signaling may also contribute to the activation of the Rho GTPase signaling [173].

The diseases and functions (D&F) analysis tool of the IPA displayed enriched physiological and pathological functions in prion-infected CxNs at 14 dpi (Figure II-4-1B). The

(A)

Ingenuity Canonical Pathways	-logP	z-score
Salvage Pathways of Pyrimidine Deoxyribonucleotides	2.36	
Tight Junction Signaling	1.61	
UVA-Induced MAPK Signaling	1.55	
Sumoylation Pathway	1.55	1.34
Apelin Cardiomyocyte Signaling Pathway	1.55	0.00
Pyrimidine Ribonucleotides Interconversion	1.51	
GPCR-Mediated Integration of Enteroendocrine Signaling exemplified by an L Cell	1.46	
Alanine Degradation III	1.46	
Alanine Biosynthesis II	1.46	
L-cysteine Degradation III	1.46	
GDP-L-fucose Biosynthesis II (from L-fucose)	1.46	
Pyrimidine Ribonucleotides De Novo Biosynthesis	1.45	
Retinoic acid Mediated Apoptosis Signaling	1.38	
D-myo-inositol-5-phosphate Metabolism	1.33	-0.82
FAT10 Cancer Signaling Pathway	1.33	
RhoGDI Signaling	0.72	-2.00
Signaling by Rho Family GTPases	0.63	1.34

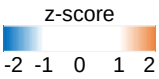

(B)

Diseases or Functions Annotation	-logP	z-score
Cell death of lymphoid organ	2.82	1.01
Loss of hair	2.50	-1.03
Apoptosis of lymphoid organ	2.07	1.59
Apoptosis of thymocytes	1.92	1.36
Hyperplasia of exocrine gland	1.77	-1.07
Eating Disorders	1.77	1.99
Cell death of macrophage cancer cell lines	1.75	1.07
Disorder of hair	1.69	-1.03
Apoptosis of cardiomyocytes	1.67	-1.11
Binding of T lymphocytes	1.61	-1.13
Transport of heavy metal	1.59	-1.02
T cell homeostasis	1.54	1.28
Differentiation of T lymphocytes	1.50	1.50
Conversion of lipid	1.50	1.09

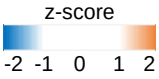

Figure II-4-1. Biological characterization of genes differentially expressed (|FC| ≥ 1.25) in prion-infected CxN at 14 dpi.

(A) Top canonical pathways determined by IPA using genes differentially expressed with |FC| ≥ 1.25 in prion-infected CxN at 14 dpi. All the pathways that have p values less than 0.05 (-logP > 1.3) in enrichment analysis are listed above the broken line. In addition, pathways which absolute values of the activated z-score are above 1.3 with –logP ≤ 1.3 (p > 0.05) are added to the bottom of the list. The activation z-score is a statistical quantity computed by IPA to infer activation states of biological functions. Positive z-score (orange) means predicted activation of the pathway, whereas negative z-score (blue) means predicted inhibition/repression of the pathway. Blanks in the column of z-score indicate that z-score for these pathways were not able to be culculatged from the data set. (B) Diseases and functions (-logP > 1.3 and |z| ≥ 1.0) determined by IPA using genes differentially expressed in prion-infected CxN at 14 dpi. The z-scores and color intensities indicate the same prediction as described in (A).

enriched D&F annotations were similar to the enriched biological process GO terms (Table II-2-1). In relation to "lymphocyte apoptotic process" (GO:0070227), IPA predicted a trend toward activation of several D&F related to cell death and homeostasis of lymphoid tissues and cells such as "apoptosis of lymphoid organ" (z = 1.59), "apoptosis of thymocytes" (z = 1.36) and "differentiation of T lymphocytes" (z = 1.50) (Figure II-4-1B). The D&F analysis also predicted activation of "eating disorders" with largest absolute value of z-score (z = 1.99), which seemed to be related to the enriched GO term "regulation of behavior". The activation of "eating disorders" is of interest since Obihiro-infected ICR mice show temporary gaining body weight just before the onset of ataxia (unpublished data).

At 21dpi, IPA canonical pathway analysis showed enrichment of the differentially expressed genes ($|FC| \geq 1.25$) in the pathways related to F-actin formation, cytoskeletal reorganization, and axon guidance (Figure II-4-2A). Of those enriched canonical pathways, IPA predicted activation of G beta gamma signaling (z = 1.89) which regulates cellular functions such as endocytosis, cell survival and neuronal signaling starting from stimulation of G protein-coupled receptors (GPCRs). Several GPCR-downstream pathways such as PI3K signaling (z = 1.34), GCPR-mediated nutrient sensing in enteroendocrine cells (z = 0.82), and Cdc42 signaling (z = -2.00, however, the enrichment was not significant), were also included in the output of the canonical pathway analysis. These signaling pathways are associated with cytoskeletal reorganization and the neurite outgrowth [174, 175]. Activation of synaptic long-term depression pathway (z = 1.41) was also predicted in prion-infected CxNs at 21 dpi. The D&F analysis showed predicted activation of proliferation of immune cells (z = 1.54) simultaneously as cell death of T lymphocytes (z = 1.63), and injury of cells (z = 2.00) (Figure II-4-2B).

As for ThNs at 14 dpi, IPA showed enrichment of the differentially expressed genes ($|FC| \geq 1.25$) in those regulating a canonical pathway named fatty acid activation (z = 1.37), which may be associated with the result of the GO enrichment analysis that showed enrichment in

(A)

Ingenuity Canonical Pathways	-logP	z-score
Virus Entry via Endocytic Pathways	2.55	
Acetate Conversion to Acetyl-CoA	2.49	
Ephrin A Signaling	2.36	
NAD Biosynthesis from 2-amino-3-carboxymuconate semialdehyde	2.28	
Caveolar-mediated Endocytosis Signaling	2.19	
G Beta Gamma Signaling	2.13	1.89
FcγRIIB Signaling in B Lymphocytes	2.08	
CTLA4 Signaling in Cytotoxic T Lymphocytes	1.92	
nNOS Signaling in Skeletal Muscle Cells	1.85	
Netrin Signaling	1.76	1.34
Cell Cycle: G1/S Checkpoint Regulation	1.76	2.00
Role of Tissue Factor in Cancer	1.76	
Molecular Mechanisms of Cancer	1.74	
Prostanoid Biosynthesis	1.66	
PD-1, PD-L1 cancer immunotherapy pathway	1.65	0.00
Integrin Signaling	1.64	-0.38
NAD biosynthesis II (from tryptophan)	1.58	
Actin Cytoskeleton Signaling	1.58	0.33
Role of NFAT in Cardiac Hypertrophy	1.58	0.33
Synaptic Long-Term Depression	1.53	1.41
Cytotoxic T Lymphocyte-mediated Apoptosis of Target cells	1.52	
p70S6K Signaling	1.51	0.00
Endocannabinoid Neuronal Synapse Pathway	1.51	0.38
Macropinocytosis Signaling	1.50	
Germ Cell-Sertoli Cell Junction Signaling	1.42	
Calcium Signaling	1.38	1.00
PI3K Signaling in B Lymphocytes	1.38	1.34
Glioma Signaling	1.36	
HER-2 Signaling in Breast Cancer	1.36	
GPCR-Mediated Nutrient Sensing in Enteroendocrine Cells	1.34	0.82
Dolichol and Dolichyl Phosphate Biosynthesis	1.33	
Granzyme B Signaling	1.32	
Autophagy	1.32	
Opioid Signaling Pathway	1.25	1.67
Glioblastoma Multiforme Signaling	1.05	-1.34
Role of NFAT in Regulation of the Immune Response	0.96	1.34
Sphingosine-1-phosphate Signaling	0.92	-1.34
D-myo-inositol-5-phosphate Metabolism	0.86	1.63
Cdc42 Signaling	0.67	-2.00
3-phosphoinositide Degradation	0.58	2.24
Senescence Pathway	0.57	-1.63
3-phosphoinositide Biosynthesis	0.51	1.34
D-myo-inositol (1,4,5,6)-Tetrakisphosphate Biosynthesis	0.42	2.00
D-myo-inositol (3,4,5,6)-tetrakisphosphate Biosynthesis	0.42	2.00

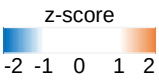

(B)

Diseases or Functions Annotation	-logP	z-score
Reperfusion injury	2.41	2.16
Thrombus	2.12	-1.40
Inflammation of muscle	1.92	1.11
Activation of T lymphocytes	1.88	1.18
Proliferation of immune cells	1.88	1.54
Apoptosis of T lymphocytes	1.80	1.38
Cell death of T lymphocytes	1.80	1.63
Pericardial effusion	1.78	-1.13
Proliferation of lymphocytes	1.75	1.39
Injury of cells	1.74	2.00
Development of body trunk	1.73	1.46
Metabolism of hormone	1.72	-1.39
Quantity of metal ion	1.59	-1.45
Activation of lymphocytes	1.54	1.43
Differentiation of B lymphocytes	1.50	1.95
Development of body axis	1.44	-1.34
Inflammation of airway	1.44	1.07
Quantity of islet cells	1.44	-1.17
Proliferation of progenitor cells	1.42	-1.43
Development of head	1.39	-1.34
Differentiation of T lymphocytes	1.37	-1.05
Synthesis of hormone	1.36	-1.39

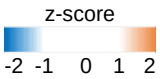

Figure II-4-2. Biological characterization of genes differentially expressed (|FC| ≥ 1.25) in prion-infected CxN at 21 dpi.

(A) Top canonical pathways determined by IPA using genes differentially expressed with |FC| ≥ 1.25 in prion-infected CxN at 21 dpi. All the pathways that have p values less than 0.05 (-logP > 1.3) in enrichment analysis are listed above the broken line. In addition, pathways which absolute values of the activated z-score are above 1.3 with –logP ≤ 1.3 (p > 0.05) are added to the bottom of the list. (B) Diseases and functions (-logP > 1.3 and |z| ≥ 1.0) determined by IPA using genes differentially expressed in prion-infected CxN at 21 dpi.

lipid metabolism-related GO terms (Table II-2-3 & 2-4). Although the canonical pathway analysis suggested that there was no enriched pathway predicted to be activated or inhibited in prion-infected ThN at 14 dpi (Figure II-4-3A), the D&F analysis using the data set of ThNs at 14 dpi predicted activation of proliferation of central nervous system cells (z = 2.40) and cognitive impairment (z = 2.21) (Figure II-4-3B). Differentially expressed genes involved in regulation of the proliferation of central nervous system cells were *App* (FC = 1.19), *Ctf2* (FC = 25.93), *Kif26a* (FC = −1.20), *Kras* (FC = 1.36), *Ncor2* (FC = 1.31), *Neto*2 (FC = 1.14), *Nr1h2* (FC = −1.44), *Wnt7*a (FC = 1.96). Genes included the data set that had regulatory influence on the predicted activation of the cognitive impairment were *Ace, App, Dlg3, Fxr2, Ip6k3, Kcnj11, Lcmt1, Pcp4, Ppme1, Ptpra, Ptprf, Rtl4, and Trpm2*. IPA did not predict activation of pathways or functions related to the synthesis of GPI-anchored proteins, which was suggested by the GO enrichment analysis (Table II-2-3).

Canonical pathways predicted activation of nucleotide excision repair (NER) pathway (z = 2.33) which is usually induced by DNA damage caused by UV radiation or DNA-reactive chemical compounds, in prion-infected ThNs at 21dpi. Although the enrichment was not significant, several pathways related to lipid metabolism, neuronal functions, and cytoskeletal organization might be associated with possible prion-induced neuronal damages were predicted to be activated; PPARα/RXRα activation pathway (z = 2.83) might be related to the regulation of lipid homeostasis, the pigment epithelium derived factor (PEDF) signaling (z = −2.00) which promotes survival of neurons by inducing anti-apoptotic and neurotrophic factors. The D&F analysis predicted activation of proliferation of neural stem cells (z = 1.68) and pluripotency of cells (z = 1.95), suggesting the proliferation of immature neural cells in the prion-infected ThNs. In addition, it is of interest that brain function-related D&F, cognition (z = −1.11) and contextual conditioning (z = −1.70), tended to be repressed (Figure II-4-4).

(A)

Ingenuity Canonical Pathways	-logP	z-score
Acetyl-CoA Biosynthesis III (from Citrate)	1.59	
Sorbitol Degradation I	1.59	
Fatty Acid Activation	1.37	
Agrin Interactions at Neuromuscular Junction	1.36	1.00
Gα12/13 Signaling	1.34	0.38
Dolichol and Dolichyl Phosphate Biosynthesis	1.30	
GDP-L-fucose Biosynthesis I (from GDP-D-mannose)	1.30	
NRF2-mediated Oxidative Stress Response	1.04	2.00
JAK/Stat Signaling	0.82	2.00
VEGF Family Ligand-Receptor Interactions	0.80	2.00
Renin-Angiotensin Signaling	0.75	2.00
Ceramide Signaling	0.75	2.00
PDGF Signaling	0.75	2.00
p70S6K Signaling	0.64	2.00
NER Pathway	0.59	-2.00
NF-κB Signaling	0.56	2.45
CDK5 Signaling	0.55	2.00
Rac Signaling	0.51	2.00
Fc Epsilon RI Signaling	0.48	2.00
Superpathway of Inositol Phosphate Compounds	0.45	1.63
Synaptogenesis Signaling Pathway	0.44	1.67
14-3-3-mediated Signaling	0.40	2.00
P2Y Purigenic Receptor Signaling Pathway	0.40	2.00
Glioblastoma Multiforme Signaling	0.40	2.24
Phospholipase C Signaling	0.39	1.63
Acute Phase Response Signaling	0.37	2.24
Cardiac Hypertrophy Signaling (Enhanced)	0.37	2.31
Colorectal Cancer Metastasis Signaling	0.35	1.89
D-myo-inositol (1,4,5,6)-Tetrakisphosphate Biosynthesis	0.35	2.00
D-myo-inositol (3,4,5,6)-tetrakisphosphate Biosynthesis	0.35	2.00
3-phosphoinositide Degradation	0.28	2.00
PKCθ Signaling in T Lymphocytes	0.28	2.00
D-myo-inositol-5-phosphate Metabolism	0.28	2.00
Synaptic Long-Term Depression	0.00	2.00
IL-8 Signaling	0.00	2.00
Cardiac Hypertrophy Signaling	0.00	2.24
GNRH Signaling	0.00	2.00
CREB Signaling in Neurons	0.00	2.00
Role of NFAT in Cardiac Hypertrophy	0.00	2.24
Adrenomedullin signaling pathway	0.00	2.00
Hepatic Fibrosis Signaling Pathway	0.00	1.67

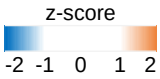

(B)

Diseases or Functions Annotation	-logP	z-score
Glycolysis of cells	2.35	1.41
Activation of microglia	2.10	1.18
Expansion of lymphoid organ	1.88	1.12
Quantity of double-negative T lymphocyte	1.85	-2.22
Proliferation of central nervous system cells	1.67	2.40
Quantity of kidney	1.59	-2.16
Cognitive impairment	1.48	2.21
Release of metal	1.47	1.11
Quantity of epithelial cells	1.34	1.09
Quantity of nephron	1.31	-1.98

Figure II-4-3. Biological characterization of genes differentially expressed (|FC| ≥ 1.25) in prion-infected ThN at 14 dpi.

(A) Top canonical pathways determined by IPA using genes differentially expressed with |FC| ≥ 1.25 in prion-infected ThN at 14 dpi. All the pathways that have p values less than 0.05 (-logP > 1.3) in enrichment analysis are listed above the broken line. In addition, pathways which absolute values of the activated z-score are above 1.3 with –logP ≤ 1.3 (p > 0.05) are added to the bottom of the list. (B) Diseases and functions (-logP > 1.3 and |z| ≥ 1.0) determined by IPA using genes differentially expressed in prion-infected ThN at 14 dpi.

(A)

Ingenuity Canonical Pathways	-logP	z-score
DNA Methylation and Transcriptional Repression Signaling	3.49	
Cell Cycle: G1/S Checkpoint Regulation	2.42	-0.45
Oxidized GTP and dGTP Detoxification	2.33	
Remodeling of Epithelial Adherens Junctions	1.87	
NAD Salvage Pathway III	1.83	
Wnt/β-catenin Signaling	1.76	0.30
NER Pathway	1.74	2.33
tRNA Splicing	1.64	-0.45
Triacylglycerol Degradation	1.56	1.34
Thioredoxin Pathway	1.53	
Lipoate Salvage and Modification	1.40	
UDP-N-acetyl-D-galactosamine Biosynthesis I	1.40	
CTLA4 Signaling in Cytotoxic T Lymphocytes	1.37	
OX40 Signaling Pathway	1.35	
UDP-N-acetyl-D-galactosamine Biosynthesis II	1.32	
PPARα/RXRα Activation	0.53	2.83
PEDF Signaling	0.39	-2.00
CDK5 Signaling	0.39	2.24
Dendritic Cell Maturation	0.35	-1.89
Sirtuin Signaling Pathway	0.30	1.67
LPS/IL-1 Mediated Inhibition of RXR Function	0.00	-2.00
Role of NFAT in Regulation of the Immune Response	0.00	-2.45
Endocannabinoid Neuronal Synapse Pathway	0.00	-2.00
Synaptogenesis Signaling Pathway	0.00	1.67
White Adipose Tissue Browning Pathway	0.00	2.24
Hepatic Fibrosis Signaling Pathway	0.00	-1.67

z-score
-2 -1 0 1 2

(B)

Diseases or Functions Annotation	-logP	z-score
Uptake of Ca2+	2.44	2.19
Proliferation of neural stem cells	2.38	1.68
Binding of glycosaminoglycan	2.22	-1.17
Pluripotency of cells	2.06	1.95
Weight loss	1.75	-2.78
Cognition	1.69	-1.11
Death of embryo	1.67	-2.01
Proliferation of CD4+ T-lymphocytes	1.55	1.09
Oxidative stress	1.55	1.12
Contextual conditioning	1.54	-1.70
Transport of heavy metal	1.49	1.28
Lymphoma	1.44	1.24
Entry into cell cycle progression	1.43	-1.98

z-score
-2 -1 0 1 2

Figure II-4-4. Biological characterization of genes differentially expressed (|FC| ≥ 1.25) in prion-infected ThN at 21 dpi.

(A) Top canonical pathways determined by Ingenuity Pathway Analysis (IPA, QIAGEN) using genes differentially expressed with |FC| ≥ 1.25 in prion-infected ThN at 21 dpi. All the pathways that have p values less than 0.05 (-logP > 1.3) in enrichment analysis are listed above the broken line. In addition, pathways which absolute values of the activated z-score are above 1.3 with –logP ≤ 1.3 (p > 0.05) are added to the bottom of the list. (B) Diseases and functions (-logP > 1.3 and |z| ≥ 1.0) determined by IPA using genes differentially expressed in prion-infected ThN at 21 dpi.

In this study, I identified 108 genes that may reflect primary, and autonomous responses of neurons to the generation of PrP^{Sc}. Bioinformatic analyses using GO and IPA did not suggest any canonical pathways or biological functions that are directly related to the neuronal cell death and neurodegeneration. However, transcriptome analyses suggest further research targets on neuron-autonomous changes by prion propagation, such as cellular functions related to the lipid metabolism and transport, and reorganization of cytoskeleton.

SUMMARY

Identification of cell biological processes/functions that are affected by prion propagation in neurons will facilitate to clarify the neuropathogenesis of prion diseases. To gain insight into the autonomous neuronal responses to prion propagation, I analyzed transcriptome of CxNs and ThNs cultures infected with prions. Over 2,000 differentially expressed genes were identified by comparison of gene expression profiles between mock- and prion-infected CxNs or ThNs at 14 and 21 dpi. A total of 108 differentially expressed genes were found in common across 2 or 3 experimental conditions based on neuronal type and days after inoculation. Of the 108 genes, 4 genes were previously reported as differentially expressed genes in prion disease, and 13 genes were associated with other neurodegenerative disorders accompanied by protein misfolding such as AD. Upregulation of *Ncstn* in prion-infected ThNs at both 14 and 21 dpi suggests the presence of neuron-autonomous response to prion propagation, which is also suggested to be involved in the development of AD. Bioinformatic analyses of differentially expressed genes using GO and IPA analyses did not suggest any canonical pathways or biological functions that are directly related to the neuronal cell death and neurodegeneration. This interpretation implies that prion propagation in neurons would not totally activate neuron-autonomous processes that lead to neuronal death, which is consistent with the findings in the Chapter I. However, interestingly, IPA analysis suggested that alterations of some biological processes in prion-infected CxNs and ThNs, which are associated with cytoskeleton reorganization and lipid metabolism. Although obvious alterations in cell biological process were not suggested from the transcriptome of prion-infected neurons, information on comprehensive gene expression profiles of prion-infected neurons will be useful for understanding the mechanisms of neurodegeneration in prion diseases.

CONCLUSION

Conversion of PrP^{C} into PrP^{Sc} in neurons is one of the key pathophysiological events in prion diseases. A line of evidence indicates that microglia and astrocytes play important roles in the neuropathogenesis of prion diseases as non-autonomous neuronal cell death. Prion propagation in neurons itself is also believed to be a key event in the neuropathogenesis of prion diseases; however, genuine neuronal responses to prion propagation have yet to be fully elucidated because of a lack of suitable experimental models for analyzing neuron-autonomous responses to prion infection. To analyze neuron-autonomous events specifically, I optimized a neuron-enrichment protocol which was able to control astrocytic growth in cortical and thalamic neuronal cultures over a month. These primary neurons were susceptible to prion infection and the characteristics of PrP^{Sc} produced in the primary neurons resembled those observed in brains of prion-infected mice. Therefore, in my thesis, I extensively studied neuron-autonomous events to prion infection using the primary neuronal cultures infected with prions.

In Chapter I, autonomous neuronal responses to prion infection was analyzed using neuron-enriched primary cultures of mouse neurons. PrP^{Sc} levels in neurons increased over the time after prion infection; however, no obvious neuronal losses or neurite alterations were observed. Interestingly, a finer analysis of individual neurons co-stained with PrP^{Sc} and p-PERK, the early cellular response of the PERK-eIF2α pathway, demonstrated a positive correlation between the number of PrP^{Sc} granular stains and p-PERK granular stains, in cortical neurons at 21 dpi. Although the phosphorylation of PERK was enhanced in prion-infected cortical neurons, there was no sign of subsequent translational repression of synaptic protein synthesis or activations of downstream UPR in the PERK-eIF2α pathway. These results suggest that PrP^{Sc} production in neurons induces ER stress in a neuron-autonomous manner; however, it does not fully activate UPR in prion-infected neurons.

In Chapter II, I analyzed transcriptome of neuron-enriched primary CxNs and ThNs

infected with prions in order to gain insight into the autonomous neuronal responses to prion propagation. Bioinformatic analyses of differentially expressed genes using Gene Ontology and the Ingenuity Pathway Analysis (IPA) did not suggest any canonical pathways or biological functions that are directly related to the neuronal cell death and neurodegeneration. This interpretation implies that prion propagation in neurons would not totally activate neuron-autonomous processes that lead to neuronal death, which is consistent with the findings in the Chapter I. However, interestingly, IPA analysis suggested that alterations of some biological processes in prion-infected ThNs, which are associated with cytoskeleton reorganization and lipid metabolism. Although obvious alterations in cell biological process were not suggested from the transcriptome of prion-infected neurons, information on comprehensive gene expression profiles of prion-infected neurons will be useful for understanding the mechanisms of neurodegeneration in prion diseases.

In my doctoral research, I have tackled to the lack of our understanding of the neuron-autonomous mechanism of neurodegeneration in prion diseases. I disclosed that prion propagation itself induced the early event of ER stress in neurons; however, it does not fully activate UPR in prion-infected neurons. Transcriptome analyses could not expect any specific neuronal events that were affected by prion propagation. These facts suggest the presence of additional, non-neuronal factor(s) in the mechanism of neurodegeneration in prion diseases. Although further studies are required for a comprehensive understanding of the mechanisms of neurodegeneration in prion diseases, I believe that this study contributes to elucidation of neuropathogenesis of prion diseases and identification of potential targets for therapeutic intervention in near future.

ACKNOWLEDGMENT

I would like to express my sincere gratitude to my supervisor, Professor HORIUCHI M. (Laboratory of Veterinary Hygiene, Department of Preventive Veterinary Medicine, Division of Veterinary Medicine, Faculty of Veterinary Medicine, Hokkaido University) for providing me this precious opportunity to spend my six-year undergraduate and graduate school life in his laboratory, and his great help with my research activity since I was welcomed here.

I would like to express my deep appreciation to my advisory supervisors, Professor SAWA H. (Division of Molecular Pathobiology, Research Center for Zoonosis Control, Hokkaido University), Professor ATARASHI R. (Division of Microbiology, Department of Infectious Diseases, Faculty of Medicine, University of Miyazaki), and Associate Professor KOBAYASHI A. (Laboratory of Comparative Pathology, Department of Clinical Sciences, Division of Veterinary Medicine, Faculty of Veterinary Medicine, Hokkaido University), for joining my research as referees giving me many pieces of their perceptive comments and kind advice throughout my PhD course.

I truly thank Dr. YAMASAKI T. and Dr. HASEBE R. for their daily discussion, continuous instruction and encouragement. I learned a lot from these my pilot researchers.

I would like to give my heartfelt thanks to Mr. SUZUKI A. and Ms. OHSAWA M. for their specialties having helped me so many times. Also, I am grateful for all members who have helped me in this lab. I give my deepest gratitude of thanks to my family, friends, and who has been at my side all the time. I had a pleasant time during 10-year university life due to their unstinted supports.

Also, I am grateful to Dr. MASUJIN K. for providing the mAb 8D5, to Dr. Roth B. for pAAV-hSyn-EGFP, and to Dr. Gradinaru V. for pUCmini-iCAP-PHP.eB. This work was supported by Grant-in-aid for JSPS Research Fellow Grant Number JP18J12535.

Finally, I would like to express my sorrow and thanks to numbers of mice for dedicating their lives to our greater knowledge of the prion pathogenesis.

REFFERENCES

1. **Colby DW, Prusiner SB**. Prions. *Cold Spring Harb Perspect Biol* 2011;3(1):a006833.
2. **Collins SJ, Lawson VA, Masters CL**. Transmissible spongiform encephalopathies. *Lancet* 2004;363(9402):51-61.
3. **Nathanson N, Wilesmith J, Griot C**. Bovine spongiform encephalopathy (BSE): causes and consequences of a common source epidemic. *Am J Epidemiol* 1997;145(11):959-969.
4. **Williams ES, Miller MW**. Chronic wasting disease in deer and elk in North America. *Rev Sci Tech* 2002;21(2):305-316.
5. **Henderson DM, Denkers ND, Hoover CE, Garbino N, Mathiason CK et al.** Longitudinal Detection of Prion Shedding in Saliva and Urine by Chronic Wasting Disease-Infected Deer by Real-Time Quaking-Induced Conversion. *J Virol* 2015;89(18):9338-9347.
6. **Wang K, Lee I, Carlson G, Hood L, Galas D**. Systems biology and the discovery of diagnostic biomarkers. *Dis Markers* 2010;28(4):199-207.
7. **Pan KM, Baldwin M, Nguyen J, Gasset M, Serban A et al.** Conversion of alpha-helices into beta-sheets features in the formation of the scrapie prion proteins. *Proc Natl Acad Sci U S A* 1993;90(23):10962-10966.
8. **Prusiner SB**. Prions. *Proc Natl Acad Sci U S A* 1998;95(23):13363-13383.
9. **Bueler H, Aguzzi A, Sailer A, Greiner RA, Autenried P et al.** Mice devoid of PrP are resistant to scrapie. *Cell* 1993;73(7):1339-1347.
10. **Prusiner SB, Groth D, Serban A, Koehler R, Foster D et al.** Ablation of the prion protein (PrP) gene in mice prevents scrapie and facilitates production of anti-PrP antibodies. *Proc Natl Acad Sci U S A* 1993;90(22):10608-10612.
11. **Manson JC, Clarke AR, McBride PA, McConnell I, Hope J**. PrP gene dosage determines the timing but not the final intensity or distribution of lesions in scrapie pathology. *Neurodegeneration* 1994;3(4):331-340.
12. **Brandner S, Isenmann S, Raeber A, Fischer M, Sailer A et al.** Normal host prion protein necessary for scrapie-induced neurotoxicity. *Nature* 1996;379(6563):339-343.
13. **Mallucci GR, White MD, Farmer M, Dickinson A, Khatun H et al.** Targeting cellular prion protein reverses early cognitive deficits and neurophysiological dysfunction in prion-infected mice. *Neuron* 2007;53(3):325-335.
14. **Mallucci G, Dickinson A, Linehan J, Klohn PC, Brandner S et al.** Depleting neuronal PrP in prion infection prevents disease and reverses spongiosis. *Science* 2003;302(5646):871-874.
15. **Goold R, Rabbanian S, Sutton L, Andre R, Arora P et al.** Rapid cell-surface prion protein conversion revealed using a novel cell system. *Nat Commun* 2011;2:281.
16. **Naslavsky N, Stein R, Yanai A, Friedlander G, Taraboulos A**. Characterization of detergent-insoluble complexes containing the cellular prion protein and its scrapie isoform. *J Biol Chem* 1997;272(10):6324-6331.
17. **Vey M, Pilkuhn S, Wille H, Nixon R, DeArmond SJ et al.** Subcellular colocalization of the cellular and scrapie prion proteins in caveolae-like membranous domains. *Proc Natl Acad Sci U S A* 1996;93(25):14945-14949.

18. **Borchelt DR, Taraboulos A, Prusiner SB**. Evidence for synthesis of scrapie prion proteins in the endocytic pathway. *J Biol Chem* 1992;267(23):16188-16199.
19. **Taraboulos A, Raeber AJ, Borchelt DR, Serban D, Prusiner SB**. Synthesis and trafficking of prion proteins in cultured cells. *Mol Biol Cell* 1992;3(8):851-863.
20. **Beranger F, Mange A, Goud B, Lehmann S**. Stimulation of PrP(C) retrograde transport toward the endoplasmic reticulum increases accumulation of PrP(Sc) in prion-infected cells. *J Biol Chem* 2002;277(41):38972-38977.
21. **Marijanovic Z, Caputo A, Campana V, Zurzolo C**. Identification of an intracellular site of prion conversion. *PLoS Pathog* 2009;5(5):e1000426.
22. **Pimpinelli F, Lehmann S, Maridonneau-Parini I**. The scrapie prion protein is present in flotillin-1-positive vesicles in central- but not peripheral-derived neuronal cell lines. *Eur J Neurosci* 2005;21(8):2063-2072.
23. **Veith NM, Plattner H, Stuermer CA, Schulz-Schaeffer WJ, Burkle A**. Immunolocalisation of PrPSc in scrapie-infected N2a mouse neuroblastoma cells by light and electron microscopy. *Eur J Cell Biol* 2009;88(1):45-63.
24. **Yamasaki T, Suzuki A, Shimizu T, Watarai M, Hasebe R et al.** Characterization of intracellular localization of PrP(Sc) in prion-infected cells using a mAb that recognizes the region consisting of aa 119-127 of mouse PrP. *The Journal of general virology* 2012;93(Pt 3):668-680.
25. **Yamasaki T, Baron GS, Suzuki A, Hasebe R, Horiuchi M**. Characterization of intracellular dynamics of inoculated PrP-res and newly generated PrP(Sc) during early stage prion infection in Neuro2a cells. *Virology* 2014;450-451:324-335.
26. **Bueler H, Fischer M, Lang Y, Bluethmann H, Lipp HP et al.** Normal development and behaviour of mice lacking the neuronal cell-surface PrP protein. *Nature* 1992;356(6370):577-582.
27. **Manson JC, Clarke AR, Hooper ML, Aitchison L, McConnell I et al.** 129/Ola mice carrying a null mutation in PrP that abolishes mRNA production are developmentally normal. *Mol Neurobiol* 1994;8(2-3):121-127.
28. **Richt JA, Kasinathan P, Hamir AN, Castilla J, Sathiyaseelan T et al.** Production of cattle lacking prion protein. *Nat Biotechnol* 2007;25(1):132-138.
29. **Benestad SL, Austbo L, Tranulis MA, Espenes A, Olsaker I**. Healthy goats naturally devoid of prion protein. *Vet Res* 2012;43:87.
30. **Mallucci GR, Ratte S, Asante EA, Linehan J, Gowland I et al.** Post-natal knockout of prion protein alters hippocampal CA1 properties, but does not result in neurodegeneration. *Embo j* 2002;21(3):202-210.
31. **Chiti Z, Knutsen OM, Betmouni S, Greene JR**. An integrated, temporal study of the behavioural, electrophysiological and neuropathological consequences of murine prion disease. *Neurobiol Dis* 2006;22(2):363-373.
32. **Cunningham C, Deacon R, Wells H, Boche D, Waters S et al.** Synaptic changes characterize early behavioural signs in the ME7 model of murine prion disease. *Eur J Neurosci* 2003;17(10):2147-2155.
33. **Fang C, Wu B, Le NTT, Imberdis T, Mercer RCC et al.** Prions activate a p38 MAPK synaptotoxic signaling pathway. *PLoS Pathog* 2018;14(9):e1007283.

34. **Foliaki ST, Lewis V, Finkelstein DI, Lawson V, Coleman HA et al.** Prion acute synaptotoxicity is largely driven by protease-resistant PrPSc species. *PLoS Pathog* 2018;14(8):e1007214.
35. **Hynd MR, Scott HL, Dodd PR**. Glutamate-mediated excitotoxicity and neurodegeneration in Alzheimer's disease. *Neurochem Int* 2004;45(5):583-595.
36. **Ambrosi G, Cerri S, Blandini F**. A further update on the role of excitotoxicity in the pathogenesis of Parkinson's disease. *J Neural Transm (Vienna)* 2014;121(8):849-859.
37. **Williams A, Lucassen PJ, Ritchie D, Bruce M**. PrP deposition, microglial activation, and neuronal apoptosis in murine scrapie. *Exp Neurol* 1997;144(2):433-438.
38. **Giese A, Groschup MH, Hess B, Kretzschmar HA**. Neuronal cell death in scrapie-infected mice is due to apoptosis. *Brain Pathol* 1995;5(3):213-221.
39. **Jesionek-Kupnicka D, Buczynski J, Kordek R, Sobow T, Kloszewska I et al.** Programmed cell death (apoptosis) in Alzheimer's disease and Creutzfeldt-Jakob disease. *Folia Neuropathol* 1997;35(4):233-235.
40. **Lucassen PJ, Williams A, Chung WC, Fraser H**. Detection of apoptosis in murine scrapie. *Neurosci Lett* 1995;198(3):185-188.
41. **Fairbairn DW, Carnahan KG, Thwaits RN, Grigsby RV, Holyoak GR et al.** Detection of apoptosis induced DNA cleavage in scrapie-infected sheep brain. *FEMS Microbiol Lett* 1994;115(2-3):341-346.
42. **Coulpier M, Messiaen S, Hamel R, Fernandez de Marco M, Lilin T et al.** Bax deletion does not protect neurons from BSE-induced death. *Neurobiol Dis* 2006;23(3):603-611.
43. **Steele AD, Hetz C, Yi CH, Jackson WS, Borkowski AW et al.** Prion pathogenesis is independent of caspase-12. *Prion* 2007;1(4):243-247.
44. **Steele AD, King OD, Jackson WS, Hetz CA, Borkowski AW et al.** Diminishing apoptosis by deletion of Bax or overexpression of Bcl-2 does not protect against infectious prion toxicity in vivo. *J Neurosci* 2007;27(47):13022-13027.
45. **Chiesa R, Piccardo P, Dossena S, Nowoslawski L, Roth KA et al.** Bax deletion prevents neuronal loss but not neurological symptoms in a transgenic model of inherited prion disease. *Proc Natl Acad Sci U S A* 2005;102(1):238-243.
46. **Glick D, Barth S, Macleod KF**. Autophagy: cellular and molecular mechanisms. *J Pathol* 2010;221(1):3-12.
47. **Boellaard JW, Schlote W, Tateishi J**. Neuronal autophagy in experimental Creutzfeldt-Jakob's disease. *Acta Neuropathol* 1989;78(4):410-418.
48. **Liberski PP, Yanagihara R, Wells GA, Gibbs CJ, Jr., Gajdusek DC**. Ultrastructural pathology of axons and myelin in experimental scrapie in hamsters and bovine spongiform encephalopathy in cattle and a comparison with the panencephalopathic type of Creutzfeldt-Jakob disease. *J Comp Pathol* 1992;106(4):383-398.
49. **Sikorska B, Liberski PP, Giraud P, Kopp N, Brown P**. Autophagy is a part of ultrastructural synaptic pathology in Creutzfeldt-Jakob disease: a brain biopsy study. *Int J Biochem Cell Biol* 2004;36(12):2563-2573.
50. **Aguib Y, Heiseke A, Gilch S, Riemer C, Baier M et al.** Autophagy induction by trehalose counteracts

cellular prion infection. *Autophagy* 2009;5(3):361-369.

51. **Heiseke A, Aguib Y, Riemer C, Baier M, Schatzl HM**. Lithium induces clearance of protease resistant prion protein in prion-infected cells by induction of autophagy. *J Neurochem* 2009;109(1):25-34.
52. **Cortes CJ, Qin K, Cook J, Solanki A, Mastrianni JA**. Rapamycin delays disease onset and prevents PrP plaque deposition in a mouse model of Gerstmann-Straussler-Scheinker disease. *J Neurosci* 2012;32(36):12396-12405.
53. **Ron D, Walter P**. Signal integration in the endoplasmic reticulum unfolded protein response. *Nat Rev Mol Cell Biol* 2007;8(7):519-529.
54. **Harding HP, Zhang Y, Ron D**. Protein translation and folding are coupled by an endoplasmic-reticulum-resident kinase. *Nature* 1999;397(6716):271-274.
55. **Kimball SR**. Eukaryotic initiation factor eIF2. *Int J Biochem Cell Biol* 1999;31(1):25-29.
56. **Jackson RJ, Hellen CU, Pestova TV**. The mechanism of eukaryotic translation initiation and principles of its regulation. *Nat Rev Mol Cell Biol* 2010;11(2):113-127.
57. **Han J, Back SH, Hur J, Lin YH, Gildersleeve R et al.** ER-stress-induced transcriptional regulation increases protein synthesis leading to cell death. *Nat Cell Biol* 2013;15(5):481-490.
58. **Galehdar Z, Swan P, Fuerth B, Callaghan SM, Park DS et al.** Neuronal apoptosis induced by endoplasmic reticulum stress is regulated by ATF4-CHOP-mediated induction of the Bcl-2 homology 3-only member PUMA. *J Neurosci* 2010;30(50):16938-16948.
59. **Hetz C, Russelakis-Carneiro M, Maundrell K, Castilla J, Soto C**. Caspase-12 and endoplasmic reticulum stress mediate neurotoxicity of pathological prion protein. *Embo j* 2003;22(20):5435-5445.
60. **Yoo BC, Krapfenbauer K, Cairns N, Belay G, Bajo M et al.** Overexpressed protein disulfide isomerase in brains of patients with sporadic Creutzfeldt-Jakob disease. *Neurosci Lett* 2002;334(3):196-200.
61. **Hetz C, Russelakis-Carneiro M, Walchli S, Carboni S, Vial-Knecht E et al.** The disulfide isomerase Grp58 is a protective factor against prion neurotoxicity. *J Neurosci* 2005;25(11):2793-2802.
62. **Moreno JA, Radford H, Peretti D, Steinert JR, Verity N et al.** Sustained translational repression by eIF2alpha-P mediates prion neurodegeneration. *Nature* 2012;485(7399):507-511.
63. **Moreno JA, Halliday M, Molloy C, Radford H, Verity N et al.** Oral treatment targeting the unfolded protein response prevents neurodegeneration and clinical disease in prion-infected mice. *Sci Transl Med* 2013;5(206):206ra138.
64. **Falsig J, Julius C, Margalith I, Schwarz P, Heppner FL et al.** A versatile prion replication assay in organotypic brain slices. *Nat Neurosci* 2008;11(1):109-117.
65. **Hollister JR, Lee KS, Dorward DW, Baron GS**. Efficient uptake and dissemination of scrapie prion protein by astrocytes and fibroblasts from adult hamster brain. *PLoS One* 2015;10(1):e0115351.
66. **Krejciova Z, Alibhai J, Zhao C, Krencik R, Rzechorzek NM et al.** Human stem cell-derived astrocytes replicate human prions in a PRNP genotype-dependent manner. *J Exp Med* 2017;214(12):3481-3495.
67. **Victoria GS, Arkhipenko A, Zhu S, Syan S, Zurzolo C**. Astrocyte-to-neuron intercellular prion transfer is mediated by cell-cell contact. *Sci Rep* 2016;6:20762.
68. **Cronier S, Carimalo J, Schaeffer B, Jaumain E, Beringue V et al.** Endogenous prion protein conversion

is required for prion-induced neuritic alterations and neuronal death. *Faseb j* 2012;26(9):3854-3861.

69. **Sakai K, Hasebe R, Takahashi Y, Song CH, Suzuki A et al.** Absence of CD14 delays progression of prion diseases accompanied by increased microglial activation. *J Virol* 2013;87(24):13433-13445.
70. **Hasebe R, Tanaka M, Suzuki A, Yamasaki T, Horiuchi M**. Complement factors alter the amount of PrP(Sc) in primary-cultured mouse cortical neurons associated with increased membrane permeability. *Virology* 2016;496:9-20.
71. **Carroll JA, Race B, Williams K, Striebel J, Chesebro B**. Microglia Are Critical in Host Defense against Prion Disease. *J Virol* 2018;92(15).
72. **Gomez-Nicola D, Fransen NL, Suzzi S, Perry VH**. Regulation of microglial proliferation during chronic neurodegeneration. *J Neurosci* 2013;33(6):2481-2493.
73. **Nakagaki T, Satoh K, Ishibashi D, Fuse T, Sano K et al.** FK506 reduces abnormal prion protein through the activation of autolysosomal degradation and prolongs survival in prion-infected mice. *Autophagy* 2013;9(9):1386-1394.
74. **Zhu C, Herrmann US, Falsig J, Abakumova I, Nuvolone M et al.** A neuroprotective role for microglia in prion diseases. *J Exp Med* 2016;213(6):1047-1059.
75. **Rubenstein R, Scalici CL, Papini MC, Callahan SM, Carp RI**. Further characterization of scrapie replication in PC12 cells. *J Gen Virol* 1990;71 (Pt 4):825-831.
76. **Butler DA, Scott MR, Bockman JM, Borchelt DR, Taraboulos A et al.** Scrapie-infected murine neuroblastoma cells produce protease-resistant prion proteins. *J Virol* 1988;62(5):1558-1564.
77. **Race RE, Caughey B, Graham K, Ernst D, Chesebro B**. Analyses of frequency of infection, specific infectivity, and prion protein biosynthesis in scrapie-infected neuroblastoma cell clones. *J Virol* 1988;62(8):2845-2849.
78. **Uryu M, Karino A, Kamihara Y, Horiuchi M**. Characterization of prion susceptibility in Neuro2a mouse neuroblastoma cell subclones. *Microbiol Immunol* 2007;51(7):661-669.
79. **Vilette D**. Cell models of prion infection. *Vet Res* 2008;39(4):10.
80. **Schatzl HM, Laszlo L, Holtzman DM, Tatzelt J, DeArmond SJ et al.** A hypothalamic neuronal cell line persistently infected with scrapie prions exhibits apoptosis. *J Virol* 1997;71(11):8821-8831.
81. **Hannaoui S, Maatouk L, Privat N, Levavasseur E, Faucheux BA et al.** Prion propagation and toxicity occur in vitro with two-phase kinetics specific to strain and neuronal type. *J Virol* 2013;87(5):2535-2548.
82. **Cronier S, Laude H, Peyrin JM**. Prions can infect primary cultured neurons and astrocytes and promote neuronal cell death. *Proc Natl Acad Sci U S A* 2004;101(33):12271-12276.
83. **Alleaume-Butaux A, Nicot S, Pietri M, Baudry A, Dakowski C et al.** Double-Edge Sword of Sustained ROCK Activation in Prion Diseases through Neuritogenesis Defects and Prion Accumulation. *PLoS Pathog* 2015;11(8):e1005073.
84. **Tanaka M, Fujiwara A, Suzuki A, Yamasaki T, Hasebe R et al.** Comparison of abnormal isoform of prion protein in prion-infected cell lines and primary-cultured neurons by PrPSc-specific immunostaining. *J Gen Virol* 2016;97(8):2030-2042.
85. **Godsave SF, Wille H, Kujala P, Latawiec D, DeArmond SJ et al.** Cryo-immunogold electron microscopy

for prions: toward identification of a conversion site. *J Neurosci* 2008;28(47):12489-12499.

86. **Godsave SF, Wille H, Pierson J, Prusiner SB, Peters PJ**. Plasma membrane invaginations containing clusters of full-length PrPSc are an early form of prion-associated neuropathology in vivo. *Neurobiol Aging* 2013;34(6):1621-1631.
87. **Taraboulos A, Serban D, Prusiner SB**. Scrapie prion proteins accumulate in the cytoplasm of persistently infected cultured cells. *J Cell Biol* 1990;110(6):2117-2132.
88. **Jiang HY, Wek SA, McGrath BC, Lu D, Hai T et al.** Activating transcription factor 3 is integral to the eukaryotic initiation factor 2 kinase stress response. *Mol Cell Biol* 2004;24(3):1365-1377.
89. **Ma Y, Hendershot LM**. Delineation of a negative feedback regulatory loop that controls protein translation during endoplasmic reticulum stress. *J Biol Chem* 2003;278(37):34864-34873.
90. **McCullough KD, Martindale JL, Klotz LO, Aw TY, Holbrook NJ**. Gadd153 sensitizes cells to endoplasmic reticulum stress by down-regulating Bcl2 and perturbing the cellular redox state. *Mol Cell Biol* 2001;21(4):1249-1259.
91. **Zinszner H, Kuroda M, Wang X, Batchvarova N, Lightfoot RT et al.** CHOP is implicated in programmed cell death in response to impaired function of the endoplasmic reticulum. *Genes Dev* 1998;12(7):982-995.
92. **Kim CL, Umetani A, Matsui T, Ishiguro N, Shinagawa M et al.** Antigenic characterization of an abnormal isoform of prion protein using a new diverse panel of monoclonal antibodies. *Virology* 2004;320(1):40-51.
93. **Masujin K, Kaku-Ushiki Y, Miwa R, Okada H, Shimizu Y et al.** The N-terminal sequence of prion protein consists an epitope specific to the abnormal isoform of prion protein (PrP(Sc)). *PLoS One* 2013;8(2):e58013.
94. **Nakamitsu S, Kurokawa A, Yamasaki T, Uryu M, Hasebe R et al.** Cell density-dependent increase in the level of protease-resistant prion protein in prion-infected Neuro2a mouse neuroblastoma cells. *J Gen Virol* 2010;91(Pt 2):563-569.
95. **Yamasaki T, Suzuki A, Hasebe R, Horiuchi M**. Comparison of the anti-prion mechanism of four different anti-prion compounds, anti-PrP monoclonal antibody 44B1, pentosan polysulfate, chlorpromazine, and U18666A, in prion-infected mouse neuroblastoma cells. *PLoS One* 2014;9(9):e106516.
96. **Challis RC, Ravindra Kumar S, Chan KY, Challis C, Beadle K et al.** Systemic AAV vectors for widespread and targeted gene delivery in rodents. *Nat Protoc* 2019;14(2):379-414.
97. **Chan KY, Jang MJ, Yoo BB, Greenbaum A, Ravi N et al.** Engineered AAVs for efficient noninvasive gene delivery to the central and peripheral nervous systems. *Nat Neurosci* 2017;20(8):1172-1179.
98. **Horiuchi M, Mochizuki M, Ishiguro N, Nagasawa H, Shinagawa M**. Epitope mapping of a monoclonal antibody specific to feline panleukopenia virus and mink enteritis virus. *J Vet Med Sci* 1997;59(2):133-136.
99. **Shindoh R, Kim CL, Song CH, Hasebe R, Horiuchi M**. The region approximately between amino acids 81 and 137 of proteinase K-resistant PrPSc is critical for the infectivity of the Chandler prion strain. *J Virol* 2009;83(8):3852-3860.
100. **Fang C, Imberdis T, Garza MC, Wille H, Harris DA**. A Neuronal Culture System to Detect Prion Synaptotoxicity. *PLoS Pathog* 2016;12(5):e1005623.
101. **Ma Y, Brewer JW, Diehl JA, Hendershot LM**. Two distinct stress signaling pathways converge upon the CHOP promoter during the mammalian unfolded protein response. *J Mol Biol* 2002;318(5):1351-1365.

102. **Harding HP, Novoa I, Zhang Y, Zeng H, Wek R et al.** Regulated translation initiation controls stress-induced gene expression in mammalian cells. *Mol Cell* 2000;6(5):1099-1108.
103. **Luo S, Baumeister P, Yang S, Abcouwer SF, Lee AS**. Induction of Grp78/BiP by translational block: activation of the Grp78 promoter by ATF4 through and upstream ATF/CRE site independent of the endoplasmic reticulum stress elements. *J Biol Chem* 2003;278(39):37375-37385.
104. **Yoshida H, Haze K, Yanagi H, Yura T, Mori K**. Identification of the cis-acting endoplasmic reticulum stress response element responsible for transcriptional induction of mammalian glucose-regulated proteins. Involvement of basic leucine zipper transcription factors. *J Biol Chem* 1998;273(50):33741-33749.
105. **Mallucci GR**. Prion neurodegeneration: starts and stops at the synapse. *Prion* 2009;3(4):195-201.
106. **Siskova Z, Page A, O'Connor V, Perry VH**. Degenerating synaptic boutons in prion disease: microglia activation without synaptic stripping. *Am J Pathol* 2009;175(4):1610-1621.
107. **Campeau JL, Wu G, Bell JR, Rasmussen J, Sim VL**. Early increase and late decrease of purkinje cell dendritic spine density in prion-infected organotypic mouse cerebellar cultures. *PLoS One* 2013;8(12):e81776.
108. **Smith HL, Freeman OJ, Butcher AJ, Holmqvist S, Humoud I et al.** Astrocyte Unfolded Protein Response Induces a Specific Reactivity State that Causes Non-Cell-Autonomous Neuronal Degeneration. *Neuron* 2020;105(5):855-866.e855.
109. **Maragakis NJ, Rothstein JD**. Mechanisms of Disease: astrocytes in neurodegenerative disease. *Nat Clin Pract Neurol* 2006;2(12):679-689.
110. **Block ML, Zecca L, Hong JS**. Microglia-mediated neurotoxicity: uncovering the molecular mechanisms. *Nat Rev Neurosci* 2007;8(1):57-69.
111. **Lobsiger CS, Cleveland DW**. Glial cells as intrinsic components of non-cell-autonomous neurodegenerative disease. *Nat Neurosci* 2007;10(11):1355-1360.
112. **Schultz J, Schwarz A, Neidhold S, Burwinkel M, Riemer C et al.** Role of interleukin-1 in prion disease-associated astrocyte activation. *Am J Pathol* 2004;165(2):671-678.
113. **Hartmann K, Sepulveda-Falla D, Rose IVL, Madore C, Muth C et al.** Complement 3(+)-astrocytes are highly abundant in prion diseases, but their abolishment led to an accelerated disease course and early dysregulation of microglia. *Acta Neuropathol Commun* 2019;7(1):83.
114. **Riemer C, Schultz J, Burwinkel M, Schwarz A, Mok SW et al.** Accelerated prion replication in, but prolonged survival times of, prion-infected CXCR3-/- mice. *J Virol* 2008;82(24):12464-12471.
115. **Kerschensteiner M, Meinl E, Hohlfeld R**. Neuro-immune crosstalk in CNS diseases. *Neuroscience* 2009;158(3):1122-1132.
116. **Garden GA, La Spada AR**. Intercellular (mis)communication in neurodegenerative disease. *Neuron* 2012;73(5):886-901.
117. **Chitu V, Gokhan S, Nandi S, Mehler MF, Stanley ER**. Emerging Roles for CSF-1 Receptor and its Ligands in the Nervous System. *Trends Neurosci* 2016;39(6):378-393.
118. **Wolf Y, Yona S, Kim KW, Jung S**. Microglia, seen from the CX3CR1 angle. *Front Cell Neurosci* 2013;7:26.
119. **Liddelow SA, Guttenplan KA, Clarke LE, Bennett FC, Bohlen CJ et al.** Neurotoxic reactive astrocytes

are induced by activated microglia. *Nature* 2017;541(7638):481-487.

120. **Trettel F, Di Castro MA, Limatola C**. Chemokines: Key Molecules that Orchestrate Communication among Neurons, Microglia and Astrocytes to Preserve Brain Function. *Neuroscience* 2019.
121. **Hilton KJ, Cunningham C, Reynolds RA, Perry VH**. Early Hippocampal Synaptic Loss Precedes Neuronal Loss and Associates with Early Behavioural Deficits in Three Distinct Strains of Prion Disease. *PLoS One* 2013;8(6):e68062.
122. **Hoozemans JJ, van Haastert ES, Nijholt DA, Rozemuller AJ, Eikelenboom P et al.** The unfolded protein response is activated in pretangle neurons in Alzheimer's disease hippocampus. *Am J Pathol* 2009;174(4):1241-1251.
123. **Hoozemans JJ, van Haastert ES, Eikelenboom P, de Vos RA, Rozemuller JM et al.** Activation of the unfolded protein response in Parkinson's disease. *Biochem Biophys Res Commun* 2007;354(3):707-711.
124. **Basu U, Guan LL, Moore SS**. Functional genomics approach for identification of molecular processes underlying neurodegenerative disorders in prion diseases. *Curr Genomics* 2012;13(5):369-378.
125. **Filali H, Martin-Burriel I, Harders F, Varona L, Lyahyai J et al.** Gene expression profiling and association with prion-related lesions in the medulla oblongata of symptomatic natural scrapie animals. *PLoS One* 2011;6(5):e19909.
126. **Bartoletti-Stella A, Corrado P, Mometto N, Baiardi S, Durrenberger PF et al.** Analysis of RNA Expression Profiles Identifies Dysregulated Vesicle Trafficking Pathways in Creutzfeldt-Jakob Disease. *Mol Neurobiol* 2019;56(7):5009-5024.
127. **Dandoy-Dron F, Guillo F, Benboudjema L, Deslys JP, Lasmezas C et al.** Gene expression in scrapie. Cloning of a new scrapie-responsive gene and the identification of increased levels of seven other mRNA transcripts. *J Biol Chem* 1998;273(13):7691-7697.
128. **Duguid JR, Dinauer MC**. Library subtraction of in vitro cDNA libraries to identify differentially expressed genes in scrapie infection. *Nucleic Acids Res* 1990;18(9):2789-2792.
129. **Miele G, Manson J, Clinton M**. A novel erythroid-specific marker of transmissible spongiform encephalopathies. *Nat Med* 2001;7(3):361-364.
130. **Baker CA, Manuelidis L**. Unique inflammatory RNA profiles of microglia in Creutzfeldt-Jakob disease. *Proc Natl Acad Sci U S A* 2003;100(2):675-679.
131. **Majer A, Medina SJ, Sorensen D, Martin MJ, Frost KL et al.** The cell type resolved mouse transcriptome in neuron-enriched brain tissues from the hippocampus and cerebellum during prion disease. *Sci Rep* 2019;9(1):1099.
132. **Booth S, Bowman C, Baumgartner R, Sorensen G, Robertson C et al.** Identification of central nervous system genes involved in the host response to the scrapie agent during preclinical and clinical infection. *J Gen Virol* 2004;85(Pt 11):3459-3471.
133. **Ginsberg SD, Alldred MJ, Che S**. Gene expression levels assessed by CA1 pyramidal neuron and regional hippocampal dissections in Alzheimer's disease. *Neurobiol Dis* 2012;45(1):99-107.
134. **Carroll JA, Striebel JF, Race B, Phillips K, Chesebro B**. Prion infection of mouse brain reveals multiple new upregulated genes involved in neuroinflammation or signal transduction. *J Virol* 2015;89(4):2388-2404.

135. **Vincenti JE, Murphy L, Grabert K, McColl BW, Cancellotti E et al.** Defining the Microglia Response during the Time Course of Chronic Neurodegeneration. *J Virol* 2015;90(6):3003-3017.
136. **Sharma K, Schmitt S, Bergner CG, Tyanova S, Kannaiyan N et al.** Cell type- and brain region-resolved mouse brain proteome. *Nat Neurosci* 2015;18(12):1819-1831.
137. **Zhang Y, Chen K, Sloan SA, Bennett ML, Scholze AR et al.** An RNA-sequencing transcriptome and splicing database of glia, neurons, and vascular cells of the cerebral cortex. *J Neurosci* 2014;34(36):11929-11947.
138. **Doyle JP, Dougherty JD, Heiman M, Schmidt EF, Stevens TR et al.** Application of a translational profiling approach for the comparative analysis of CNS cell types. *Cell* 2008;135(4):749-762.
139. **Darmanis S, Sloan SA, Zhang Y, Enge M, Caneda C et al.** A survey of human brain transcriptome diversity at the single cell level. *Proc Natl Acad Sci U S A* 2015;112(23):7285-7290.
140. **Schroeder A, Mueller O, Stocker S, Salowsky R, Leiber M et al.** The RIN: an RNA integrity number for assigning integrity values to RNA measurements. *BMC Mol Biol* 2006;7:3.
141. **Anders S, Huber W**. Differential expression analysis for sequence count data. *Genome Biol* 2010;11(10):R106.
142. **Ashburner M, Ball CA, Blake JA, Botstein D, Butler H et al.** Gene ontology: tool for the unification of biology. The Gene Ontology Consortium. *Nat Genet* 2000;25(1):25-29.
143. **Zhou Y, Zhou B, Pache L, Chang M, Khodabakhshi AH et al.** Metascape provides a biologist-oriented resource for the analysis of systems-level datasets. *Nat Commun* 2019;10(1):1523.
144. **Binns D, Dimmer E, Huntley R, Barrell D, O'Donovan C et al.** QuickGO: a web-based tool for Gene Ontology searching. *Bioinformatics* 2009;25(22):3045-3046.
145. **Tortosa R, Castells X, Vidal E, Costa C, Ruiz de Villa Mdel C et al.** Central nervous system gene expression changes in a transgenic mouse model for bovine spongiform encephalopathy. *Vet Res* 2011;42(1):109.
146. **Kim HO, Snyder GP, Blazey TM, Race RE, Chesebro B et al.** Prion disease induced alterations in gene expression in spleen and brain prior to clinical symptoms. *Adv Appl Bioinform Chem* 2008;1:29-50.
147. **Hwang D, Lee IY, Yoo H, Gehlenborg N, Cho JH et al.** A systems approach to prion disease. *Mol Syst Biol* 2009;5:252.
148. **Sesele K, Thanopoulou K, Paouri E, Tsefou E, Klinakis A et al.** Conditional inactivation of nicastrin restricts amyloid deposition in an Alzheimer's disease mouse model. *Aging Cell* 2013;12(6):1032-1040.
149. **Sontag E, Hladik C, Montgomery L, Luangpirom A, Mudrak I et al.** Downregulation of protein phosphatase 2A carboxyl methylation and methyltransferase may contribute to Alzheimer disease pathogenesis. *J Neuropathol Exp Neurol* 2004;63(10):1080-1091.
150. **Ogris E, Du X, Nelson KC, Mak EK, Yu XX et al.** A protein phosphatase methylesterase (PME-1) is one of several novel proteins stably associating with two inactive mutants of protein phosphatase 2A. *J Biol Chem* 1999;274(20):14382-14391.
151. **Zhou Q, Rammohan K, Lin S, Robinson N, Li O et al.** CD24 is a genetic modifier for risk and progression of multiple sclerosis. *Proc Natl Acad Sci U S A* 2003;100(25):15041-15046.

152. **Şentürk M, Lin G, Zuo Z, Mao D, Watson E et al.** Ubiquilins regulate autophagic flux through mTOR signalling and lysosomal acidification. *Nat Cell Biol* 2019;21(3):384-396.
153. **Lamar KJ, Carvill GL**. Chromatin Remodeling Proteins in Epilepsy: Lessons From CHD2-Associated Epilepsy. *Front Mol Neurosci* 2018;11:208.
154. **Devasenapathy S, Midha R, Naskar T, Mehta A, Prajapati B et al.** A pilot Indian family-based association study between dyslexia and Reelin pathway genes, DCDC2 and ROBO1, identifies modest association with a triallelic unit TAT in the gene RELN. *Asian J Psychiatr* 2018;37:121-129.
155. **Pacault M, Nizon M, Pichon O, Vincent M, Le Caignec C et al.** A de novo 2q37.2 deletion encompassing AGAP1 and SH3BP4 in a patient with autism and intellectual disability. *Eur J Med Genet* 2019;62(12):103586.
156. **Rahbar MH, Samms-Vaughan M, Ma J, Bressler J, Dickerson AS et al.** Synergic effect of GSTP1 and blood manganese concentrations in Autism Spectrum Disorder. *Res Autism Spectr Disord* 2015;18:73-82.
157. **Tejada MI, Villate O, Ibarluzea N, de la Hoz AB, Martínez-Bouzas C et al.** Molecular and Clinical Characterization of a Novel Nonsense Variant in Exon 1 of the UPF3B Gene Found in a Large Spanish Basque Family (MRX82). *Front Genet* 2019;10:1074.
158. **Toro C, Hori RT, Malicdan MCV, Tifft CJ, Goldstein A et al.** A recurrent de novo missense mutation in UBTF causes developmental neuroregression. *Hum Mol Genet* 2018;27(4):691-705.
159. **Kopan R, Goate A**. Aph-2/Nicastrin: an essential component of gamma-secretase and regulator of Notch signaling and Presenilin localization. *Neuron* 2002;33(3):321-324.
160. **Yu G, Nishimura M, Arawaka S, Levitan D, Zhang L et al.** Nicastrin modulates presenilin-mediated notch/glp-1 signal transduction and betaAPP processing. *Nature* 2000;407(6800):48-54.
161. **Ma Z, Han D, Zuo X, Wang F, Jia J**. Association between promoter polymorphisms of the nicastrin gene and sporadic Alzheimer's disease in North Chinese Han population. *Neurosci Lett* 2009;458(3):136-139.
162. **Confaloni A, Terreni L, Piscopo P, Crestini A, Campeggi LM et al.** Nicastrin gene in familial and sporadic Alzheimer's disease. *Neurosci Lett* 2003;353(1):61-65.
163. **Dermaut B, Theuns J, Sleegers K, Hasegawa H, Van den Broeck M et al.** The gene encoding nicastrin, a major gamma-secretase component, modifies risk for familial early-onset Alzheimer disease in a Dutch population-based sample. *Am J Hum Genet* 2002;70(6):1568-1574.
164. **Nicolas G, Acuña-Hidalgo R, Keogh MJ, Quenez O, Steehouwer M et al.** Somatic variants in autosomal dominant genes are a rare cause of sporadic Alzheimer's disease. *Alzheimers Dement* 2018;14(12):1632-1639.
165. **Chen CY, Weng YH, Chien KY, Lin KJ, Yeh TH et al.** (G2019S) LRRK2 activates MKK4-JNK pathway and causes degeneration of SN dopaminergic neurons in a transgenic mouse model of PD. *Cell Death Differ* 2012;19(10):1623-1633.
166. **Hu K, Huang Q, Liu C, Li Y, Liu Y et al.** c-Jun/Bim Upregulation in Dopaminergic Neurons Promotes Neurodegeneration in the MPTP Mouse Model of Parkinson's Disease. *Neuroscience* 2019;399:117-124.
167. **Hetz C, Thielen P, Fisher J, Pasinelli P, Brown RH et al.** The proapoptotic BCL-2 family member BIM mediates motoneuron loss in a model of amyotrophic lateral sclerosis. *Cell Death Differ series vol. 7)*.

England 2007. pp. 1386-1389.

168. **Engidawork E, Gulesserian T, Seidl R, Cairns N, Lubec G**. Expression of apoptosis related proteins in brains of patients with Alzheimer's disease. *Neurosci Lett* 2001;303(2):79-82.
169. **Biswas SC, Shi Y, Vonsattel JP, Leung CL, Troy CM et al.** Bim is elevated in Alzheimer's disease neurons and is required for beta-amyloid-induced neuronal apoptosis. *J Neurosci* 2007;27(4):893-900.
170. **Pan Y, Sun L, Wang J, Fu W, Fu Y et al.** STI571 protects neuronal cells from neurotoxic prion protein fragment-induced apoptosis. *Neuropharmacology* 2015;93:191-198.
171. **Jassal B, Matthews L, Viteri G, Gong C, Lorente P et al.** The reactome pathway knowledgebase. *Nucleic Acids Res* 2020;48(D1):D498-d503.
172. **Garcia-Mata R, Boulter E, Burridge K**. The 'invisible hand': regulation of RHO GTPases by RHOGDIs. *Nat Rev Mol Cell Biol* 2011;12(8):493-504.
173. **Tcherkezian J, Lamarche-Vane N**. Current knowledge of the large RhoGAP family of proteins. *Biol Cell* 2007;99(2):67-86.
174. **Lindmo K, Stenmark H**. Regulation of membrane traffic by phosphoinositide 3-kinases. *J Cell Sci* 2006;119(Pt 4):605-614.
175. **Watson JR, Owen D, Mott HR**. Cdc42 in actin dynamics: An ordered pathway governed by complex equilibria and directional effector handover. *Small GTPases* 2017;8(4):237-244.

和文抄録

神経細胞内での正常型プリオンタンパク質（PrP^{C}）から異常型プリオンタンパク質（PrP^{Sc}）への構造転換は、プリオン病において鍵となる病態生理学的事象のひとつである。神経細胞でのプリオン増殖は、それ自体がプリオン病の神経病理における重要なイベントであると考えられているが、プリオンの増殖に対する真の神経細胞応答については十分に理解されていない。その一因として、プリオン感染と PrP^{Sc} の新規産生に対する神経細胞自律的な応答の解析に適した実験系が確立されていないことが挙げられる。私は、4 週以上にわたってアストロサイトの増殖が抑制されるよう改良した神経細胞エンリッチメント法を用いて、マウス胎仔大脳皮質および視床の初代培養神経細胞を作出してきた。この初代培養神経細胞はプリオンの感染に感受性であり、産生される PrP^{Sc} はマウス生体で産生される PrP^{Sc} と形態的・生化学的に類似した特徴を示した。そこで本研究ではこの初代培養系を用いて、プリオン感染に対する神経細胞自律的応答を解析した。

第一章では、大脳皮質および視床由来初代培養神経細胞にプリオンを感染させた時の神経細胞の変化を解析した。初代培養神経細胞で産生される PrP^{Sc} は経時的に増加したものの、これに伴う明らかな神経細胞数の減少や神経突起密度の低下は認められなかった。小胞体ストレス応答である Unfolded protein response (UPR) の PERK-eIF2α シグナリング経路の活性化状態について、個々の神経細胞を免疫染色により詳細に解析したところ、大脳皮質由来神経細胞では PrP^{Sc} とリン酸化 PERK の染色シグナル数が正の相関を示し、PrP^{Sc} 産生による PERK リン酸化の促進が示唆された。しかし、PERK リン酸化に続く下流シグナルの活性化およびシナプスタンパク質翻訳抑制は認められなかった。これらの結果は、神経細胞における PrP^{Sc} の産生は直接に小胞体ストレスを惹起し、PERK-eIF2α シグナリングの初期段階を神経細胞自律的に活性化させるが、UPR の完全な活性化には不十分であることを示している。

第二章では、プリオン感染初代培養神経細胞のトランスクリプトームの変化から神経細胞自律的応答を解析した。プリオン感染により発現変動を示した遺伝子の Gene Ontology 解析および Ingenuity Pathway Analysis を用いたパスウェイ解析では、神経変性や神経細胞死に直接つながるシグナル経路や生物学的機能の活性化は予測されなかった。この結果は第一章の解析結果と

一致して、初代培養神経細胞でのプリオンの増殖に対する神経自律的応答は、神経細胞死に至るプロセスを完全には活性化しないことを示唆している。一方で、神経変性や神経細胞死に直接の関連は認められないものの、プリオン感染神経細胞において細胞骨格リモデリング、脂質代謝に関連するシグナル経路や生物学的機能が変化することが示唆された。トランスクリプトーム解析により、プリオン感染神経細胞において細胞・生物機能の劇的な変化は神経細胞自律的には生じないことが示されたが、このプリオン感染初代培養神経細胞の網羅的遺伝子発現変動データはプリオン病の神経変性メカニズムを理解するうえで今後も有効に活用されるものと考えている。

この学位論文では、プリオン病における神経細胞自律的な神経変性メカニズムの解明に向けて種々の解析に取り組み、プリオンの増殖自体が神経病理学的な初期変化である小胞体ストレスの原因となるが、この初期異常は神経自律的には UPR 全体の活性化に至らないことを明らかにした。トランスクリプトーム解析においても、プリオンの増殖によって明らかに影響を受ける神経細胞特異的なシグナル経路や生物学的機能が特定されなかった。これらの結果は、プリオン病の神経変性メカニズムにおいては、神経細胞での PrP^{Sc} の産生に加えて、非神経細胞因子が重要な役割を果たすことを示唆している。本研究は神経変性メカニズムの完全な理解に向けて、基盤となるプリオン感染神経細胞の変化を明らかにした点で、今後の研究の発展に大きく寄与するものである。